

POLITECNICO DI TORINO

Corso di Laurea Magistrale
in Ingegneria Aerospaziale



Tesi di Laurea Magistrale

Wavelet analysis of complex flow fields

Candidato:

Salvatore LAURETTA

Relatori:

Prof. Gaetano IUSO

Prof. Giocchino CAFIERO

2019/2020

Abstract

Since the beginning of turbulence studies, one of the most challenging problems was to correctly educe coherent structures within the chaotic motion of turbulent flows. From flow visualization through velocity gradient-based methods all have positive aspects and drawbacks.

The present work takes inspiration and bases its development on previous studies concerning *wavelet transform analysis* of turbulent flow velocity signals for coherent structures' eduction. The wavelet transforms come from signal analysis theory and are a mathematical means to perform signal analysis when signal frequency varies over time employing a small wavelet with a limited duration. Thus, frequencies which compose the signal and its energy content and, moreover, their location along the signal duration can be retrieved. This is the significative characteristics which distinguishes wavelet transforms and Fourier transforms. Indeed, the latter loses information about the energy content's location within the signal.

Particularly, we focused on the analysis of flow fields retrieved through *Particle Image Velocimetry (PIV)* technique and showing energy maps which highlight the presence of possible coherent structures within the flow field.

Firstly, a synthetic vortex and a round jet, relatively simple flow fields, are evaluated to allow the wavelet-based code validation. Once it's been ascertained for the code to work properly, despite some inaccuracies, a more sophisticated flow field is examined. The analysis is performed on turbulent boundary layer over smooth and *riblet* surfaces. Riblet surfaces (or simply riblets) are adopted for flow control showing good drag reduction performances. The obtained results are then treated statistically to highlight possible differences between smooth plate and riblets' boundary layer.

Sommario

Sin dagli albori dello studio di flussi turbolenti, una delle principali sfide risiede nell'identificazione di strutture coerenti. Nel corso degli anni, diversi metodi basati sulla visualizzazione dei campi di moto tramite traccianti o metodologie analitiche basate sulla valutazione di gradienti o in generale variazioni di velocità sono stati messi a punto.

Il presente elaborato prende ispirazione da studi precedenti riguardo l'impiego delle *trasformate di wavelet* per l'analisi di segnali di velocità di flussi turbolenti con l'obiettivo di identificare la presenza di strutture coerenti. Le *trasformate di wavelet* provengono dalla teoria dei segnali e permettono la valutazione di segnali all'interno dei quali si hanno variazioni frequenza. Ciò viene effettuato tramite una "ondina", appunto *wavelet*, la quale presenta una determinata frequenza e una durata limitata, ovvero è dotata di un supporto limitato nel tempo (o nello spazio). Quindi, è possibile ottenere il contenuto energetico e, soprattutto, la posizione lungo il segnale delle varie frequenze che compongono lo stesso. È questa la significativa differenza rispetto alle *trasformate di Fourier* le quali, invece, perdono l'informazione riguardo la posizione di tale contenuto energetico spalmandola su tutto il dominio.

In modo particolare, si cerca di analizzare campi di moto ottenuti mediante tecnica PIV (*Particle Image Velocimetry*) visualizzando delle mappe di energia che mettano in luce la presenza di eventuali strutture coerenti all'interno del campo di moto.

Inizialmente, vengono analizzati un vortice sintetico, ottenuto per via analitica, e il campo di moto di un getto che, in quanto campi relativamente semplici, possono permettere la validazione del codice. Una volta accertato il corretto funzionamento del codice, vengono analizzati dei campi di moto più complessi. In particolare, si valutano i campi di moto relativi allo strato limite che si genera su una placca piana liscia e su tre differenti tipi di superfici riblettate (o riblets). Le riblets vengono adoperate per il controllo di flussi e mostrano buone performance per quel che riguarda la riduzione della resistenza. Questi ultimi risultati vengono, poi, analizzati statisticamente per cercare di mettere in luce eventuali differenze tra strato limite su placca liscia e su riblets.

Contents

1	Introduction to Wavelet Transform.....	- 1 -
1.1	Definition.....	- 1 -
1.2	Time-Frequency vs. Space-Scale analysis.....	- 3 -
1.3	Wavelet transform and turbulence.....	- 5 -
2	Coherent structures identification in 2D flow fields	- 7 -
2.1	What is a coherent structure?.....	- 7 -
2.2	Eduction techniques	- 9 -
2.3	Particle Image Velocimetry	- 11 -
2.4	Wavelet analysis of particle image velocimetry data	- 12 -
3	Wavelet based code validation.....	- 15 -
3.1	Synthetic Lamb-Oseen vortex analysis	- 15 -
3.2	The round jet	- 18 -
3.2.1	Jet description	- 18 -
3.2.2	Coherent structures in a turbulent round jet.....	- 19 -
3.2.3	Experimental set-up	- 20 -
3.2.4	Wavelet analysis near the potential core	- 21 -
3.2.5	Wavelet analysis extended to the transitional region	- 31 -
4	Turbulent boundary layer over smooth and riblet surfaces.....	- 44 -
4.1	Boundary layer description	- 44 -
4.2	Coherent motion in turbulent boundary layer	- 47 -
4.3	Drag Reduction technologies.....	- 52 -
4.4	Drag reduction by riblet surfaces	- 54 -
4.5	Technological applications of riblets	- 62 -
5	Wavelet analysis of turbulent boundary layer	- 64 -
5.1	Experimental set-up and PIV measurements.....	- 64 -
5.2	Smooth plate	- 67 -
5.3	Riblet surfaces.....	- 71 -

5.4	Statistical analysis.....	- 76 -
6	Conclusion.....	- 94 -
6.1	Future works.....	- 95 -
	Bibliography	- 97 -
	Ringraziamenti.....	- 101 -

1 Introduction to Wavelet Transform

1.1 Definition

Wavelet transform is a mathematical technique that allows to analyze signals or images which present abrupt changes. In fact, wavelet transform allows to unfold a signal into both time and frequency. The basic concept is to superimpose a *mother wavelet* on the test signal and to make two simple operations: *scale* and *translate*.

The *mother wavelet* is a mathematical function characterized by a limited spatial support and a given frequency called center frequency of the mother wavelet. Typical shape of a wavelet is reported in

Figure 1.1. As it can be seen, one can choose a real-valued or a complex-valued wavelet function. The choice of one or another type depends on the analysis to perform. For example, a *complex* wavelet function will return information about both amplitude and phase and is better adapted for capturing oscillatory behavior. A *real* wavelet function returns only a single component and can be used to isolate peaks or discontinuities. The *shape* of wavelet function should reflect the features present in the analyzed signal.

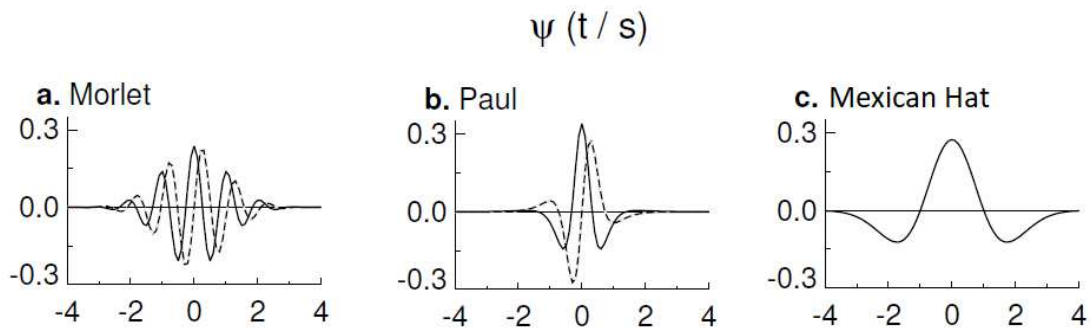


Figure 1.1 - Three types of Wavelet functions. Solid lines represent real part of wavelet function, while the dashed lines represent the imaginary part. (a) Morlet complex-valued wavelet, (b) Paul complex-valued, (c) Mexican Hat real-valued wavelet.

Thanks to these characteristics of the wavelet, the analysis can be performed locally on the signal, as opposed to the Fourier Transform which is nonlocal, indeed it does not lose information about the signal, but instead spread it away. As can be seen from Figure 1.2, the Fourier Transform detects the energy associated with

frequencies which constitute the signal, but it can't give any information about where this energy is placed along the signal.

The two operations previously mentioned are performed over the mother wavelet. The wavelet is, initially, *scaled* by a factor a and *translated* along the whole signal performing the *convolution* operation between the scaled wavelet and the signal. The scaling factor a stretch or compress the wavelet properly, so singularities inside the signal are detected. If a is increased the wavelet will appear stretched, whereas if it is decreased the wavelet will appear compressed fitting better the rapid changes in the signal.

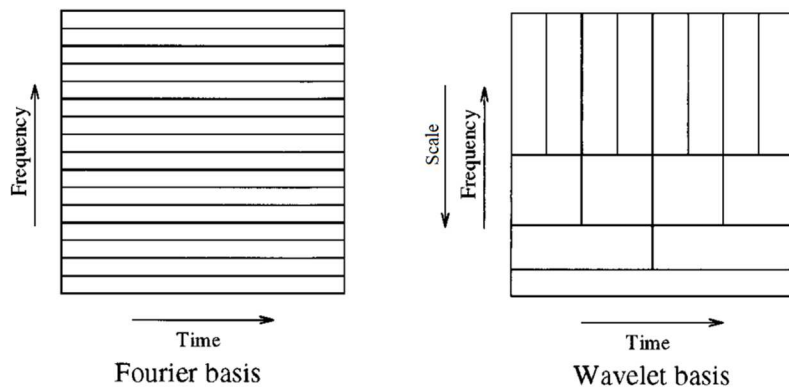


Figure 1.2 - Decomposition of signals based on the Fourier Transform and the Wavelet Transform.

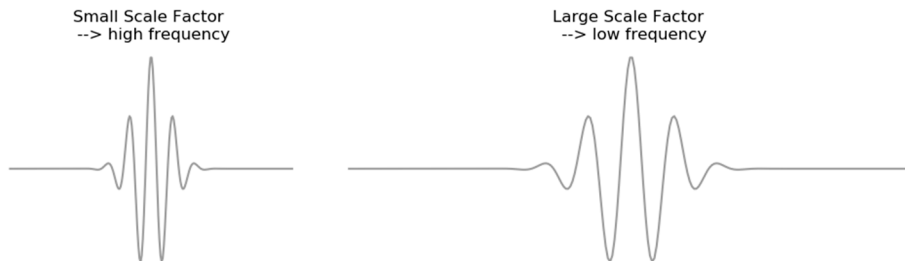


Figure 1.3 - Effect of scale factor a on wavelet spatial support.

For each scale factor considered, a shifting operation is performed so, at the end of the analysis, a *frequency (or scale) decomposition* of the signal is obtained. That process gives very good resolution in the small scales and in large scales too. Nevertheless, according to the *Heisenberg's uncertainty principle*, the variation of the number of oscillations, or cycles, of the mother wavelet leads to a different resolution in time and frequency. Indeed, if a mother wavelet with many cycles is selected, we obtain a great resolution in frequency, while the time resolution, i.e. the time position of the detected variation in the signal is not well resolved. By contrast,

with less oscillation the wavelet gives a low resolution in frequency but a great resolution in time.

Two main types of wavelet transform exist; the *continuous wavelet transform*, and the *discrete wavelet transform*.

The 1D *Continuous wavelet transform* of the $f(x)$ function scaled by the factor a is obtained as follows:

$$w^a(x) = a^{-1/2} \int f(x') \psi^* \left(\frac{x - x'}{a} \right) dx' \quad (1.1)$$

whit a as the *scale dilation parameter* corresponding to the width of the wavelet, x' as the translation parameter corresponding to the position of the wavelet and ψ^* as the complex conjugate of ψ , the so-called mother wavelet function; a and x' are dimensionless variables. The wavelet coefficients will correspond to energy densities. If a function is locally smooth the corresponding wavelet coefficients will remain small, while if a singularity is present, in its vicinity the wavelet coefficients' amplitude will increase [1]. For analysing purposes, the continuous wavelet transform is preferable because its redundancy allows good legibility and an unfolding of the signal's information content on the *time-frequency* domain.

The *Discrete wavelet transform* (or *orthogonal wavelet transform* due to orthogonal wavelet property) is better suited for compression or modelling purposes because it decomposes the signal into a minimal number of independent coefficients on a dyadic grid.

For present work's objective, the continuous wavelet transform is adopted.

1.2 Time-Frequency vs. Space-Scale analysis

As mentioned above, the scale factor a is used to reduce or increase the mother wavelet's width. Since the wavelet analysis was largely adopted in time signal analysis, the time-frequency study of the signal is performed. For the sake of simplicity, we consider a signal as reported in Figure 1.4, composed by two well distinguished frequencies; the wavelet analysis is performed and the so called *scalogram* is obtained with time in the x-axis and frequencies in the y-axis, while the contour represents the energy density of the signal, obtained as the square value of wavelet coefficients.

$$E_w(a, x') = |w(a, x')|^2 \quad (1.2)$$

A local energy density, which measures the cross-energy density of two processes (that identifies their local correlation) is defined as:

$$E_{wxy}(a, x') = w_x(a, x')w_y(a, x') \quad (1.3)$$

which can be represented as wavelet *coscalogram*.

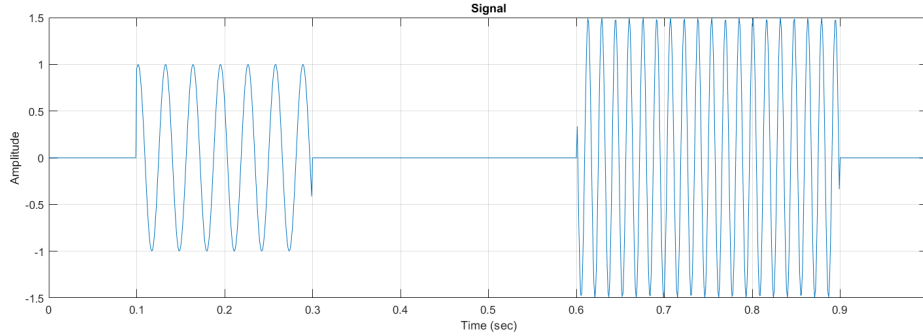


Figure 1.4 - The signal is composed by two frequencies: 32Hz in 0.1-0.3 time interval with an amplitude of 1 and 64Hz in 0.6-0.9 time interval with a 1.5 amplitude.

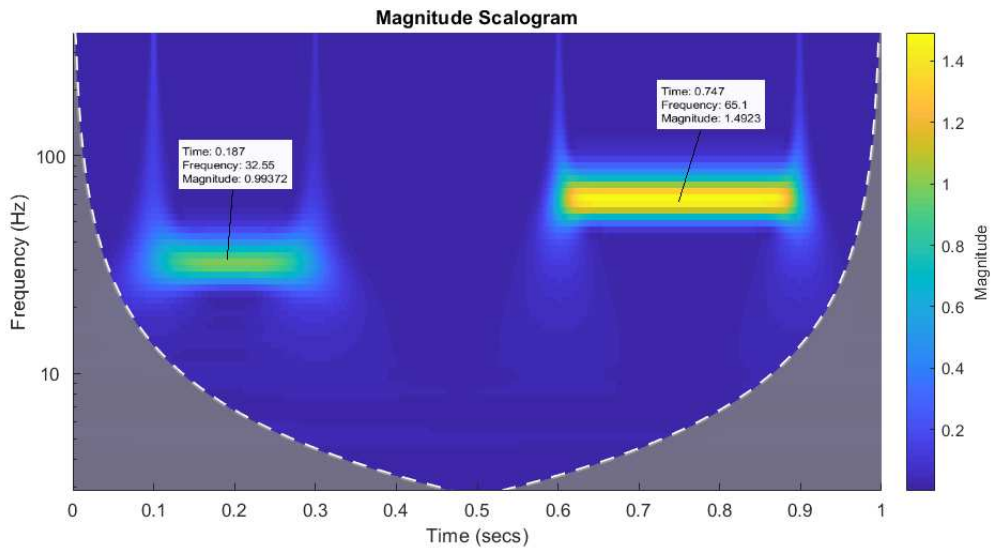


Figure 1.5 - The scalogram puts in evidence the signal's frequencies and, as can be noted, the magnitude corresponds with the signal amplitudes.

The same thing can be expressed in terms of period instead of frequency obtaining the same result, but in the form of time-period.

The concepts stated above, can be perfectly translated in the space domain considering a signal sampled in space rather than in time. Thus, the scalogram obtained will have the space in x-axis and something like “space frequency” in y-axis. The product of this “space frequency” with the constant 2π is the *wavenumber* k defined as $k = 2\pi/r$ where r is the spatial size. In this case, we obtain a *space-*

wavenumber, or better a *space-scale analysis*. To better understand, the analysis process will be well explained.

The effect of the scale factor a is to shrink or widen the mother wavelet. The wavelet is associated with a purely periodic signal with frequency F_c , called *center frequency* of the wavelet with scale factor $a = 1$ (so, the wavelet is not shrunk nor widened). When a scale factor is applied, the center frequency is increased or decreased, as the equation (1.4) states, leading to the so called *pseudo-frequency* F_{eq} .

$$F_{eq} = \frac{F_c}{a} \tag{ 1.4 }$$

In other words, F_{eq} represents the frequency of the periodic signal associated with the scaled wavelet (see Figure 1.6).

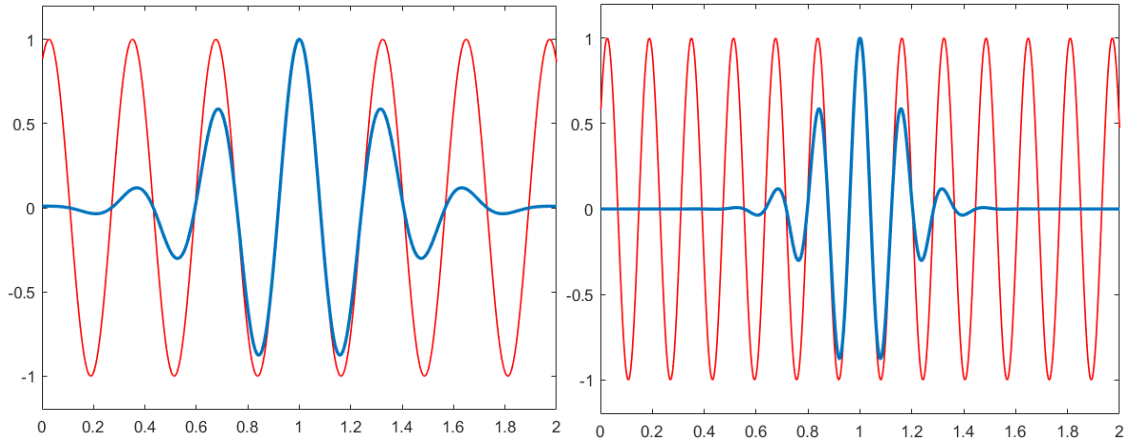


Figure 1.6 - Effect of scale factor ($a > 1$) on wavelet (blue line) width and associated period signal (red line); (a) pseudo-frequency $F_{eq} = 3.08\text{Hz}$ corresponding to a larger scale factor, (b) pseudo-frequency $F_{eq} = 6.17\text{Hz}$ corresponding to a lower scale factor.

Thus, a relationship between frequency and scale is showed, precisely, the frequency results to be inversely proportional to the scale.

Once the wavelet is scaled, it is translated along the domain and the operation of *convolution* is performed with the signal to be analysed. Then, the process is repeated with another scale factor. In so doing, the wavelet coefficients are obtained.

1.3 Wavelet transform and turbulence

In the field of turbulence, it is well known the energy cascade spectrum of a turbulent flow, in which the three regions corresponding to integral scale, inertial range and dissipative scales are observed in relation with wavenumbers. Thus, we

can retrieve from the spectrum at which frequencies (or wavenumbers) most of the energy is contained. But there is a lack in the theory. We don't know, in physical space, where the energy is contained.

In turbulent flows most of the energy is contained within rotating structures known as coherent structures. Therefore, we need to locate some elementary coherent structures. With the help of wavelet this begin possible. In fact, wavelet transform allows to unfold the signal in both space and scale, enabling the possibility to locate the structures and measure their contribution to the energy spectrum.

2 Coherent structures identification in 2D flow fields

2.1 What is a coherent structure?

Since the earliest observations, turbulence has been described as chaotic motions dominated by a random behavior. But soon, the observation of structures presenting some sort of order, took scientists to think about the possible presence of some sort of order in the chaos.

Historically, the notion of *coherence* was related to wave phenomena of acoustic, electro-dynamic physics, meaning “[...] relation of coincidence between two sets of waves, which will produce interference phenomena [...]”. In the present context, the meaning of *coherence* is intended in a wider significance, in a more colloquial sense. Thus, a coherent structure is a flow structure with discernible correlation and which, by its repetitive specific properties characterize a specific flow.

Flow fields reproduced in laboratory (Figure 2.1) with relatively small Reynolds in which this type of structures was observed, invites criticism and skepticism with respect to the fully developed turbulent structures. Indeed, one must ask whether the clearly visible “coherent” structures are possibly relics of the characteristic structures of the laminar-turbulent transition. But, observation of natural phenomena took off the answer (Figure 2.2). Essentially, meteorological structures, oil-wakes in the lee of damaged tanker ships and, as an extreme case, the structures in the Jupiter’s atmosphere are all characterized by Reynolds number of the order of 10^7 or greater, thus fully turbulent flow fields.

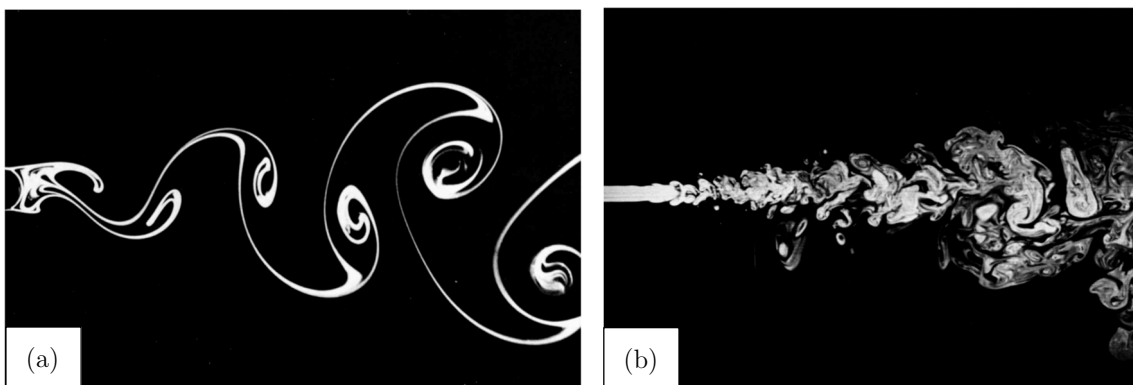


Figure 2.1 - Flow structures in laboratory visualization: (a) Karman vortex street behind a circular cylinder at $Re = 140$ (Ref [2], 94), (b) Turbulent water jet at $Re = 2300$ (Ref. [2], 166).

From flow visualization, some criteria may be derived for coherent structure with the purpose to provide a definition.

Typically, coherent structures are composed by different scales, from the largest, comparable to the lateral flow dimension, to the smallest and, sometimes, large-scale structures can be broken down in more elementary small structures with their own coherent properties. They exhibit a high degree of organization in their structures as well as in their dynamics and they show a strong similarity with the structures of the laminar-turbulent transition. Lastly, they are pattern recurrent, having such a temporal coherence, i.e. they must persist

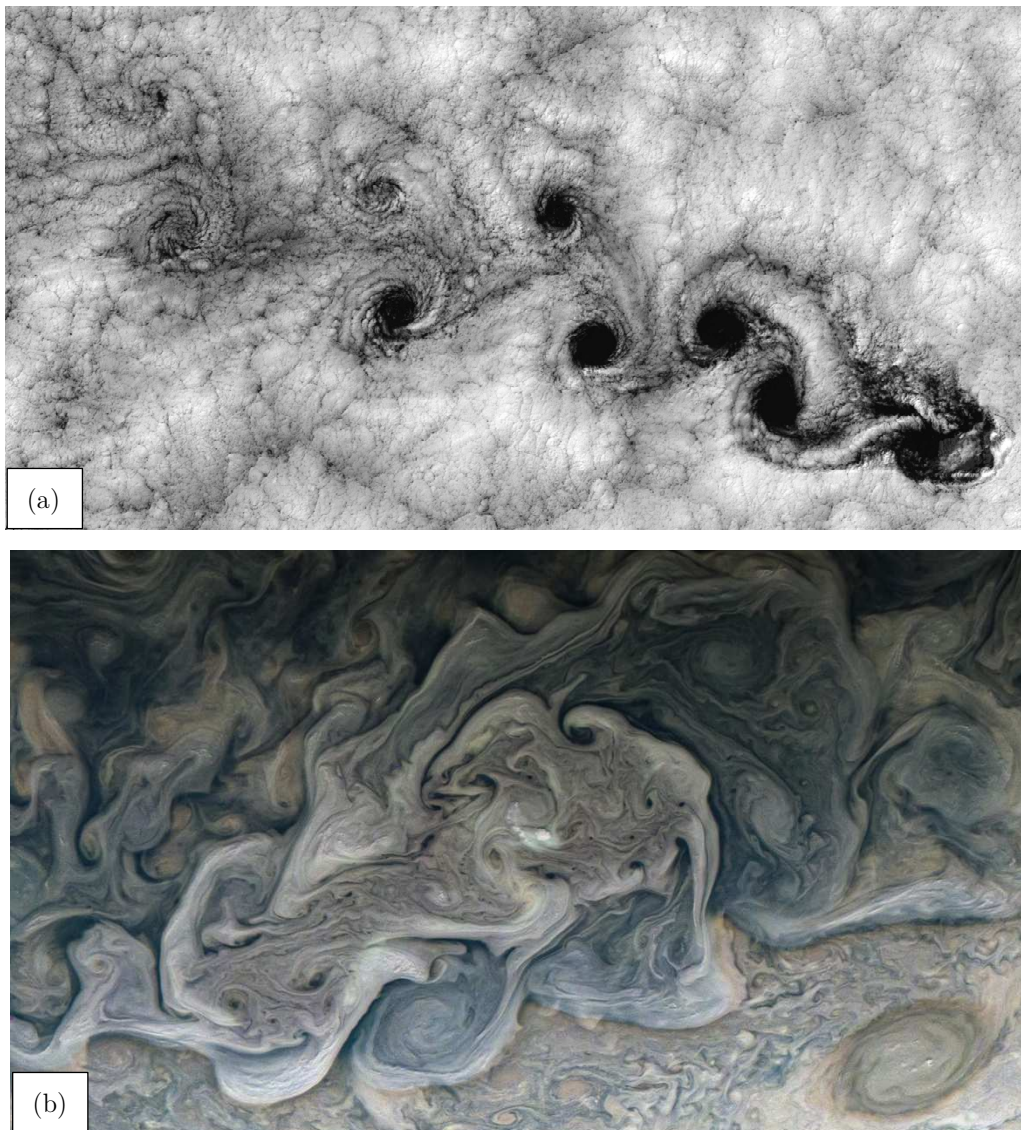


Figure 2.2 - Coherent structures observed in nature: (a) Von Karman vortex street behind the Robinson Crusoe Island [NASA Earth Observatory], (b) Turbulent structures in Jupiter's atmosphere [NASA/JPL-Caltech].

in time [3]. In the past years, efforts to provide a precise definition of what a coherent structure is was made by many researchers.

In 1983, Hussain, with his article, proposed a definition for coherent structures. He stated that “a coherent structure is a connected turbulent fluid mass with instantaneously phase-correlated vorticity over its spatial extent” [4]. That means, the random three-dimensional vorticity, that characterizes turbulence, possesses an organized component which is phase-correlated over the spatial extent of the structure.

The initial formation of coherent structures is the result of local instability of laminar or turbulent free shear layers or boundary layers and initial conditions play a fundamental role in their generation.

In wall or free flows, different types of coherent structures can be distinguished becoming a characterization feature of that precise flow fields (see Section 3.2.2 and 4.2 for more details).

2.2 Eduction techniques

In previous years, the main approach for coherent structures and eddy detection was the visualization technique by means the injection of tracing fluids or particles in the main flow. Lately, several “analytic” methodologies have been developed for the extraction of coherent structures from bidimensional velocity fields which are obtained, for example, through *particle image velocimetry* technique which provides the two components U and V of velocity vector \mathbf{V} . Some of these methods are briefly described below [5]:

Direct analysis of vorticity field ω

Regions of maximum vorticity, computed from the velocity field, can show local rotational velocity vectors according to its definition $\omega = \nabla \times \mathbf{V}$. However, this approach may not be always satisfactory since $|\omega|$ doesn't identifies vortex cores in a shear flow, especially if the background shear is comparable with the vorticity magnitude of the vortex core. Moreover, the locality of the vorticity definition enhances small scales, so it become difficult to separate noise from real small length scales structures.

Galilean decomposition

The velocity field is translated by the *convective velocity* U_a , so rotating structures become well visible by plot the velocity vector field. The drawback of the method stands in the non-deterministic value of the convective velocity, so some rotating structures are advected with slightly different velocity. For example, in the shear layer of a jet flow the convective velocity can be assumed equal to half of the jet ejection velocity obtaining good results. Nevertheless, it is way too problematic to establish a correct velocity value of convection of many structures in a fully turbulent boundary layer flow. So, the plot of velocity field for more than one convective velocity is needed to visualize all the eddies within the flow.

λ_2 and Q definition [5]:

Both methods adopt the evaluation of the *velocity gradient tensor* $\nabla\mathbf{V}$. The symmetric \mathbf{S} and antisymmetric $\mathbf{\Omega}$ components of $\nabla\mathbf{V}$ are defined, respectively, as:

$$S_{ij} = \frac{1}{2}(u_{i,j} + u_{j,i}) \quad \Omega_{ij} = \frac{1}{2}(u_{i,j} - u_{j,i}) \quad (2.1)$$

We compute the eigenvalues of $\mathbf{S}^2 + \mathbf{\Omega}^2$ and, since this tensor is symmetric, it has real eigenvalues only. If λ_1 , λ_2 and λ_3 are the eigenvalues and $\lambda_1 \geq \lambda_2 \geq \lambda_3$, the region where $\lambda_2 < 0$ is the vortex core (λ_2 -Definition).

The quantity Q of the Q -definition method is defined as:

$$Q = -\frac{1}{2}tr(\mathbf{S}^2 + \mathbf{\Omega}^2) = -\frac{1}{2}(\lambda_1 + \lambda_2 + \lambda_3) \quad (2.2)$$

Regions in which Q is positive locate vortex cores. The λ_2 and Q definition give comparable results in some flow fields, but it seems that λ_2 definition shows better results in a larger variety of flows in which Q definition provides incorrect description of vortex topology and geometry.

Proper orthonormal decomposition (POD)

The POD is an eduction technique based on the identification of the motions which contain the most part of the energy of the flow. Precisely, it exploits the two-point velocity correlation and provides a representation for the fluctuating velocity field. Considering a random scalar function $u(x)$ in the domain $0 \leq x \leq L$, an orthonormal decomposition of the function is performed

$$u(x) = \sum_{n=1}^{\infty} a_n \phi_n(x) \quad (2.3)$$

where ϕ_n is a set of real non-random basis function which satisfy the orthogonal condition and a_n are the random coefficients of the basis function. The average mean energy of $u(x)$ is defined as

$$E = \frac{1}{L} \int_0^L \frac{1}{2} \langle u(x)^2 \rangle dx \quad (2.4)$$

and by means the equation (2.3) it can be written

$$E_N = \sum_{n=1}^N \frac{1}{2} \langle a_n^2 \rangle \quad (2.5)$$

which represents the energy content of the first N modes. The basis functions are chosen in a way to maximize the energy content of the first N modes [6].

2.3 Particle Image Velocimetry

The Particle Image Velocimetry (PIV) is a non-intrusive anemometric technique which provides a quantitative measure of the instantaneous flow field. Three types of PIV technique exist based on the number of velocity vector's components retrieved and on the dimension of the flow field portion analysed.

- 2C2D \rightarrow Two in-plane components retrieved in a two dimensions sample domain, i.e. a plane, by means a single camera;
- 3C2D (*Stereoscopic PIV*) \rightarrow Three components retrieved in a plane, by means two cameras.
- 3C3D (*Tomographic PIV*) \rightarrow Three components retrieved in a 3D volume, by means two or more cameras.

Data in the present work was obtained with 2C2D PIV technique. To allow particles visualization, *tracing particles* are added to seed the flow. These particles should have similar characteristics with the flow, like density, in order to ensure that particles follow closely flow motion. To guarantee that, the non-dimensional parameter called *Stokes number* should be much smaller than unity:

$$St = \frac{t_p}{t_0} \ll 1 \quad (2.6)$$

where t_0 is a typical time of the flow, like the convection time, while t_p is the particle relaxation time:

$$t_p = \frac{d_p^2 \rho_p}{\mu} \quad (2.7)$$

with d_p the particle diameter, ρ_p particle density and μ the fluid dynamic viscosity. At this point, the area to be examined is illuminated with two consecutive laser sheet impulse. The tracing particles reflect the laser light, which is collected by a camera which is synchronised with the laser. Two images at two different time instants are obtained. By comparison of the two images, which shows the displacements of particles, the velocity components are retrieved, since the time interval Δt between two laser flashes is known. The right time interval must be chosen; if a too long time interval is selected, probability that particles leave the 2D illuminated plane during Δt increases (3D effect) and, moreover, the obtained velocity departs from the real instantaneous value and approaches a mean value. By contrast, short Δt give short displacements which are not reliable due to background noise effects. In order to analyse the images each shot is divided into smaller windows called *interrogation window*. So, each window of the first frame is compared with the second one by means a *cross-correlation* approach. This way, for each interrogation window a velocity vector is obtained (see Figure 2.3). A good processing output requires the correct particle density within each window to obtain a relatively high value of the cross-correlation coefficient. Poor and high density particle distribution both lead to a low value of cross-correlation coefficient resulting in a not reliable processed image.

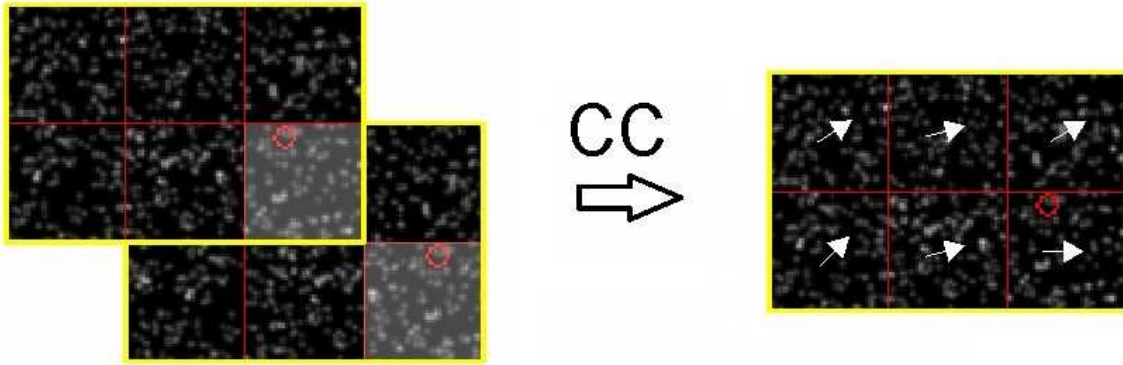


Figure 2.3 - The two consecutive frames are divided into small interrogation window, and later are processed by a cross-correlation process obtaining a velocity vector for each window.

2.4 Wavelet analysis of particle image velocimetry data

The present technique is proposed by R. Camussi and for more detail we remand to the related scientific article reported into the references [7].

The starting point of the method is the definition of wavelet transforms reported in Section 1.1. The type of mother wavelet selected for the present study is the complex-valued Morlet one, while in the scientific article is select the real-valued Mexican Hat. It is been checked that the use of others mother wavelet's types does not affect the result obtained [7].

In 2D velocity fields, the equation (1.1) can be extended to two dimensions, but for the present purpose, 1D wavelet transform will be adopted in order to obtain quantities which have clearer physical meaning related to the *vorticity*.

From PIV measurements, two bidimensional matrixes are usually retrieved corresponding each to the two components $U(x_1, x_2)$ and $V(x_1, x_2)$ of the velocity vector \mathbf{V} , where x_1 and x_2 are the Cartesian axes with U parallel to x_1 e V parallel to x_2 .

Thus, when 1D wavelet transform is applied to velocity vector's components four tensor are obtained:

$$w_{i,k}^r(x_1, x_2) \quad i, k = 1, 2; \quad r_{min} \leq r \leq r_{max}.$$

The index i correspond to the selected velocity component (1 for U and 2 for V) and the index k to the direction of transformation (i.e. along x_1 and x_2). In order to evaluate the contribution of vorticity, the two matrices $w_{1,2}^r$ and $w_{2,1}^r$ are considered. Indeed, the definition of the z-component of vorticity is given by:

$$\omega_z = \frac{\partial U}{\partial y} - \frac{\partial V}{\partial x} \quad (2.8)$$

So, the following quantity is defined:

$$E(x_1, x_2)^r = \left[\left(\frac{w_{1,2}^r w_{1,2}^{r*}}{\langle w_{1,2}^r w_{1,2}^{r*} \rangle} \right) \left(\frac{w_{2,1}^r w_{2,1}^{r*}}{\langle w_{2,1}^r w_{2,1}^{r*} \rangle} \right) \right]^{\frac{1}{2}} \quad (2.9)$$

The quantities $w_{i,k}^{r*}$ are complex conjugates and the $\langle \cdot \rangle$ notation states for spatial average over both x_1 and x_2 . So, $E(x_1, x_2)^r$ represents the 2D map of a non-dimensional normalized energy at the scale r (or a). The presence of coherent structures might be associated with region where this quantity is large. There is a direct connection between the quantity $E(x_1, x_2)^r$ and the 1D counterpart called *local intermittency measure (LIM)*, introduced by Farge [1] and successively adopted for coherence structure eduction of 1D velocity time series. So, we refer to the quantity of equation (2.9) as *local energy*. In equation (2.9), the numerator is a measure of the cross-energy density of the two transformed signals.

To better identify these regions a threshold can be defined. Thus, regions where the value of $E(x_1, x_2)^r$ overcomes its standard deviation at the scale r are considered, as the following equation states:

$$E(x_1, x_2)^r > \langle [E(x_1, x_2)^r - \langle E(x_1, x_2)^r \rangle]^2 \rangle^{\frac{1}{2}} \quad (2.10)$$

The spatial average, reported as $\langle \cdot \rangle$, is performed over the whole field, once the scale r is selected. We denote with \tilde{x}_1 and \tilde{x}_2 that regions which satisfy the equation (2.10). Once a region is selected, the mean energy content within it is calculated by:

$$\tilde{E}(r) = \langle E^r(\tilde{x}_1, \tilde{x}_2) \rangle_{\tilde{x}_1, \tilde{x}_2} \quad (2.11)$$

For each scale r , the average of the energy over the region \tilde{x}_1, \tilde{x}_2 is performed. Thus, the quantity $\tilde{E}(r)$ represents the mean energy within that region for each scale and, clearly, it will be a function of the scale r only. That quantity can be utilized to determine the typical length scale \bar{r} (or wavenumber) characterizing the coherent structure within the region selected. The typical length scale of the coherent structure corresponds to the resolution \bar{r} which maximize the energy content, in other words, the resolution \bar{r} corresponding to the maximum of the curve $\tilde{E}(r)$ is the typical length scale, as the following condition states:

$$\bar{r} = r : \tilde{E}(\bar{r}) = \max \{ \tilde{E}(r) \} \quad (2.12)$$

Once the scale \bar{r} is selected, the precise position of the coherent structure (\bar{x}_1, \bar{x}_2) can be identified locating the coordinates of the maximum value of $E^{\bar{r}}(\tilde{x}_1, \tilde{x}_2)$:

$$\bar{x}_1, \bar{x}_2 = x_1, x_2 : E^{\bar{r}}(\bar{x}_1, \bar{x}_2) = \max \{ E^{\bar{r}}(\tilde{x}_1, \tilde{x}_2) \} \quad (2.13)$$

We expect that the maximum value of energy is located in (or near) the vortex core, in the light of the connection between wavelet transform and velocity gradient.

The presented technique will be applied in the present study.

3 Wavelet based code validation

In the following sections, the examined flow fields are presented, and the related wavelet analysis and consequent results are discussed. We start with the analysis of a synthetic flow field which consists in a Lamb-Oseen vortex analytically generated. In so doing, we will have a general idea whether the code works properly. To obtain a better validation, the code will be applied to the round jet flow field which shows a relatively simple structure of the flow near the potential core, at least. In Section 5, turbulent boundary layer over smooth and riblet surfaces will be analyzed to capture possible differences between them. The round jet and boundary layer flows was obtained by means PIV measures.

3.1 Synthetic Lamb-Oseen vortex analysis

The Lamb-Oseen vortex models a vortical structure which decays in time due to the action of viscosity. The analytical model describes the tangential velocity V_θ as function of the radial coordinate R and the time t through the equation:

$$V_\theta(R, t) = \frac{\Gamma}{2\pi R} \left(1 - e^{-\frac{R^2}{4\nu t}} \right) \quad (3.1)$$

where Γ is the circulation of the vortex core and ν is the cinematic viscosity. The evolution of V_θ along R is depicted in Figure 3.1(a), where we indicate as vortex radius a the distance from the vortex center at which the tangential velocity reaches its maximum value.

The x-component U of the velocity is reported in Figure 3.1(c).

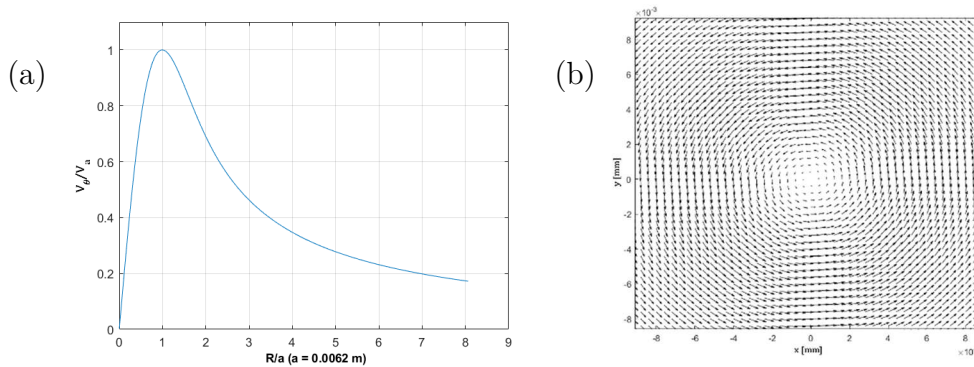


Figure 3.1(a)(b) - For caption see next page.

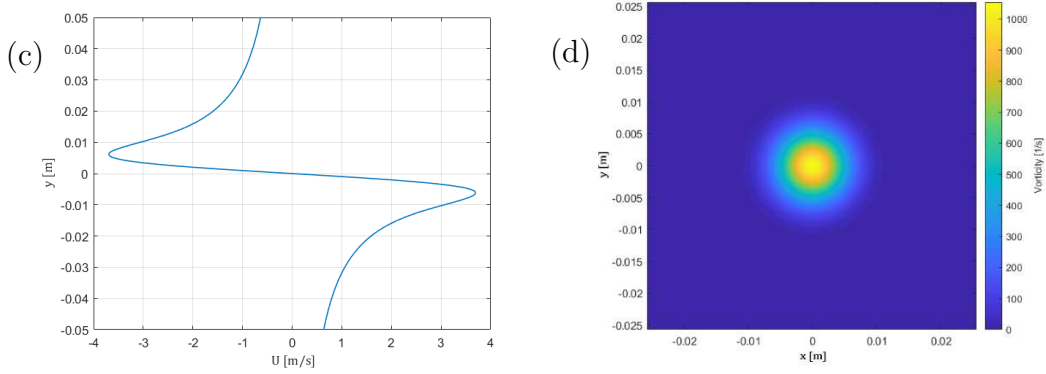


Figure 3.1 - (a) Evolution of V_θ from vortex centre; (b) Velocity vectors show the vortex structure; (c) Variation of U along the vertical direction y ; (d) Vorticity map of the vortex.

From wavelet analysis, we expect that the energy concentration will reach its maximum value for a length-scale multiple of the vortex radius and the energy distribution in the $x - y$ plane should mimics the distribution of vorticity due to the definition of $E(x_1, x_2)^r$ in the eq. (2.9). Indeed, once the analysis was performed, the obtained results clearly indicated a positive detection of the vortex. The $E(r)$ plot, where E is the result of the energy average over the selected area and r indicates the resolution (or scale) as described by eq. (2.11), presents a dominant maximum for $r/a \simeq 1.18$ which, finally, should indicates the vortex length scale (see Figure 3.2). There is not a perfect matching between the vortex's radius and the resolution r , that is $r/a = 1$, because there isn't a perfect definition of the vortex radius, and more important, because the peak in the $E(r)$ plot represents the averaged value over the selected area which take into account the low energy distribution around the vortex which became a little wider, in terms of spatial extension, for $r/d = 1.178$ (Figure 3.3(d)) and contributes more than the very well localized maximum of energy on the vortex centre showed in Figure 3.3(c) for $r/a \simeq 1.081$ which, thus, results to be the effective vortex length-scale. The wavelet maps (or energy maps) obtained are reported in Figure 3.3, and they show that the energy concentration is magnified for the vortex length-scale.

The wavelet maps represent for each scale r the magnitude of $E(x_1, x_2)^r$ which, as stated before in section 2.4, it is the 2D counterpart of the LIM . Whereas, the numerator $(w_{1,2}^r w_{1,2}^{r*} \cdot w_{2,1}^r w_{2,1}^{r*})^{1/2}$ represent in some way the cross-energy density of the two signal examined, which in this case are the signal of velocity component U sampled in the y -direction and the signal of velocity component V sampled in the x -direction, respectively.

3 Wavelet based code validation

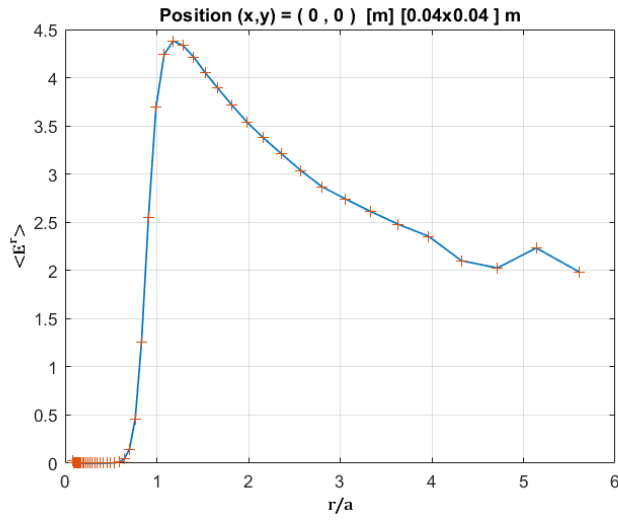


Figure 3.2 - $E(r)$ plot which indicates the length-scale of the detected vortex.

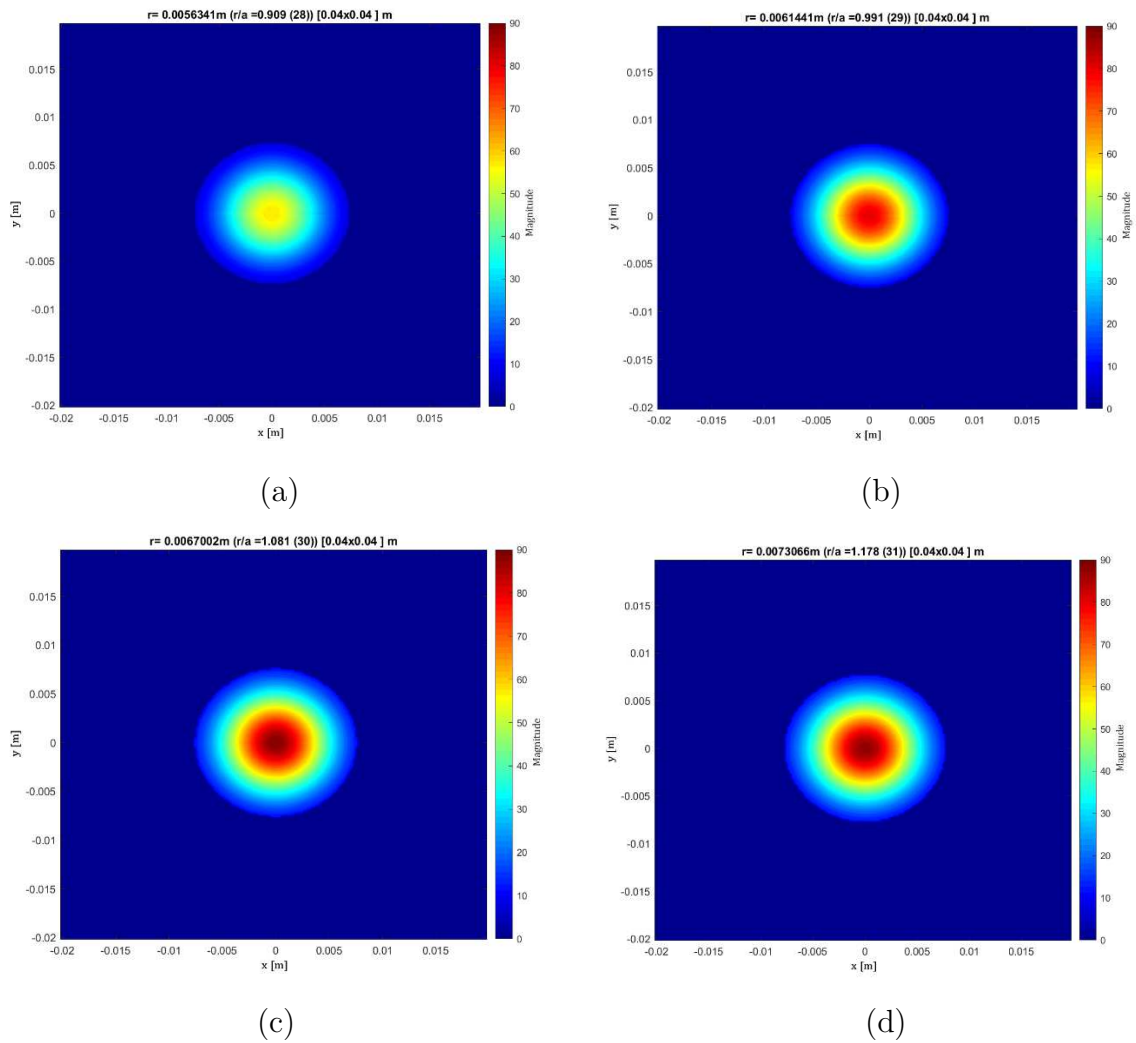


Figure 3.3 - Wavelet maps at four increasing scales show a maximum value of energy at the scale corresponding to the vortex length-scale.

3.2 The round jet

3.2.1 Jet description

The round jet is one of the most studied flow fields. The experimental configuration lies in a fluid flowing out, through a nozzle of diameter d , into an ambient with same fluid, which is at rest. Downstream of the nozzle, three regions can be distinguished, according to the behavior of the fluid (see Figure 3.4).

The first region is known as **potential core** and it extends from the exit to the distance of about $5 \div 6$ diameters ($0 \leq x/d \leq 6$). It consists of a nearly flat velocity profile with centerline velocity U_c corresponding to the exit velocity U_j .

The second zone is the **transition region** extending approximately to 15 diameters ($6 \leq x/d \leq 15$). In this region the center velocity, along the x-axis, begin to decrease and the previously formed structures evolve and interact.

The third and last region is the **self-similarity region**. This is the fully developed region where, with the appropriate scaling, velocity profiles all collapse into a single curve.

Of course, the indicated ranges can vary according to different Reynolds numbers.

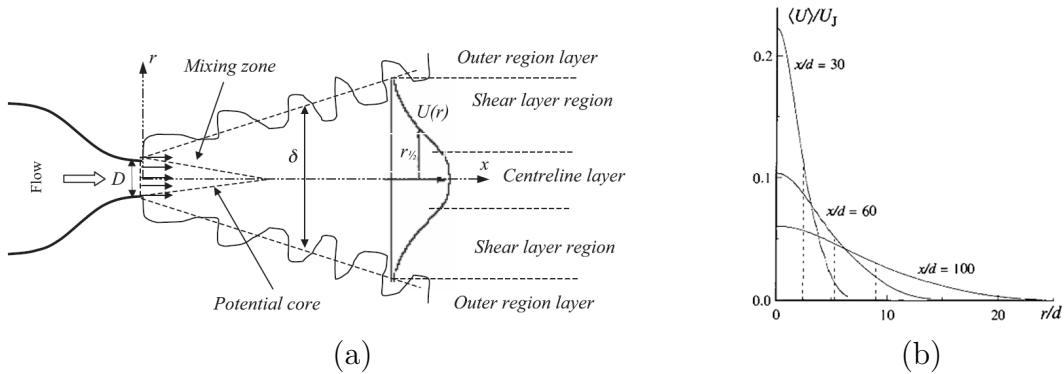


Figure 3.4 - (a)A schematic view of typical round jet flow field and (b) the mean axial velocity profiles for round jet $Re = 95500$ at different distance x/d from the nozzle exit (Ref. [6]).

A commonly used characteristic length in order to define the jet width going downstream, is the half-radius $r_{1/2}$, defined as the radius where velocity reach $U_c/2$. Downstream, fluid is entrained due the turbulent nature of the flow, so the mass flux of the jet increase, whereas momentum flow rate is almost conserved, since the jet is not subjected to external forces.

The initial instability at the end of the nozzle exit produce vortices in the shear layer. They evolve as depicted in Figure 3.5, where we can see the rolling and then pairing of these vortices [8].

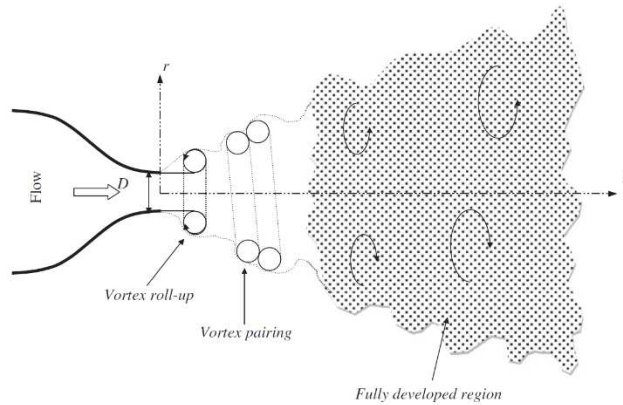


Figure 3.5 - Evolution of structures created at the nozzle exit.

3.2.2 Coherent structures in a turbulent round jet

Jet flows are characterised by large-scale structures which are generated at nozzle exit and advected downstream. These structures start to shape due to the instability of the shear layer which is formed by the interaction between the high-speed fluid issued by the jet nozzle and the free irrotational ambient fluid. The coherent structures obtained are *vortex rings*. In a longitudinal cut plane, it appears as two rolling up vortices near the nozzle just outside the potential core (see Figure 3.6(a)). Field perturbations and motions induced in the fluid by each vortex affect other vortices which begin to pair off giving birth to the *vortex pairing* process. After that, the ring vortex motion develops a circumferential wave instability which causes the vortex break up (see Figure 3.6(b)). Indeed, once the vortices begin to merge each other and constitute larger structures, at least as far as the end of potential core region, they break up into finer scale structures. Moreover, stream-wise counter-rotating structures was observed near the potential core, between successive vortex rings, which are formed due to secondary instabilities.

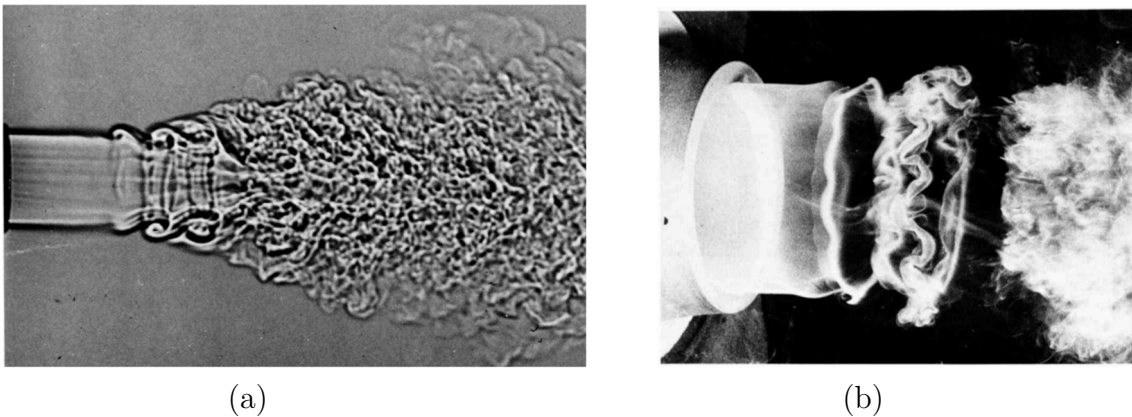


Figure 3.6 - (a) $\frac{1}{4}$ -inch round jet of CO_2 issuing into air at 38 m/s at a Reynolds number of about 30000. About one diameter downstream it shows instability, formation of vortex rings and transition to turbulence; (b) Wavy Instability and vortex rings breakdown in a round jet. (Ref. [2]).

3.2.3 Experimental set-up

The study is initially conducted in the **potential core** region, in the range $0 \leq x/d \leq 2$. The jet diameter is $d = 20 \text{ mm}$ and the velocity $U_J = 12.5 \text{ m/s}$. Since the Reynolds number is defined to be $Re = U_c d / \nu$, it results $Re = 16500$. The results are discussed in Section 3.2.4. The velocity fields are obtained by means the *Particle Image Velocimetry* (PIV) technique. Thus, we obtain two velocity components: U is the longitudinal component (x-axis component) and V is the vertical component (in this case the radial ones). A schematic view of the PIV set-up is reported in Figure 3.7.

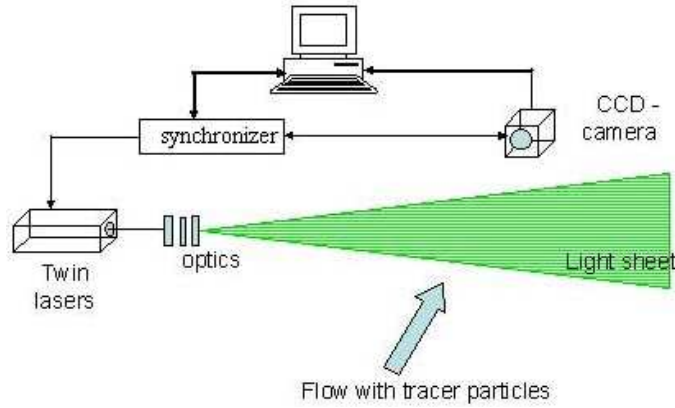


Figure 3.7 - Representation of the PIV set-up. The CCD-camera catches the flow field and the tracing particles enlightened by the laser sheet, flashing at a known frequency, at two different moment with a known time interval thanks to a synchronizer. Later, the two images are compared and from particles displacement velocity components are retrieved.

The laser plane is parallel to the longitudinal axis, so we obtain a lateral view of the jet.

Afterwards, a new set of PIV images of a jet flow field are analysed. In this case, the flow field extends to the **transitional region** in a range of about $0 \leq x/d \leq 8$. The jet diameter is, same as above, $d = 20 \text{ mm}$ and the Reynolds number reaches the value $Re \simeq 18000$ with $U_J = 13.5 \text{ m/s}$. The results are presented in Section 3.2.5. The number of pixels per unit distance, the distances Δx and Δy between two samples and other data are summarized in Table 3.1.

	<i>Pixel/mm</i>	<i>N° of samples</i>	<i>Field extension</i>	$\Delta x \mid \Delta y$ (mm)
Jet 1	60	359x425	$0.005 \leq x/d \leq 2.125$ $0.005 \leq y/d \leq 1.795$	0.1/0.1
Jet 2	-	336x1654	$0 \leq x/d \leq 8.268$ $-0.885 \leq y/d \leq 0.79$	0.1/0.1

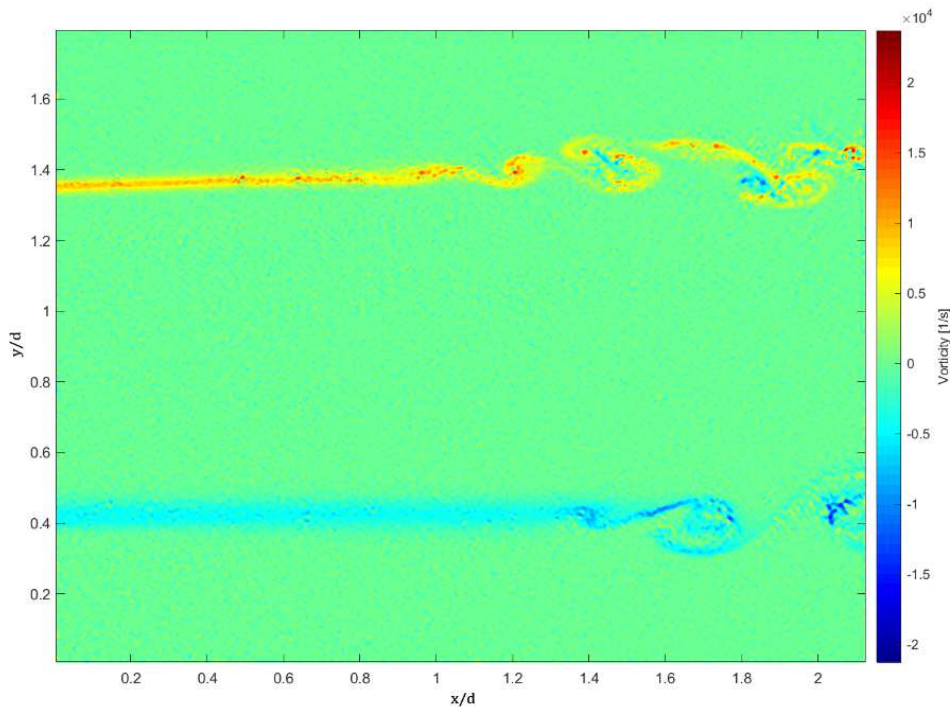
Table 3.1 - Data of round jet PIV images with $d = 20 \text{ mm}$

3.2.4 Wavelet analysis near the potential core

The procedure of the analysis is described in section 2.4 and the adopted method to evaluate length-scale r is reported in Section 1.2. We underline that the spatial resolution of the wavelet, as described in Section 1.2, corresponds to the spatial length-scale.

The study is carried out over many PIV snapshots in order to evaluate whether one or more structures are retrieved within the analysed domain. Indeed, within some snapshots no vortices were retrieved. Results for some of the processed images are showed below.

In Figure 3.8 the vorticity field and the velocity fluctuation plot are reported. The nozzle exit is placed on the left side of both figures, so the fluid flows from left to right. As can be seen from Figure 3.8(b), some structures are evident, so we can use this flow field to begin the code validation.



(a)

Figure 3.8 (a) - For caption see next page

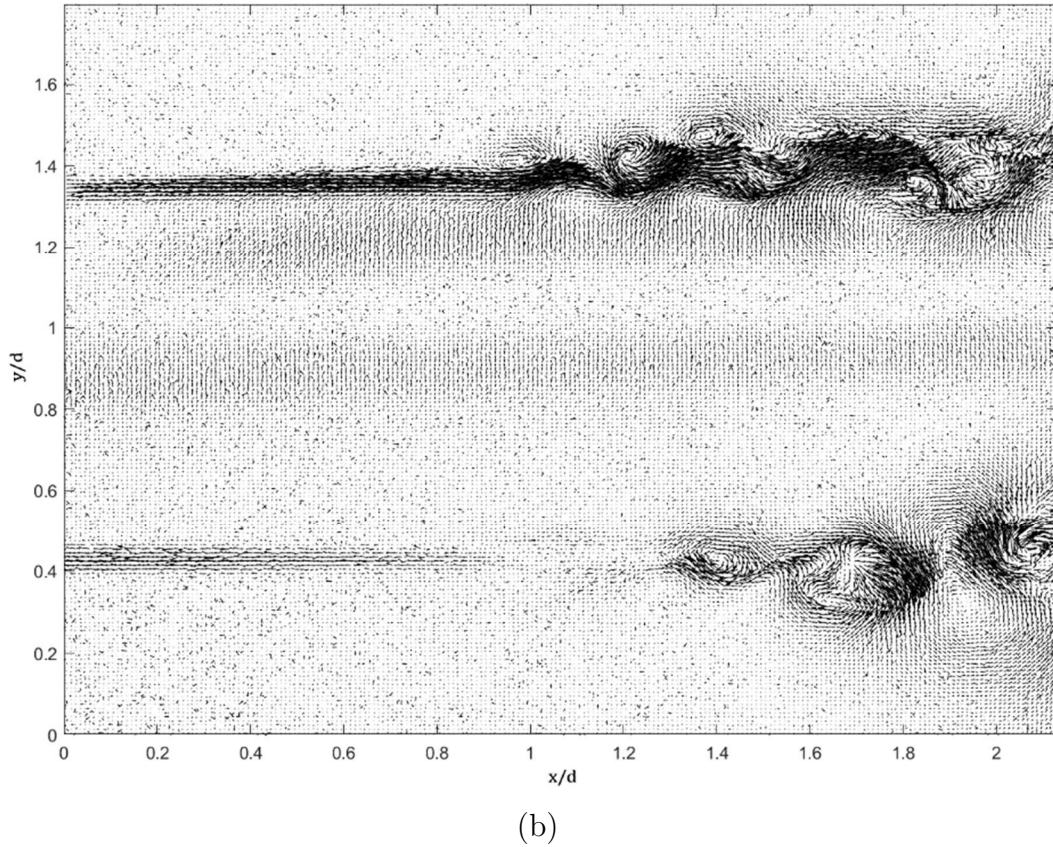


Figure 3.8 - (a)The vorticity field and (b) velocity vectors of fluctuating component of velocity obtained through Reynolds decomposition, which show the presence of different structures.

Once the energy map $E(x, y)^r$ of the complete flow fields is computed a local examination of the field is performed. A window of defined dimensions is slid along the entire field and for each window position, depicted in Figure 3.9, the $E(r)$ graphic is computed by evaluating the space average over the selected window for each scale, as the equation (2.11) states.

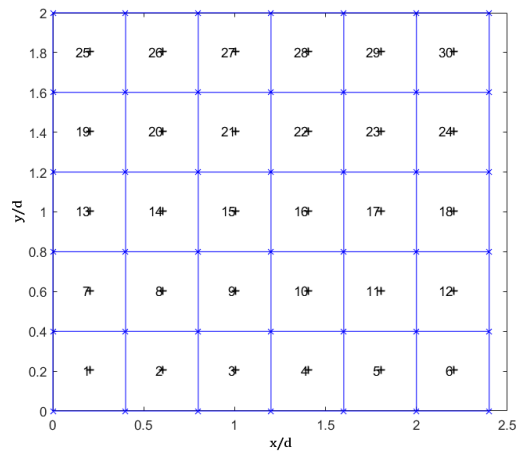


Figure 3.9 - The grid shows the various position reached by the sliding window.

Regions not interested by the presence of vortices show very low level of energy without any kind of peak in the $E(r)$ plot, like the cell 20 (see Figure 3.10(a)) where some energy is detected, but at very low level and without remarkable peaks. Otherwise, one absolute maximum or more relative maximums indicates the presence of one or more structures inside the examined window (see Figure 3.10) at a

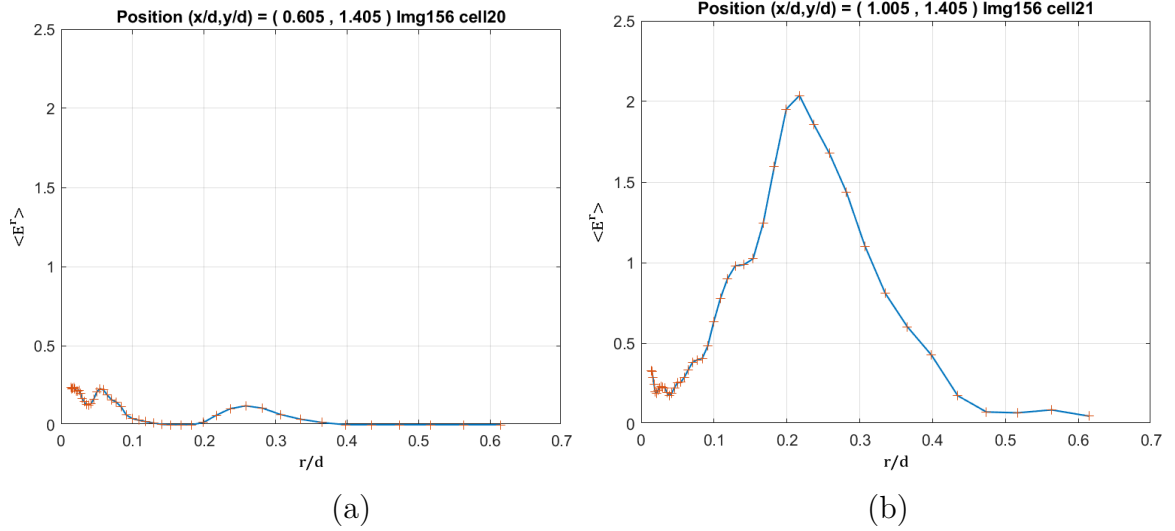


Figure 3.10 - The $E(r)$ plot shows the mean value of the energy over (a) cell 20 and (b) cell 21 for each scale.

specific length scale r/D . In fact, the energy content is maximized for that resolution.

Considering the plot of Figure 3.10(b), the presence of one maximum is related with the presence of one or more structures inside the selected window, in this case cell 21. Why do we say “more structures can be associated also to a single maximum”? Within the reference [7], it is stated that one absolute maximum coincides with one structure. But, if two structures inside the same window have the same length scale (or nearly the same), they will have an energy peak for the same scale contributing to the same maximum. This is because of the definition of $E(r)$; indeed, it is an average of the energy enclosed in the selected region. Thus, the localization characteristic is slightly lost. At that point, in order to have a better understanding of what is enclosed within the window, we need to visualize the energy map $E(x, y)^r$ for values of scale around the peak. This way, if more than one structure is included, we will see them. Indeed, for cell 21 at the scale corresponding to the peak at $r/d = 0.2$ the map showed in Figure 3.11(a) is obtained.

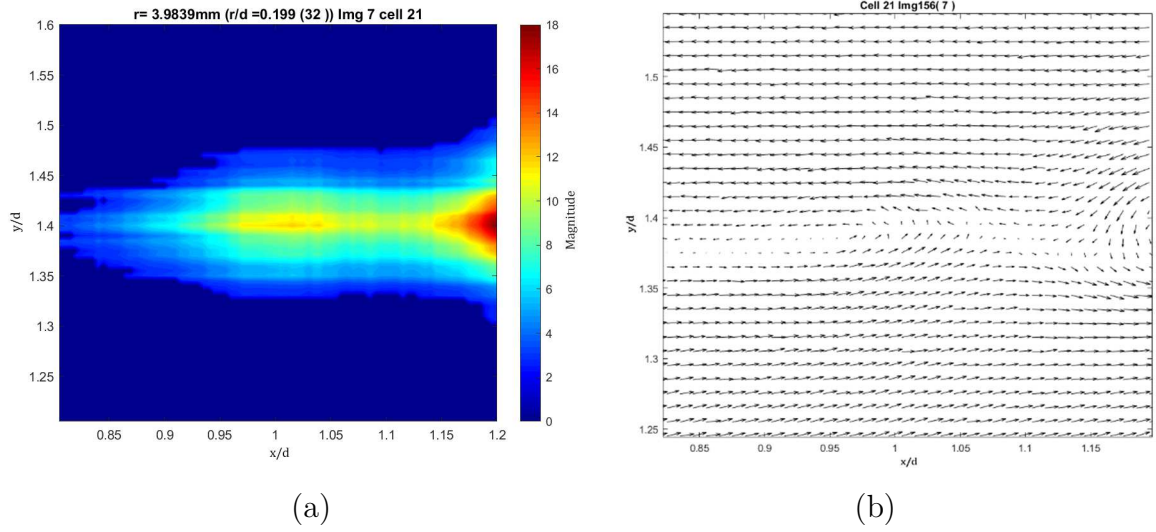


Figure 3.11 - (a) Contour map of $E(x, y)^r$ for the selected cell 21 at scale $r/D \approx 0.2$; (b) the Galilean transform of the velocity field. Two structures are visible. The one on the centre appears to be deformed and a little bit stretched and seems to be the end of a rising shear layer where we hypothesize, a streamwise structure, probably is formed.

With the purpose to confirm what the $E(x, y)^r$ map is showing the Galilean transform of the velocity field in the same cell is evaluated (see Figure 3.11(b)) with a convective velocity U_a equal to half the jet velocity U_J (the same result can be achieved through the visualization of the fluctuating component of the velocity fields).

The central structure enlightened in Figure 3.11(a) has a non-defined shape, as we can see from the Galilean transform. Because of this type of structure is present in many other images, we can hypothesize that it corresponds to a section of a streamwise vortex, but with PIV data in our possession it isn't possible to obtain an indisputable confirmation.

At this stage, we focus our attention on the right vortex presented in Figure 3.11 which results well defined. We center the window on this structure, in order to isolate it from the second vortex, and we obtain the map and the $E(r)$ plot reported in Figure 3.12.

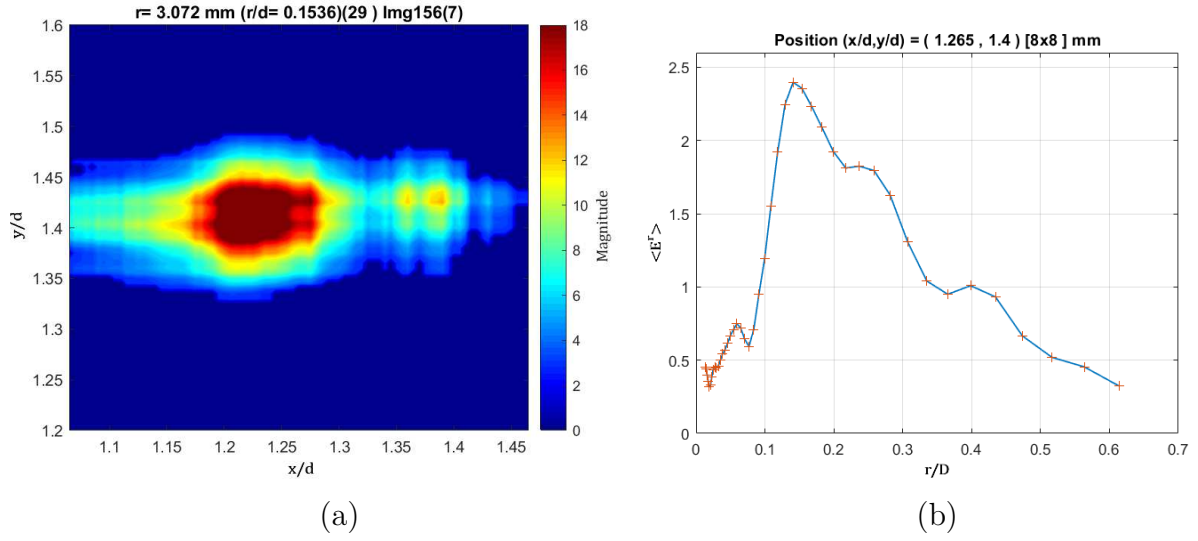


Figure 3.12 - (a) Energy map, (b) and $E(r)$ plot of a selected vortex.

As we can see, the length-scale at which the energy content is magnified is $r/D \simeq 0.15$ and it should correspond approximately to the size of the vortex. Since the nozzle diameter is $D = 20 \text{ mm}$ the resulting size is about 3 mm . Comparing this value with the Galilean transform in Figure 3.13, that value almost matches the effective size of the vortex. The second vortex of Figure 3.11 has a peak in the $E(r)$ graphic at $r/D \simeq 0.2$ and it corresponds to the width of the stretched vortex.

In Figure 3.12(a), on the right side of the bigger area of energy, we can see a small area with a significant energy magnitude. Navigating through the energy maps $E(x, y)^r$ at different scales, another not well defined small structure is found, which has a peak for the energy magnitude at scale of about $r/D \simeq 0.13$ resulting in the effective size of about 2.6 mm . This can be confirmed through Figure 3.13 where the Galilean transform is reported.

As remarked before, the $E(r)$ graphic is obtained through an average over the area selected losing some localized information. Thus, if we visualize the energy map for each scale, we can find at which one the energy content is magnified and so the characteristic length scale of the structure is retrieved.

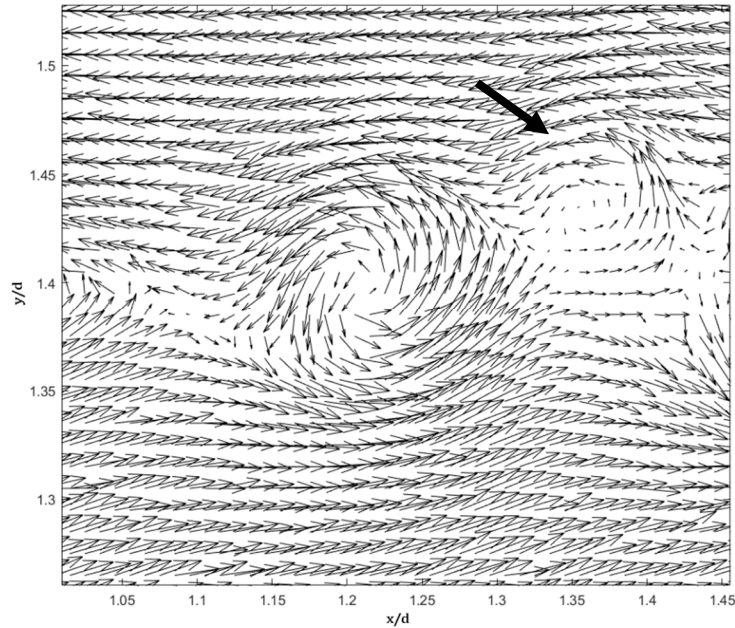


Figure 3.13 - (a) Galilean transform with convective velocity equal to half the jet velocity on the x -axis. The small structure is pointed with an arrow.

Now, a global view of the flow field is given with the purpose to visualize all the energy concentrations for each scale and compare them with the Galilean transform. This way, we are able to associate the presence of a possible vortex with the “local energy”. Later, a more accurate method will be adopted for comparison.

Considering the same PIV snapshot as above, we examine four wavelet maps at the related resolutions which emphasise vortices’ presence. In Figure 3.14(b) and Figure 3.14(c), vortices 1, 2 and 3 are clearly visible, while we can discern the small amount of energy indicated with number 5 which corresponds to the small structure of Figure 3.12. Moreover, in the lower side two other regions are indicated with 4 and 6.

An interesting thing comes from the Figure 3.14(a) which present the local energy for a small resolution. The small illuminated areas are all divided, but if we look at them “globally” we see they are located in regions where vortices are detected. Thus, this small energy concentrations can represent the small irregularities and vorticity concentrations that constitute the bigger vortices. Within the circled area there must be something. As can be seen from the Galilean transform images of Figure 3.15(b), there are some not well identified structures which from wavelet analysis are not well retrieved. However, Figure 3.15(a) as well Figure 3.13 show a great matching between the wavelet maps and the velocity vector field.

3 Wavelet based code validation

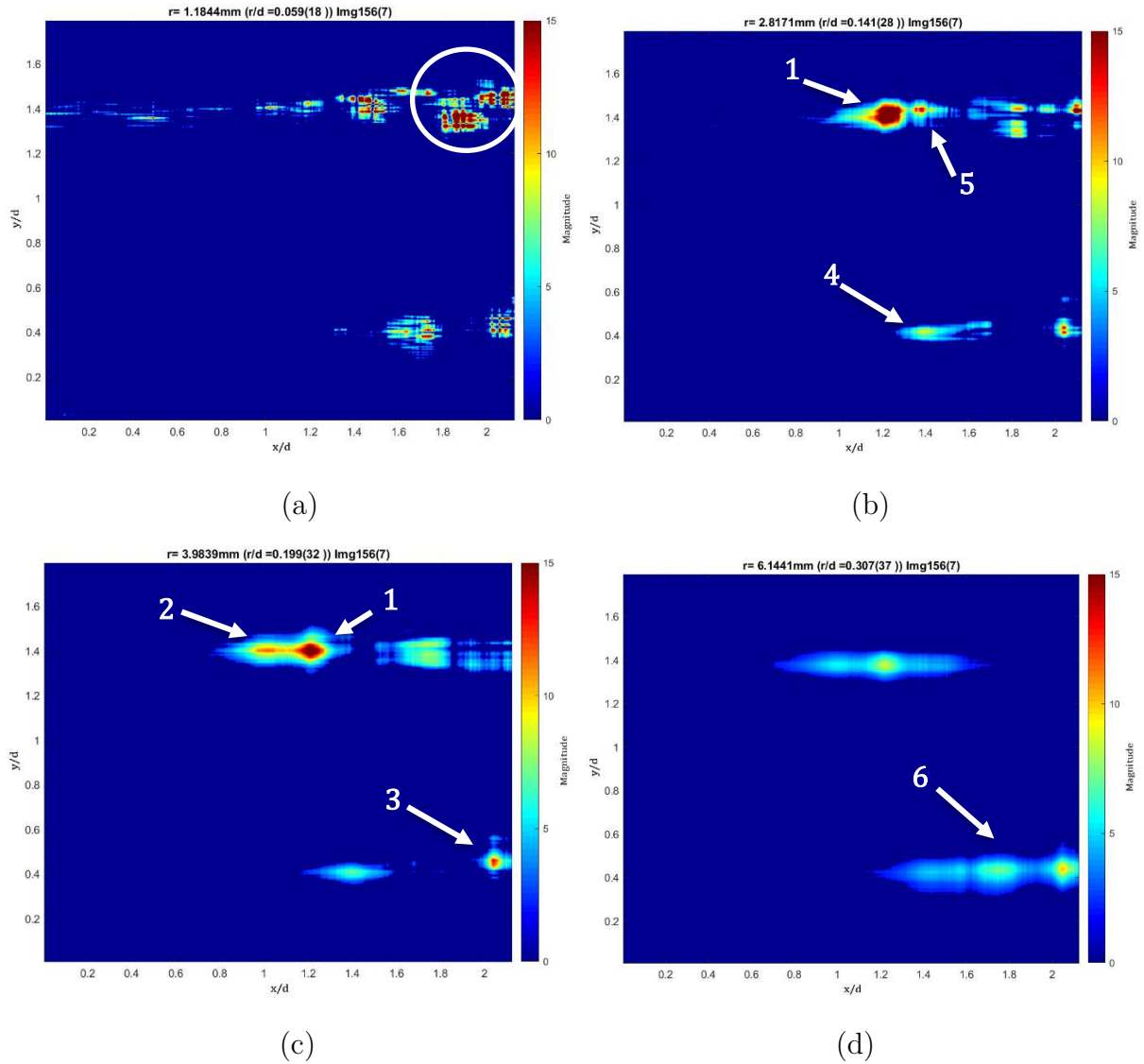


Figure 3.14 - Four energy maps (or wavelet maps) showing possible vortices at different resolution.

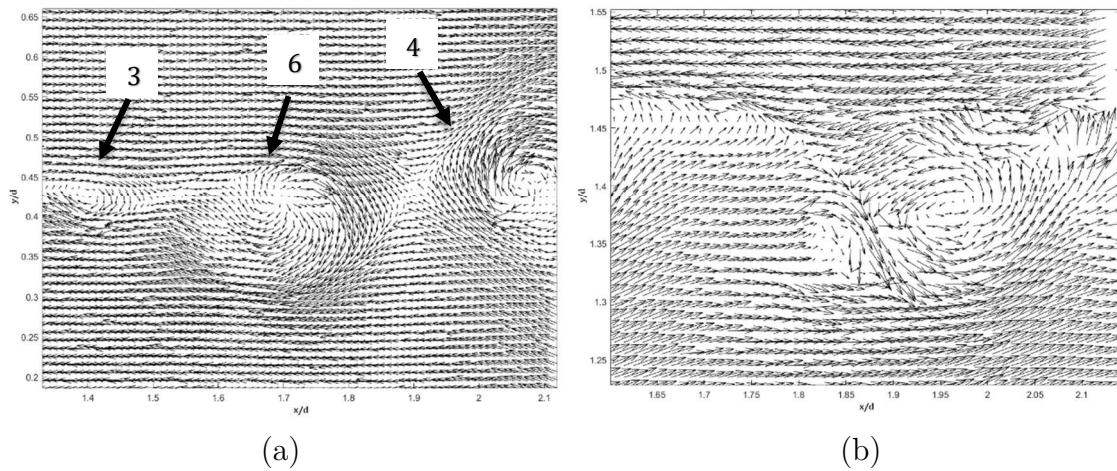


Figure 3.15 - (a) Three vortices (3,4 and 6) on the lower side of the flow field; (b) the area in the upper-right side of flow field marked with a white circle in Figure 3.14(a).

Now, results of another analysed snapshot are presented which show a very interesting outcome.

The flow field reported in Figure 3.16 is obtained through a Galilean transform adopting an advective velocity U_a equal to half the jet velocity U_J . What appears very clear is the presence of one counter-clockwise rotating coherent structure in the region labelled as A and a second clockwise structure in the region C which both corresponds to a section of vortex-rings. Very remarkable is what appears in the region C. Indeed, we can see two coherent structures pairing off.

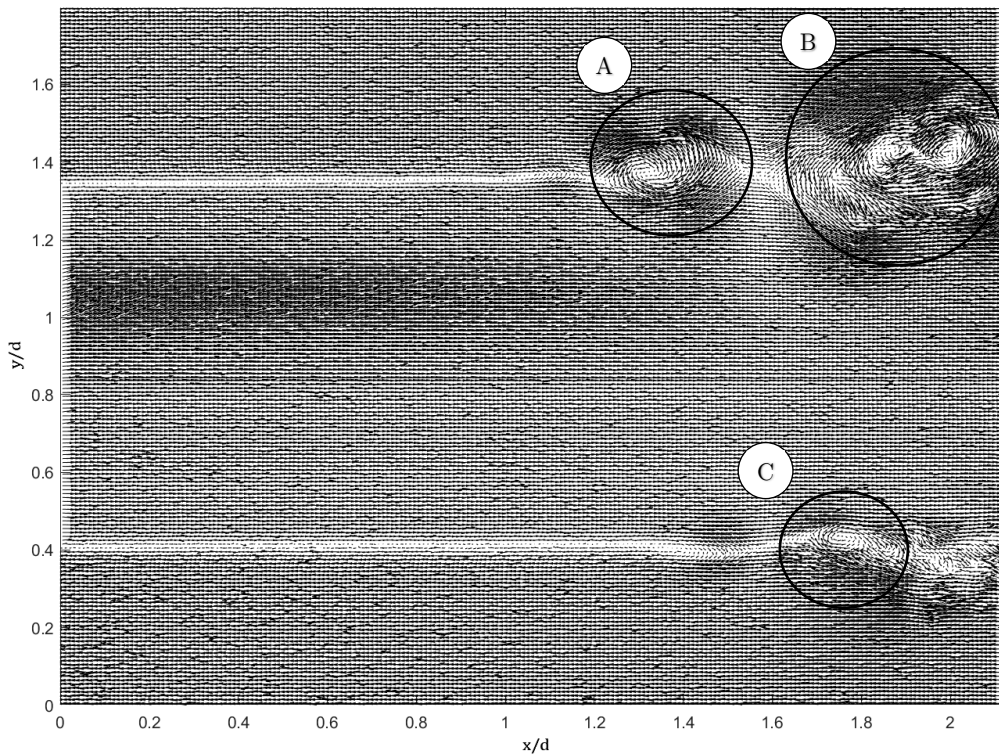


Figure 3.16 - Velocity vectors' field obtained by means Galilean transform of the instantaneous velocity field. Different coherent structures are visible included the pairing process of two vortices in the area named as B.

In Figure 3.17 the wavelet maps at scales which highlight the various vortices are depicted. From the Galilean transformed PIV images, one can suppose that the flow field is animated by events of the same length-scale, but through the wavelet maps we can state that the flow field is actually multiscale which contains various coherent structure at different length-scale.

If we superimpose the Galilean vector field onto the wavelet maps, we discover a perfect matching between vortices and enlightened areas of the wavelet maps (see Figure 3.18).

3 Wavelet based code validation

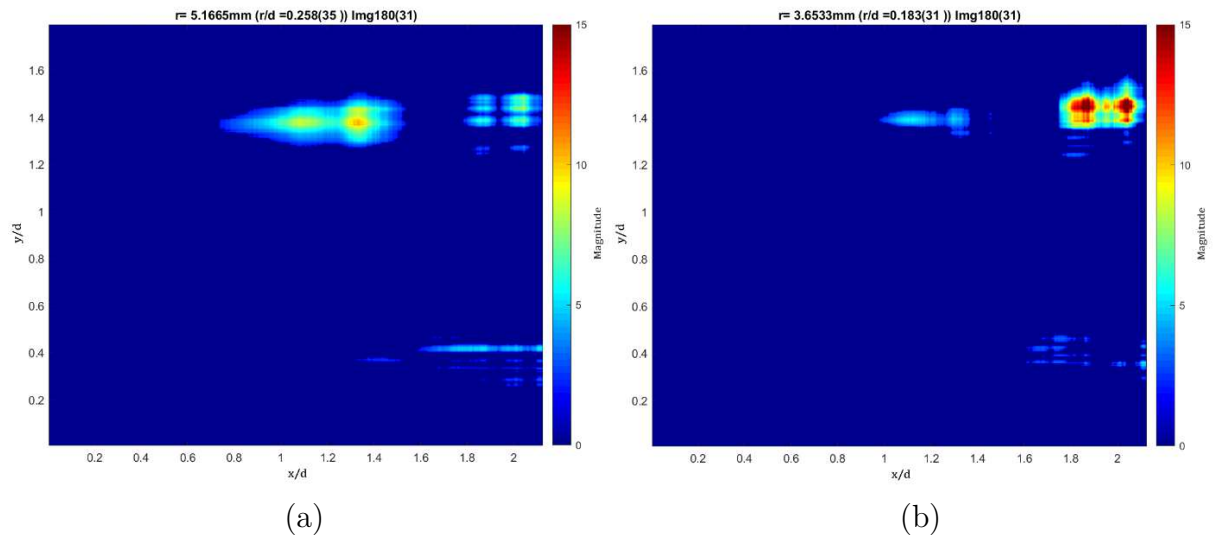


Figure 3.17 - The wavelet maps show (a) the vortex over the region A which is preceded by a “stretched” structure and (b) two vortices of the region B where the pairing process is going on.

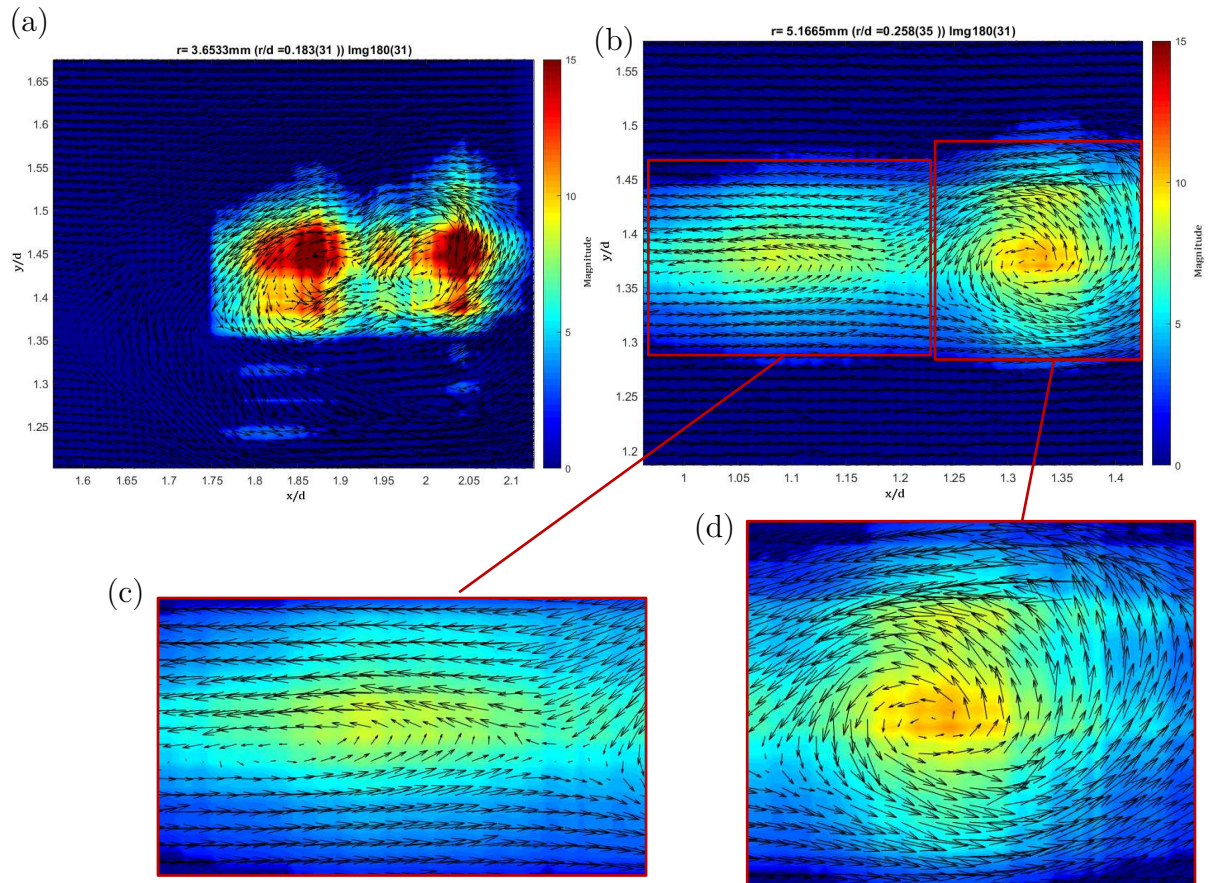


Figure 3.18 - Galilean vector field with $U_c = 0.5U_J$ superimposed onto the wavelet maps (a) for the region B and (b) for the region A including the preceding structure which are remarked in (c) and (d), respectively.

By the exam of Figure 3.18, we notice that for the two pairing structures (see Figure 3.18(a)) the maximum of energy is reached in positions slightly different of the precise vortex centre core and this was observed in many other images. The length-scale of these two structures is nearly the same with $r/d \simeq 0.18$.

The coherent structure of Figure 3.18(d) finds a perfect matching with the velocity vectors' field and the energy content rises at its maximum value for a resolution of $r/d \simeq 0.26$ which corresponds to the coherent structure's length-scale.

The structure highlighted by Figure 3.18(c) doesn't seem an azimuthal vortex, but the vectors' orientation could indicate a streamwise structure, although typical streamwise structure detected by flow visualizations are located between two succeeding vortex-rings.

The structures in the zone C are not well detected, that means there isn't a clear identification from the wavelet map. However, at low scale all the regions interested by vortices are spotted and small-scale "constituent" are visible all over that regions as can be seen from Figure 3.19.

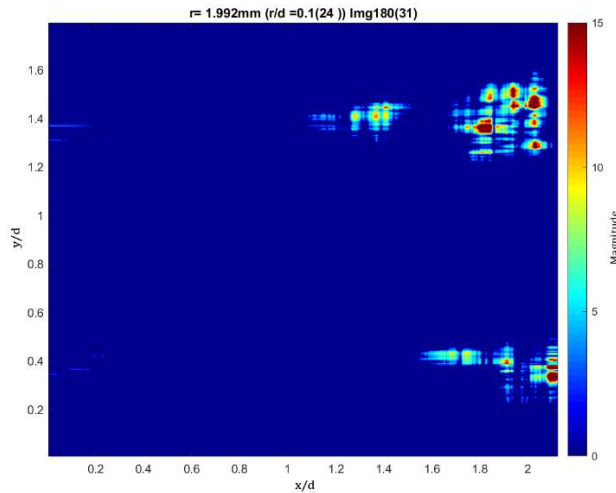


Figure 3.19 - Small scale wavelet map ($r/d = 0.1$) shows areas of the domain affected by vortices presence. The map is related to the PIV image of Figure 3.16.

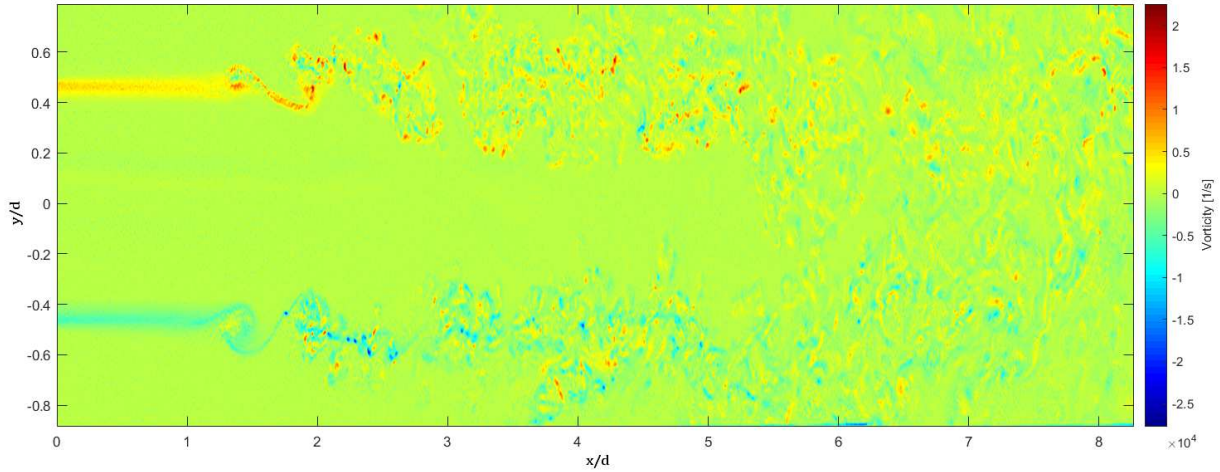
3.2.5 Wavelet analysis extended to the transitional region

In this section, the new set of PIV data extends in $0 \leq x/d \leq 8$ and results are presented ranging from potential core to transitional region.

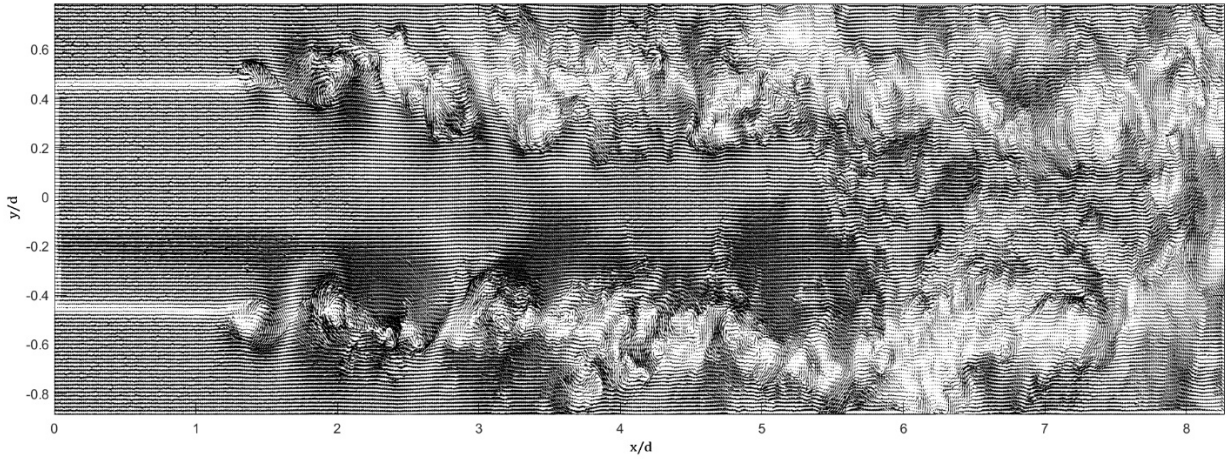
We begin analyzing the first snapshot whose vorticity and Galilean velocity field is depicted in Figure 3.20. The Galilean transform is performed with a convective velocity value U_a equal to half the jet velocity U_J whose value is around 13.5 m/s .

With the purpose to analyze the entire field the following procedure is applied:

- The wavelet transform is performed over the complete flow field, so energy map (or wavelet map) is obtained for each scale (or resolution).
- A threshold is set for energy; only energy which overcomes that threshold is considered. In the present case the threshold is set at two times the standard deviation over the whole flow field at each scale.
- The entire area is scanned by means an $8 \times 8 \text{ mm}$ matrix window within which the $E(r)$ graphic is evaluated for each window's position.
- By the $E(r)$ plot and related energy map examination possible vortex or coherent structures are identified.
- To confirm the presence of structures the Galilean transform and the λ_2 -Criterion (described in Section 2.2) are applied to the selected window.



(a)

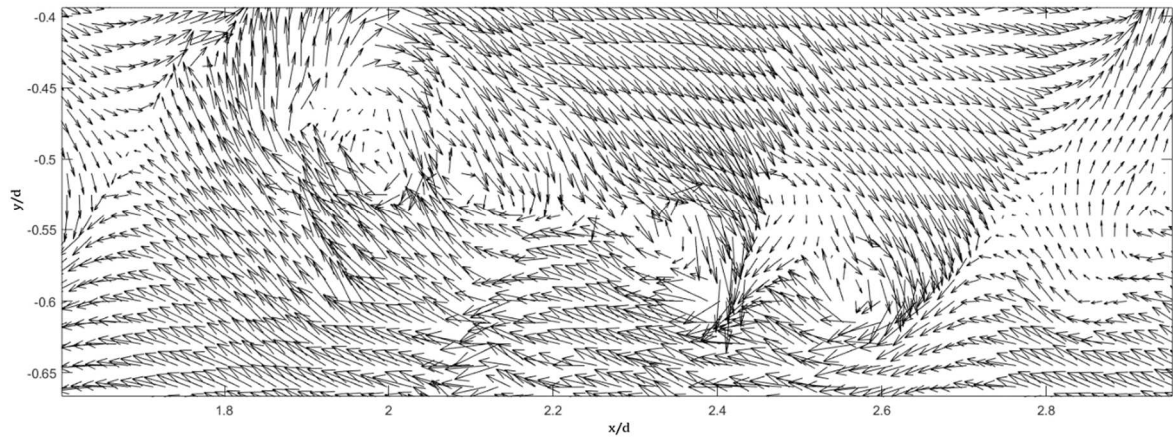


(b)

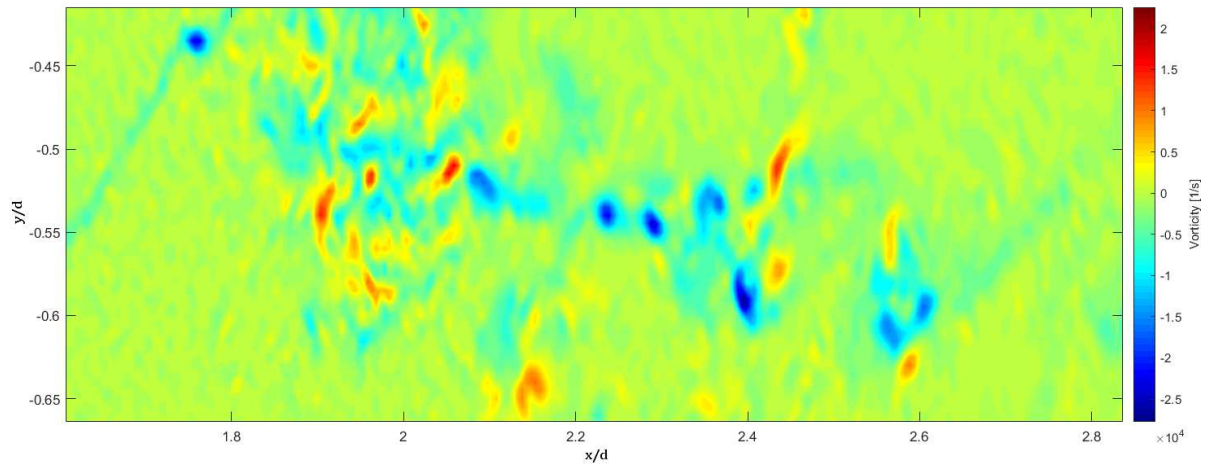
Figure 3.20 - Motion field of selected PIV snapshot's, (a) vorticity field, (b) Galilean transform of velocity field with convective velocity $U_a = 0.5U_J$. Both images show the typical conformation of a jet, where potential core and transitional region are clearly visible. The jet issues from left to right with velocity equal to $U_J = 13.5$ m/s.

First of all, we choose a small flow region and we report the corresponding Galilean transform to physically visualize the velocity field conformation (see Figure 3.21(a)). Next, we compare that region's vorticity field with the λ_2 -Criterion and the wavelet map and a very interesting thing comes out. As can be seen in Figure 3.21, there is a great correspondence between the high vorticity areas, the isolines of λ_2 and the high energy regions at very small scale, which means high resolution. This confirm the definition of quantity $E(x, y)^r$ in Section 2.4 is associated with vorticity.

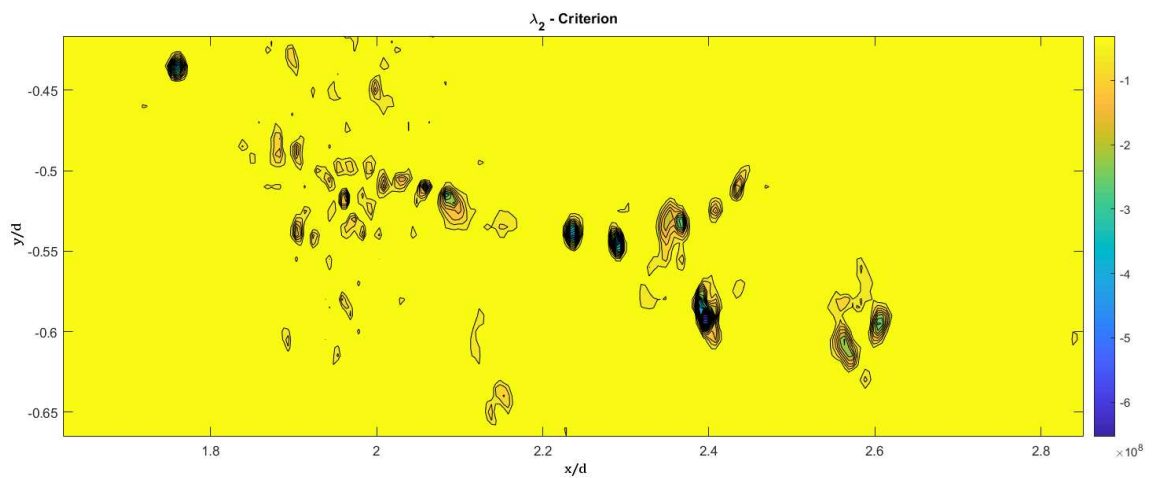
3 Wavelet based code validation



(a)



(b)



(c)

Figure 3.21(a)(b)(c) - For caption see next page.

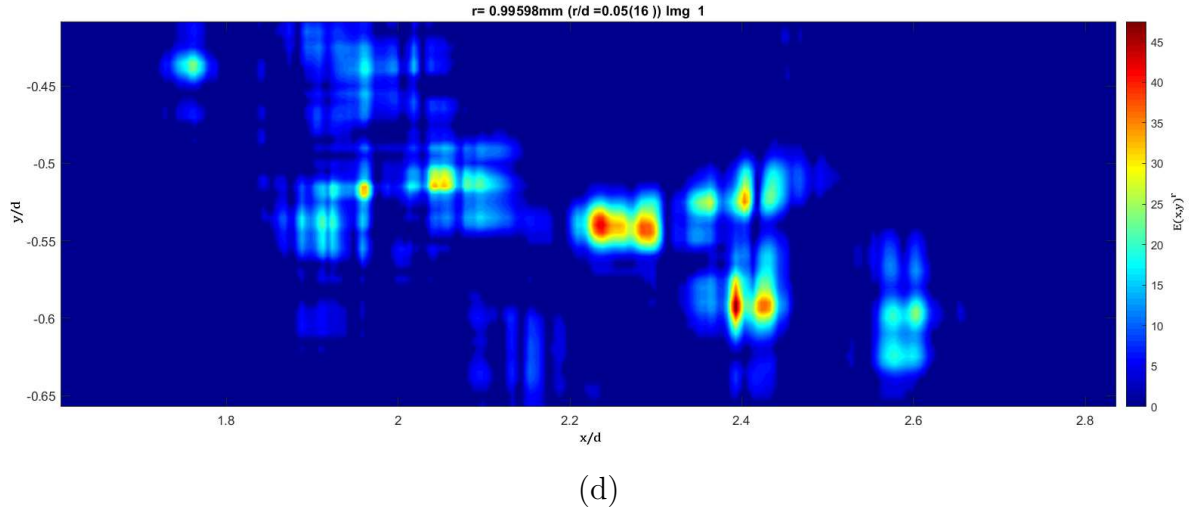


Figure 3.21 - Comparison of different methods used to retrieve vortices; (a) Galilean transform with convective velocity $U_a = 6.5\text{m/s}$ equal to half the jet velocity, (b) vorticity field (c) λ_2 -Criterion, (d) wavelet map at small scales.

One advantage of wavelet analysis with respect to other methods lies in the possibility to separate the energy content for each scale.

Now, the whole jet region is scanned by a sliding window (see Figure 3.22), as done before, and within each window the graphic $E(r)$ is computed. Results for significative windows are report below.

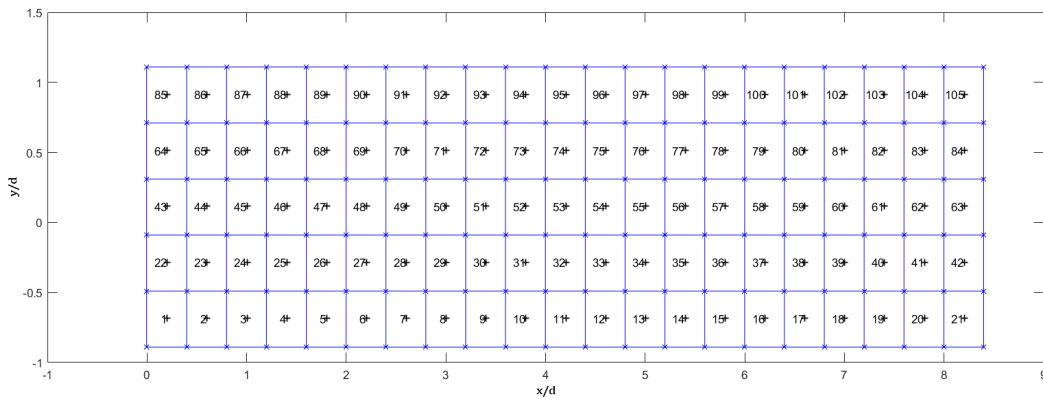


Figure 3.22 - Window position within jet flow field

Cell 7 ($x/d \simeq 2.6 - y/d \simeq -0.7$)

The $E(r)$ graphic obtained for this window is reported in Figure 3.23(c). As we can see, two peaks are evident, one at small scale ($r/D \simeq 0.06$) and one at larger scales ($r/D \simeq 0.25$). To understand what these peaks represent, it is always fundamental to visualize the wavelet map for each scale. Thus, the wavelet maps at scales' peaks are depicted in Figure 3.23(a) and Figure 3.23(b). If we look at the small scales' peak, we notice many little areas at very high energy content caused

by great values of the z-component of velocity curl, i.e. the z-vorticity. As showed before in Figure 3.21, all these areas represent high vorticity small regions which constitutes bigger ones or, probably, they also can be noisy areas within the turbulent flow. We can neglect values at scale smaller than $r/d \simeq 0.1$ as it has been done in Ref. [7]. So, we focus our attention on the second peak. There is an area of consistent energy content, which probably represents a vortex, surrounded by a low energy distribution. The Galilean transform and the fluctuating velocity (see Figure 3.24) show and confirm clearly the presence of a vortex in that area. Moreover, we have confirmation through the λ_2 -criterion. In Figure 3.23(d), the second eigenvalue of matrix $\mathbf{S}^2 + \mathbf{\Omega}^2$, namely λ_2 (see Section 2.2 for details), is represented by white isolines superimposed over wavelet map and it is clear the correspondence at small scales. The position of λ_2 isolines matches the location of vortices.

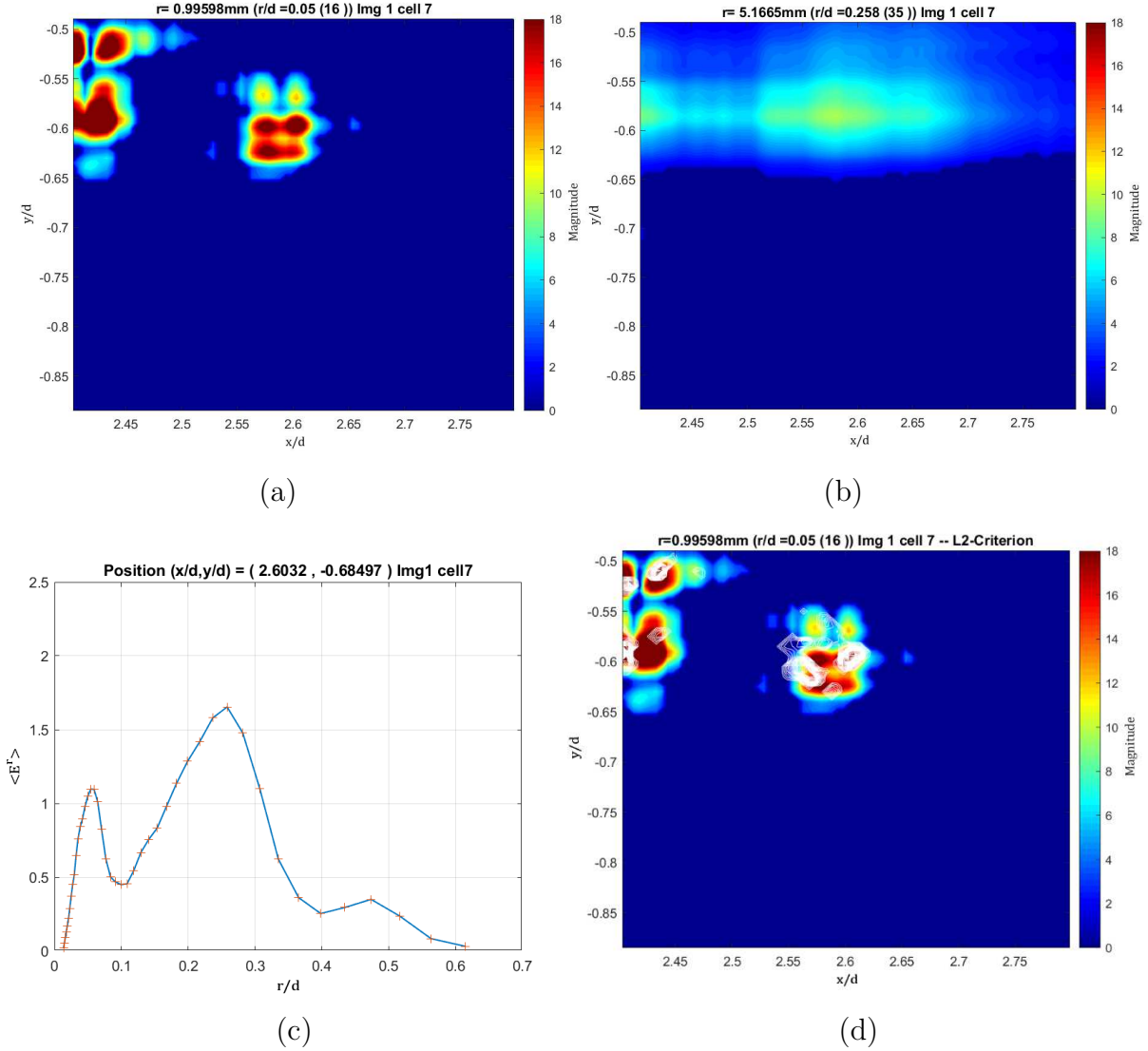


Figure 3.23 - (a) Wavelet map related to (a) first peak and (b) second peak of (c) $E(r)$ plot and (d) λ_2 isolines over small scales' wavelet map over cell 7.

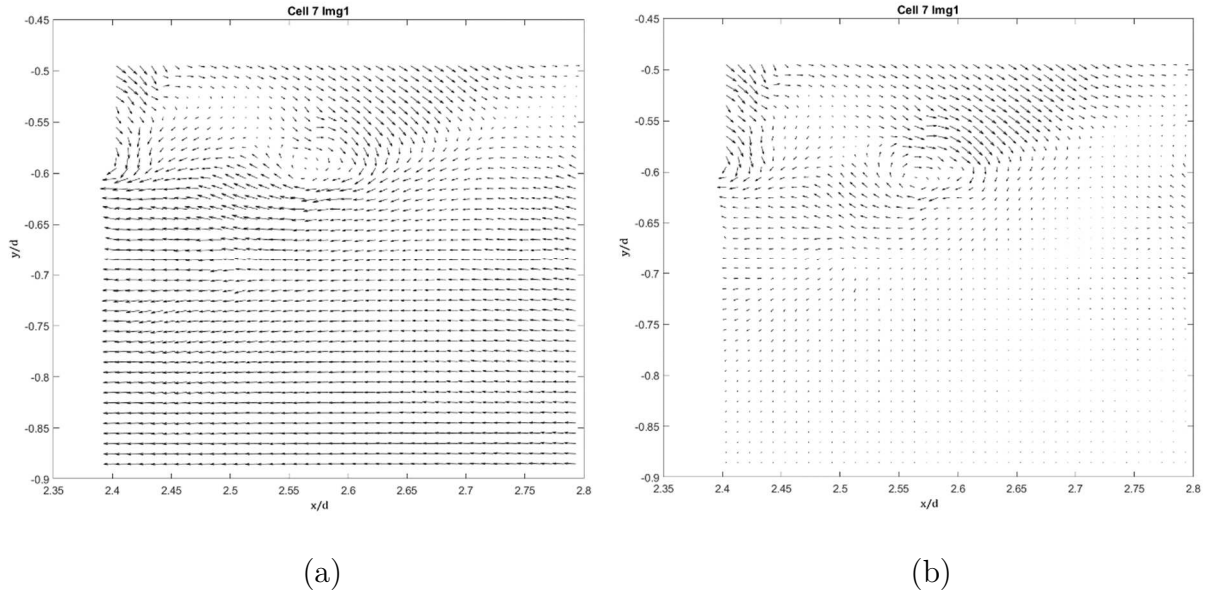


Figure 3.24 - (a) Galilean transform and (b) fluctuating velocity within window 7.

However, there is an uncertainty of which the correct scale of this structure is due to the following reason. The surrounding low-level energy is caused by the chaotic motion of the turbulent flow field and it must not be considered when defining the length scale. But, the $E(r)$ graphic is obtained, as more times remarked, by an average over the selected area, so, for example, we can obtain the same peak for a well localized high energy content and a distributed low energy area. Thus, the surrounding energy in Figure 3.23(b) contributes to the peak at $r/D \simeq 0.25$. To determine the correct length scale, we visualize the wavelet map for more scales around the peak (see Figure 3.25). As can be noted, the high energy area finds its maximum value for $r/D \simeq 0.2$. This value corresponds approximately with the vortex size visible in Figure 3.24.

Since a threshold was set for the energy, the problem of surrounding energy can be partially solved increasing that threshold. For the current cell, we increase the threshold value to 5. The resulting $E(r)$ graphic, depicted in Figure 3.26 has a lower peak than before because the amount of energy is smaller, and average is always made over the same area, but its position in terms of r/D is nearly the correct one. Thus, the peak has moved back from $r/D \simeq 0.25$ to $r/D \simeq 0.217$

3 Wavelet based code validation

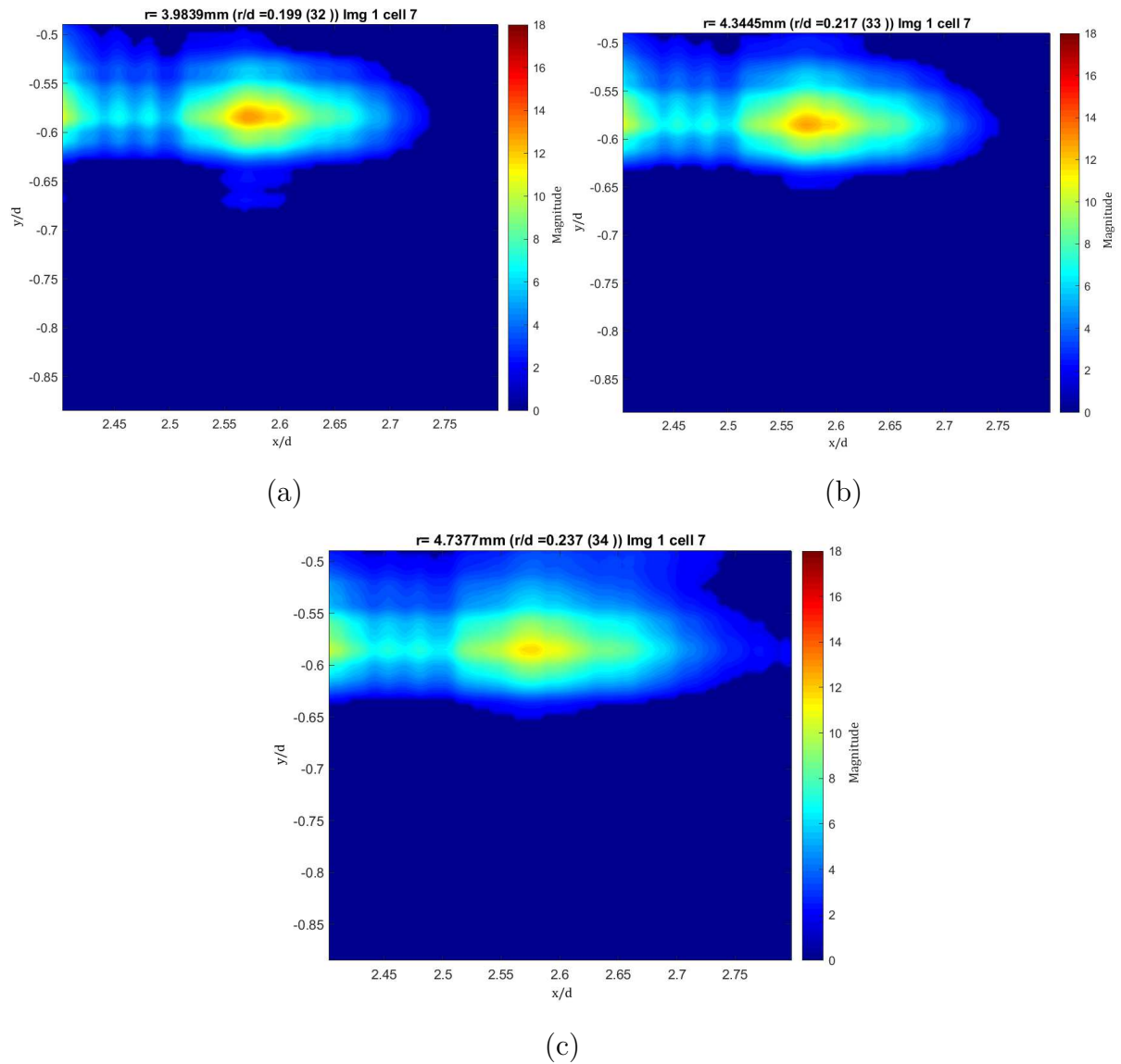


Figure 3.25 - Wavelet maps of cell 7 for three scales; the energy maximum is found for scales between (a) $r/D = 0.199$ and (b) $r/D = 0.217$ while for (c) $r/D = 0.237$ the energy decreases and the surrounding low energy is spreading.

3 Wavelet based code validation

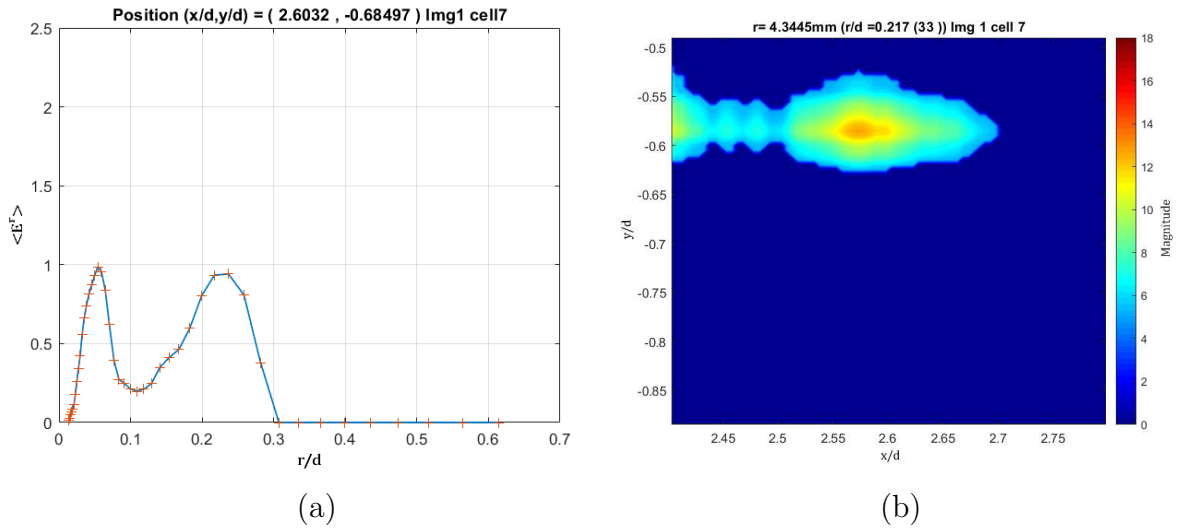


Figure 3.26 - (a) $E(r)$ graphic and (b) wavelet map of cell 7 with threshold increased to the value $Magnitude = 5$.

Cell 31 ($x/d \approx 3.8 - y/d \approx -0.3$)

In this area, we discover the presence of small scales structures. The $E(r)$ graphic, which we use as guideline, is reported in Figure 3.27(a) and a peak is evident. Thus, we examine the wavelet maps (see Figure 3.27) around the r/d value at which the peak is placed.

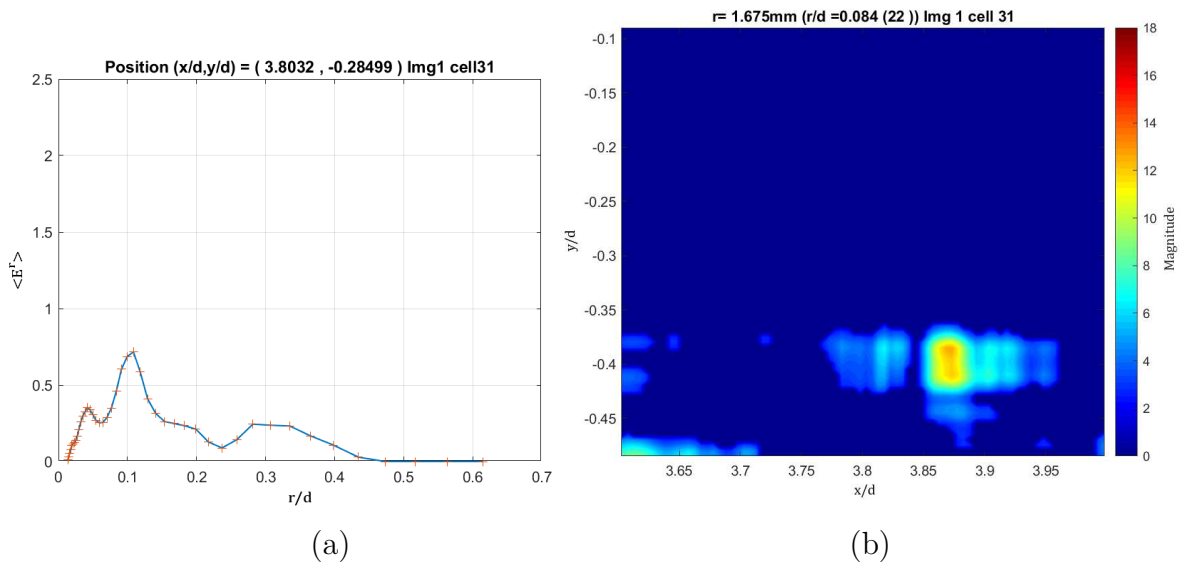


Figure 3.27(a)(b) - For caption see next page

3 Wavelet based code validation

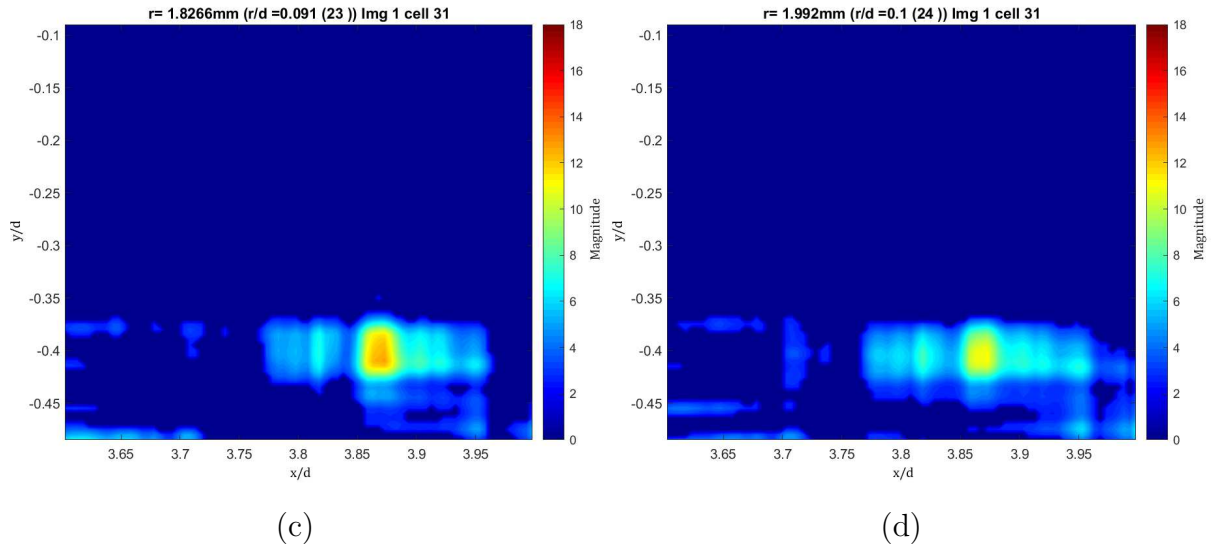


Figure 3.27 - (a) $E(r)$ plot which show a peak around $r/D \simeq 0.1$ and (b)(c)(d) wavelet maps at three scales near the peak of the $E(r)$ plot. The actual length scale is retrieved through the maps.

As previous case has showed, the energy maximum is obtained not exactly for $r/d = 0.11$, but for $r/d \simeq 0.09 \div 0.1$ as the wavelet maps show. Increasing the threshold value, the peak moves to the correct value in terms of length scale in the $E(r)$ plot and the wavelet map appears more clear (see Figure 3.28).

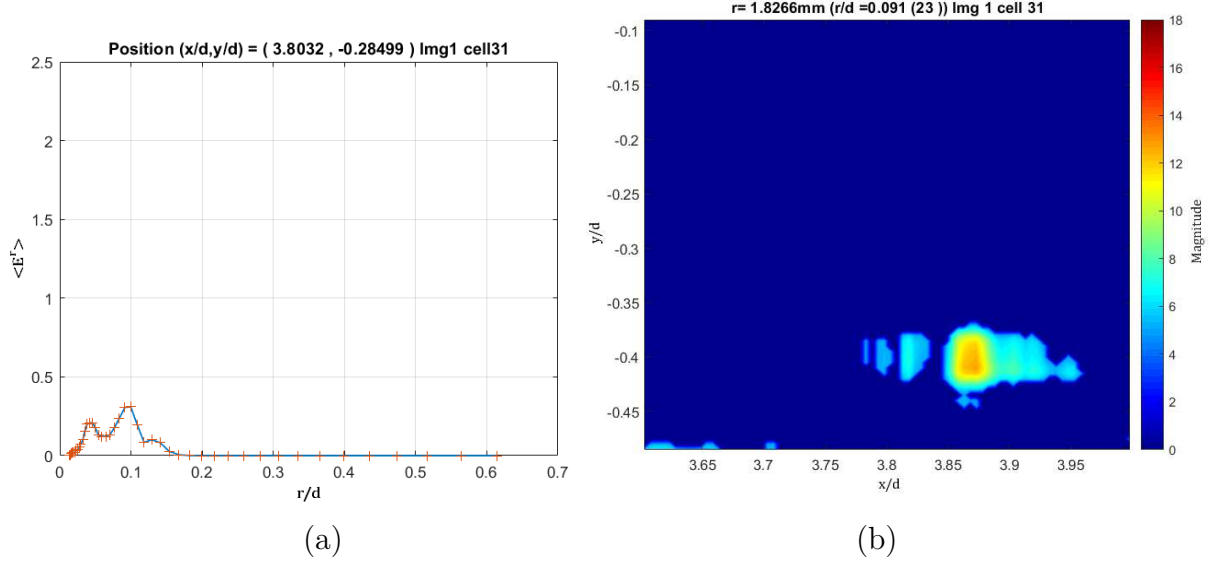


Figure 3.28 - (a) Graphic $E(r)$ and (b) wavelet map at scale relative to the $E(r)$ peak of cell 31 with an increased threshold to the value of Magnitude =5.

In order to have a basis for comparison, the velocity fluctuations are reported below in Figure 3.29 together with λ_2 -Criterion.

3 Wavelet based code validation

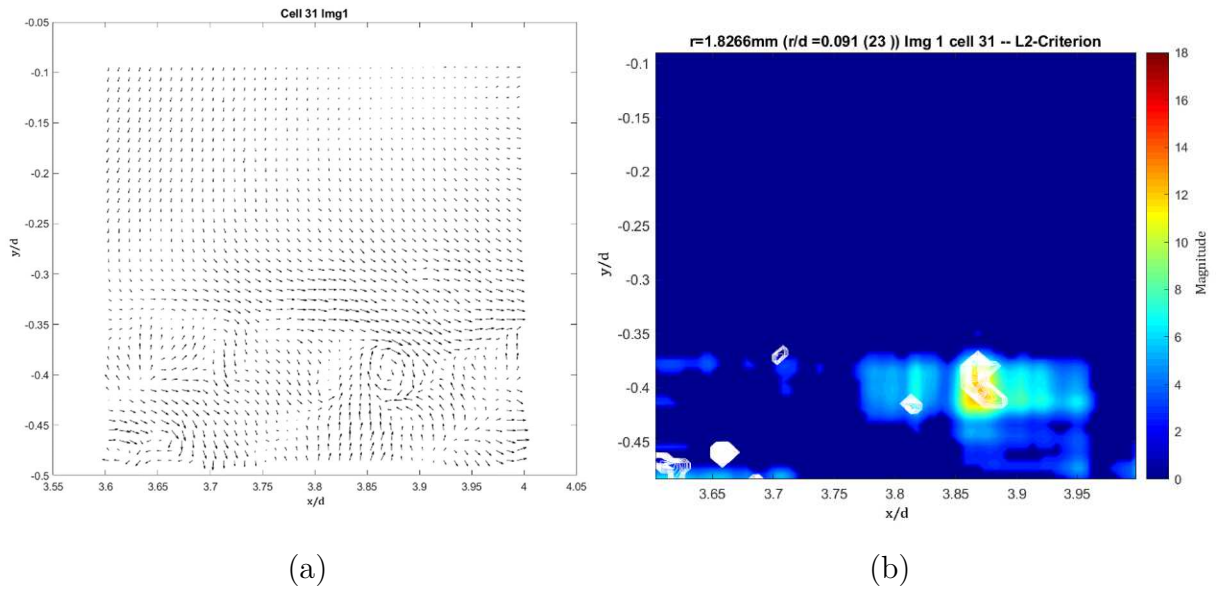


Figure 3.29 - (a) Velocity fluctuations and (b) isolines of λ_2 value superimposed to the wavelet map of cell 31 at the indicated scale.

Cell 37 ($x/d \simeq 6.2 - y/d \simeq -0.3$)

This window is located at the beginning of the transitional region. Here, we see from the $E(r)$ plot (see Figure 3.30(a)) two peaks and the first one is not so well defined. This peak's shape is due to the presence of two or more structures with a similar length-scale, i.e. navigating through the scales the smaller eddy is, initially, enlightened and then, increasing the scale value, its energy content start to decrease while the second slightly bigger eddy start to arise.

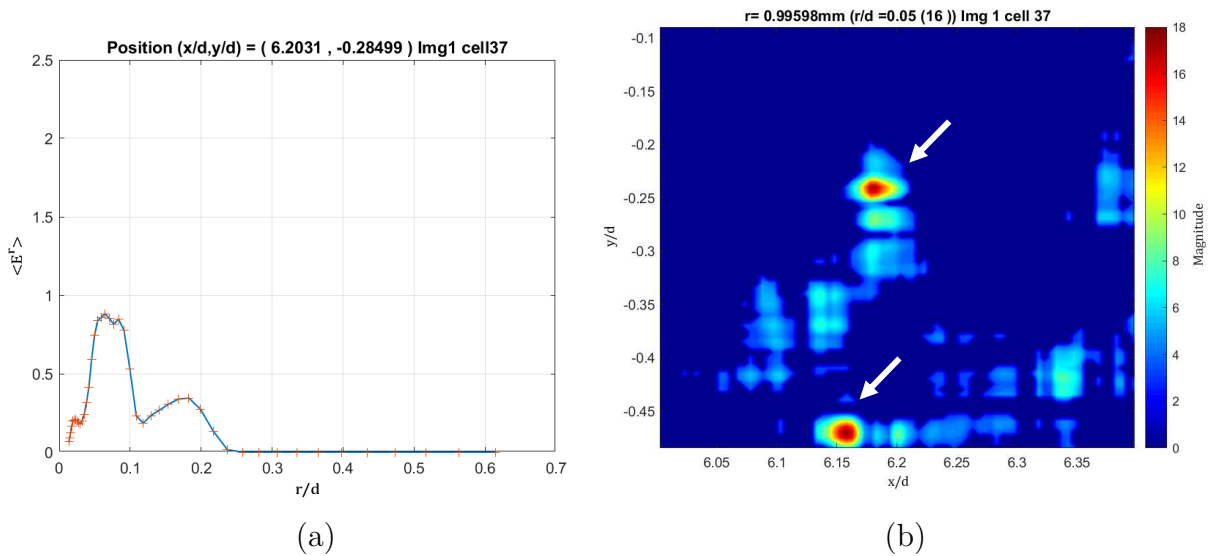


Figure 3.30(a)(b) - For caption see next page

3 Wavelet based code validation

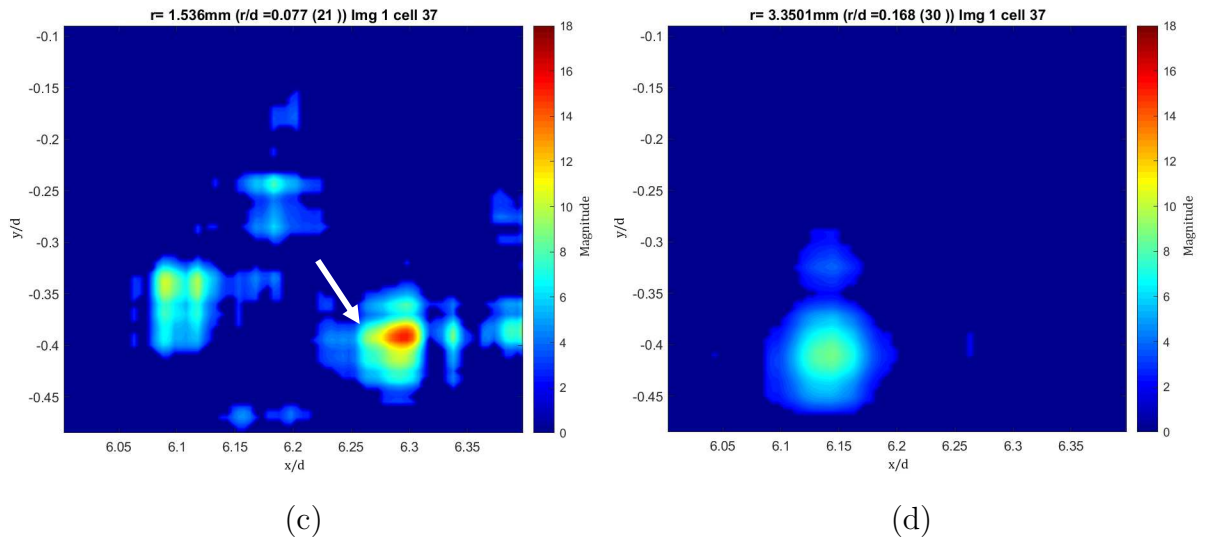


Figure 3.30 - (a) $E(r)$ plot which show two peaks and (b)(c)(d) wavelet maps at three scales near the peaks value of the $E(r)$ plot. The actual length scale is retrieved through the maps.

Three structures are visible, two for $r/d = 0.05$ depicted in Figure 3.30(b) and one for $r/d = 0.077$ reported in Figure 3.30(c) which are all indicated by arrows. The Figure 3.30(d) shows a big enlightened area which matches with the velocity fluctuations plot. The velocity fluctuations and the λ_2 value isolines are reported in Figure 3.31 for comparison.

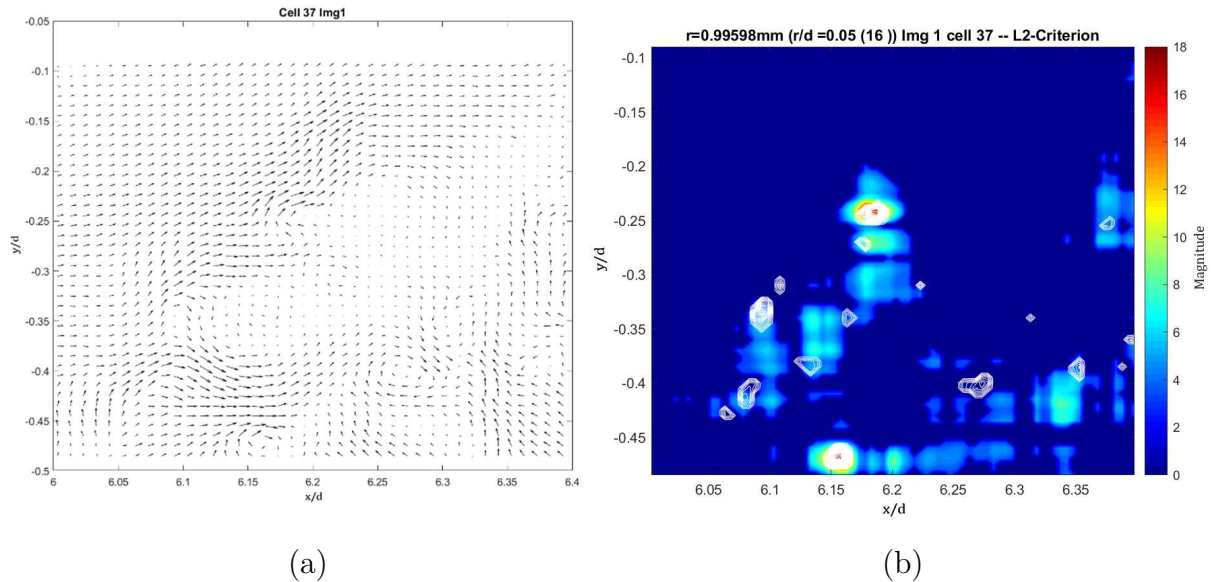


Figure 3.31 - (a) Velocity fluctuations and (b) isolines of λ_2 value superimposed to the wavelet map of cell 37 at the indicated scale.

Cell 77 ($x/d \simeq 5.4 - y/d = 0.5$)

The window considered is placed in the upper shear layer of the flow field at the beginning of the transitional region. As the windows examined previously, the $E(r)$ plot shows a peak at about $r/d \simeq 0.11$ (see Figure 3.32(a)). Thus, the wavelet map is reported in Figure 3.32(b) and it clearly shows the presence of one structure at $r/d \simeq 0.11$. This time the peak in $E(r)$ plot matches the right length scale value.

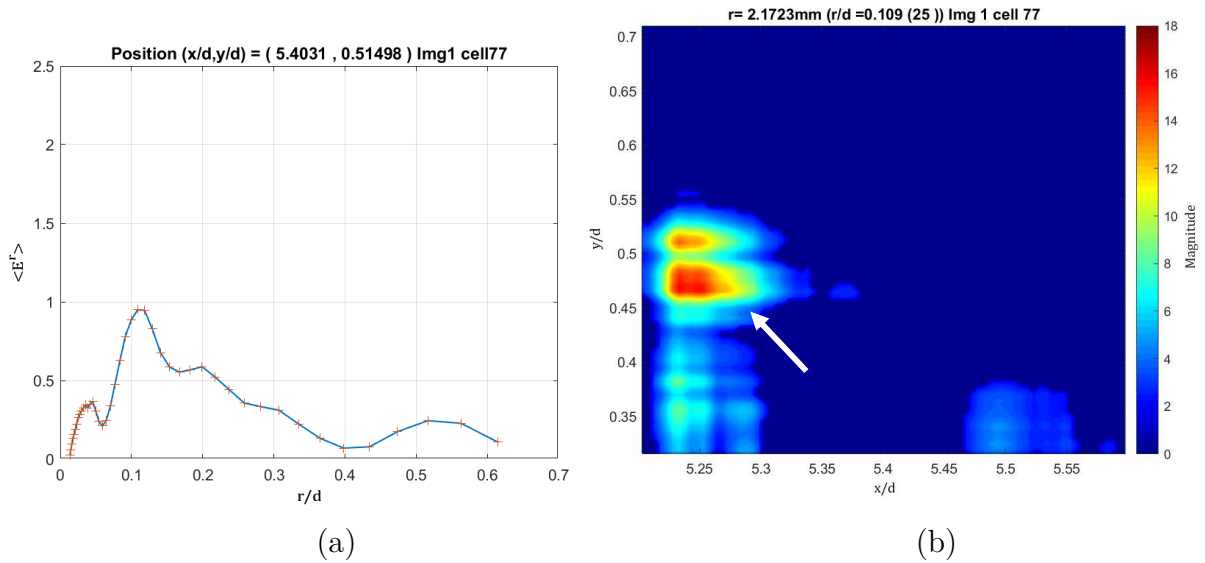


Figure 3.32 - (a) $E(r)$ plot which show a dominant peak for $r/D \simeq 0.11$ and (b) wavelet map for the same r/D value.

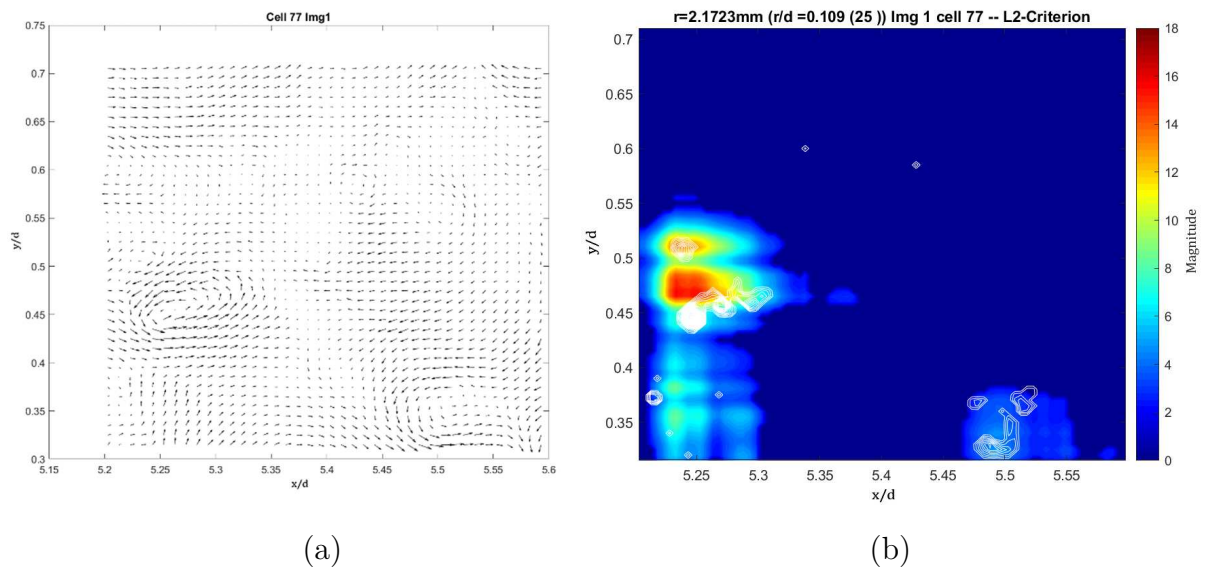


Figure 3.33 - (a) Velocity fluctuations and (b) isolines of λ_2 value superimposed to the wavelet map of cell 77 at the indicated scale.

The energetic area which is marked in Figure 3.32(b) with an arrow matches the presence of a swirling motion visible through the velocity fluctuations in Figure 3.33(a) and the λ_2 values depicted as isolines in Figure 3.33(b).

Above the marked vortex, a small energetic area is also visible so another small structure should be present which, although it is not clearly visible by means the velocity fluctuations. Conversely, the λ_2 isolines match with that small area and, moreover, in the lower-right side of Figure 3.33(b), the λ_2 -Criterion and the velocity fluctuations plot suggest the presence of another structure. Actually, the wavelet map also shows an energy concentration on the lower-right corner where the isolines are placed, but the energy level is lower than the energy of other structures. This fact finds an answer on the vorticity field map (see Figure 3.34) where the vorticity value of the arrow marked vortex is consistently higher than the value of the structure at the bottom right.

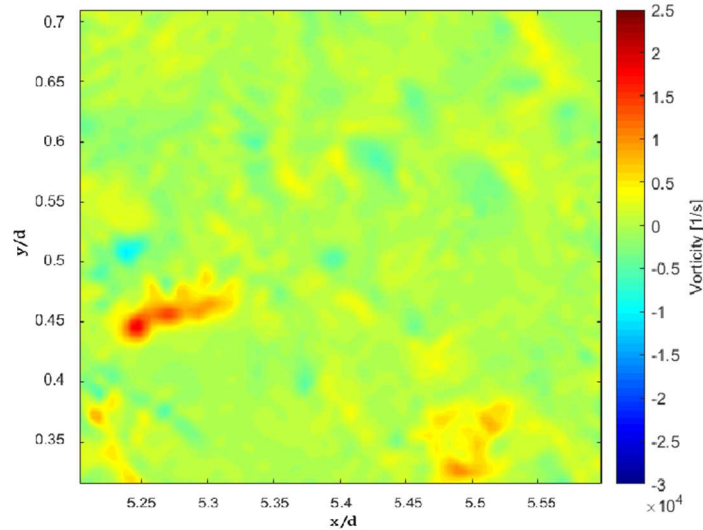


Figure 3.34 - Vorticity field of cell 77. It is evident the matching of high vorticity area with wavelet maps.

We can conclude that the code works properly, and it is capable to discern coherent structures and eddies, in a wider vision, at the proper length-scale for each structure. There are, of course some inaccuracies when the flow field becomes chaotic and fully turbulent, it nevertheless works well being able to spot small structure inside the chaotic motion as described for the transitional region of the jet flow.

At this point, we adopt the code in order to perform the analysis over a more sophisticated flow field that is the turbulent boundary layer. We focus our attention on the differences between a boundary layer over a smooth plate and over a riblet surface with the purpose to reveal some drag reduction characteristics of riblets widely observed in various industrial and practical applications.

4 Turbulent boundary layer over smooth and riblet surfaces

4.1 Boundary layer description

We consider a fluid flowing over a flat plate at null angle of attack with velocity U_0 . From the leading edge of the plate ($x = 0$), a thin layer arises better known as *boundary layer*, within which the viscous stress is no more negligible. Along the x-axis going downstream, the boundary layer evolves and its *thickness* $\delta(x)$ increases. The boundary layer thickness $\delta(x)$ is generally defined as the value of y at which the mean velocity $\langle U(x, y) \rangle$ reaches the 99% of the free stream velocity U_0 . There are more reliable quantities in order to characterize the boundary layer such as the *displacement thickness*:

$$\delta^*(x) = \int_0^\infty \left(1 - \frac{\langle U \rangle}{U_0}\right) dy \quad (4.1)$$

and the *momentum thickness*:

$$\theta(x) = \int_0^\infty \frac{\langle U \rangle}{U_0} \left(1 - \frac{\langle U \rangle}{U_0}\right) dy \quad (4.2)$$

The free stream pressure $p_0(x)$ is linked to the free stream velocity by the Bernoulli's equation

$$p_0(x) + \frac{1}{2}\rho U_0^2(x) = \text{constant} \quad (4.3)$$

so, the pressure gradient results to be:

$$-\frac{dp_0}{dx} = \rho U_0 \frac{dU_0}{dx} \quad (4.4)$$

According to equation (4.4), accelerating flow ($dU_0/dx > 0$) corresponds to a negative pressure gradient, or *favourable pressure gradient*. By contrast, decelerating flow ($dU_0/dx < 0$) corresponds to a positive pressure gradient, or *adverse pressure gradient*. The statement adverse is due to the tendency of separation of the boundary layer from the surface in a positive pressure gradient situation.

In a zero-pressure gradient boundary layer, i.e. over a flat plate, there is *laminar* flow from the leading edge and when a critical value of the Reynolds number is reached it evolves through a *transitional* process and become fully *turbulent* (see Figure 4.1).

There are many formulations of the Reynolds number definition based on different characteristic quantities of the boundary layer, i.e. the displacement and the momentum thickness, and, among them, one formulation is based on the stream-wise direction x as follow:

$$Re_x = \frac{U_0 x}{\nu} \quad (4.5)$$

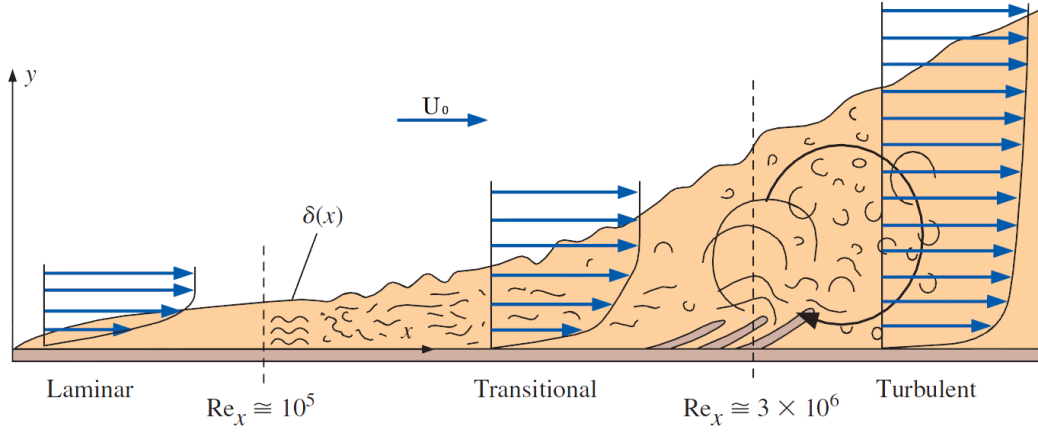


Figure 4.1 - Structure of boundary layer over flat plate at null angle of attack.

The *critical* Re_x which separates the laminar and transitional regime is approximately $Re_{crit} = 5 \cdot 10^5$. The critical value of Re_x depends considerably on the level of disturbances in the free stream.

As can be seen by Figure 4.2, the mean velocity profile for a turbulent boundary layer is fuller than the laminar counterpart and rises much more steeply from the wall than the laminar profile does. Since the wall shear stress is defined to be:

$$\tau_w = \rho\nu \left(\frac{d\langle U \rangle}{dy} \right)_{y=0} \quad (4.6)$$

it is clear the turbulent boundary layer has a higher value of wall shear stress than laminar boundary layer.

The total shear stress $\tau(y)$ is the sum of the viscous shear stress τ_ν and the Reynolds stress τ_{Re} :

$$\tau(y) = \tau_\nu + \tau_{Re} = \rho\nu \left(\frac{d\langle U \rangle}{dy} \right) - \rho\langle uv \rangle \quad (4.7)$$

Close to the wall, the viscous shear stress dominates while the Reynolds stresses are negligible and become zero at the wall, since the boundary condition at the wall is $\mathbf{U}(\mathbf{x}, t) = 0$. Profiles of viscous and Reynolds shear stresses are reported in Figure

4.2. Therefore, it is evident that, close to the wall the dominant parameters are the cinematic viscosity ν and the wall shear stress τ_w . Thus, in the near wall-region we define *viscous scales* for velocity and length scales. These are the *friction velocity* u_τ and the *viscous length* l_τ defined as follow

$$u_\tau = \sqrt{\frac{\tau_w}{\rho}} \qquad l_\tau = \frac{\nu}{u_\tau} \qquad (4.8)$$

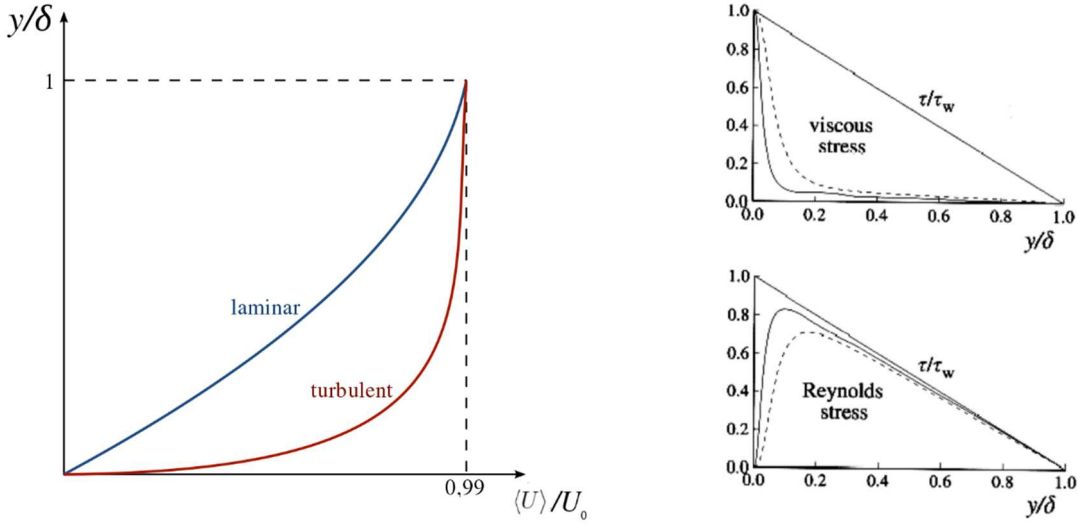


Figure 4.2 - Mean velocity profiles and stresses of laminar and turbulent boundary layer.

The distance from wall can be measured in viscous length, or *wall units* called y^+ and, similarly, the velocity can be related to the friction velocity as

$$y^+ = \frac{y}{l_\tau} \qquad u^+ = \frac{\langle U \rangle}{u_\tau} \qquad (4.9)$$

Since the important role played by viscosity in the near-wall zone, in 1925 Prandtl postulated that, at high Reynolds number, in the region $y/\delta \ll 1$ close to the wall, an *inner layer* exist within the mean velocity profile is determined by the viscous scales and results independent of the outer quantities δ and U_0 .

The mean velocity profile obeys different laws according to the wall distance. In the closest part to the wall, the velocity is described by the linear law

$$u^+ = y^+ \qquad (4.10)$$

and the layer is known as *viscous sublayer* which extends from the wall to approximately, $y^+ = 5$. For $y^+ < 1000$ the mean velocity profile follows a logarithmic law (due to von Kármán) and the layer is named *log law region*:

$$u^+ = \frac{1}{k} \ln y^+ + B \quad (4.11)$$

where $k = 0.41$ is the *von Kármán constant* and $B = 5.2$. The region between the viscous sublayer and the log law region is a transition layer between the viscosity-dominated and the turbulence-dominated regions and it is called *buffer layer* and it is placed approximately at $5 < y^+ < 30$. The Figure 4.3 shows the structure and the mean velocity profile of the inner layer.

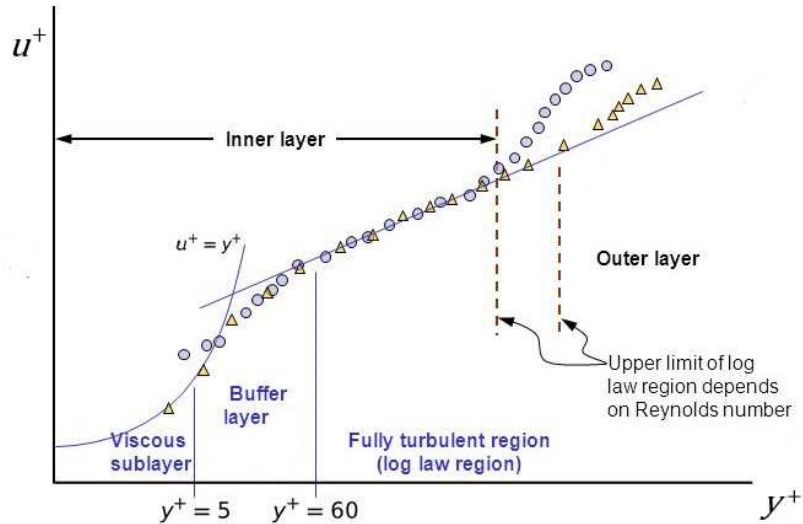


Figure 4.3 - Turbulent boundary layer's structure

4.2 Coherent motion in turbulent boundary layer

Turbulent structures within wall flows are identified by flow visualization or other education methodologies, but they result to be difficult to define precisely. There are many structures some of which present a recurrent and characteristic coherent pattern. Kline and Robinson provided a categorization of quasi-coherent structures and some of them are:

- Low-speed *streaks* in the region $0 < y^+ < 10$.
- *Ejection* of low-speed fluid outward from the wall.
- *Sweeps* of high-speed fluid toward the wall.
- *Large-scale motions* (LSM) in the outer layer including *bulges*, *superlayer* and *deep valleys* of free-stream fluid.
- Several proposed forms of *vortical structures*.

In the near wall region for $y^+ < 40$, numerous flow visualization experiments have revealed *streaks*. The streaks correspond to relatively slow-moving fluid while the fluid between the streaks is relatively fast. In Figure 4.4, two successive layers

of the flow over a flat plate in a water channel at $y^+ = 2.7$ and $y^+ = 38$ show the presence of streaks in the streamwise direction (x) which are revealed by the accumulation of tiny hydrogen bubbles generated periodically by means a fine wire placed across the flow in the spanwise direction (z) which acts as an electrode.

With the increasing streamwise distance, the streak slowly moves upward until it is rapidly lifted away from the wall by the wall-normal fluctuations, a process known as *ejection* and then the streak exhibits a rapid oscillation followed by a breakdown into finer scale motions [6]. In order to guarantee continuity, regions of high-speed fluid move toward the wall and these events are called *sweeps*. The Figure 4.5 shows the evolution process of a streak and the $u - v$ plane, representing respectively the streamwise and wall-normal components of fluctuating velocities, in which ejections and sweeps are identified.

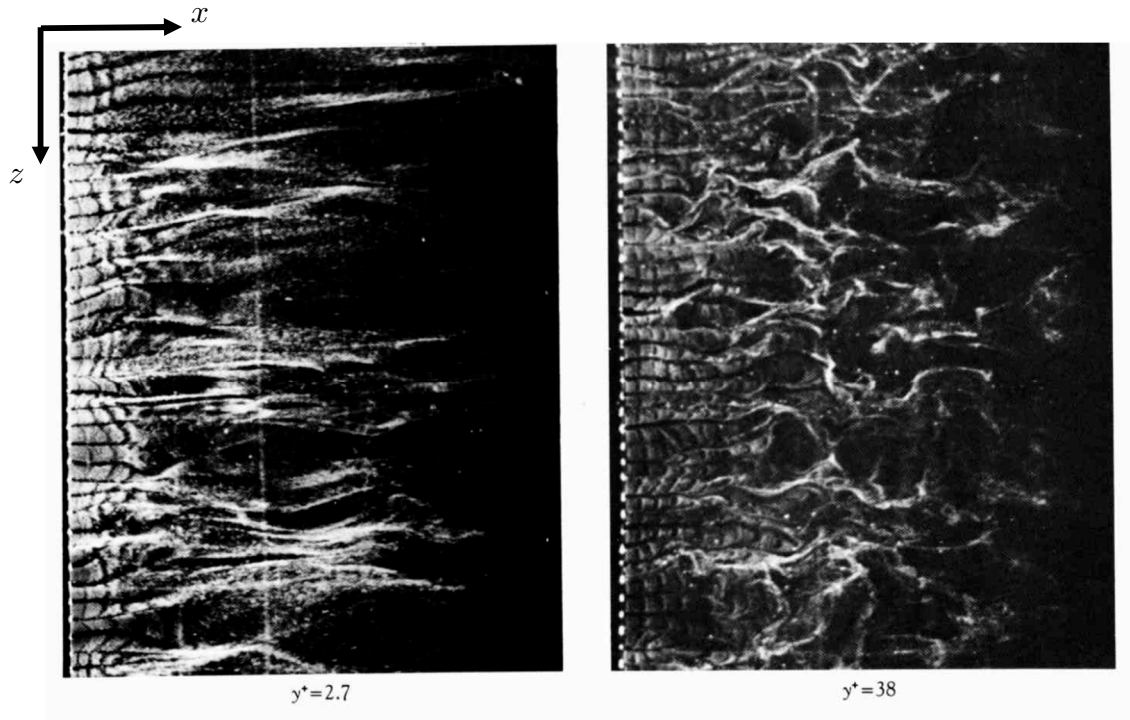


Figure 4.4 - Successive layers of the flow near a flat plate in a water channel in a streamwise-spanwise plane. The visible streaks are generated by the accumulation of tiny hydrogen bubbles released periodically from a thin platinum wire visible on the left (Van Dyke [2]).

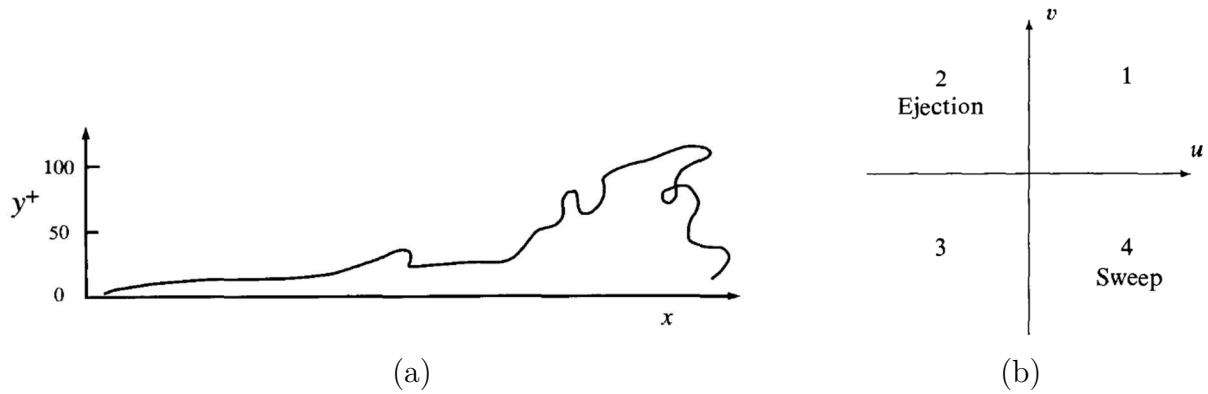
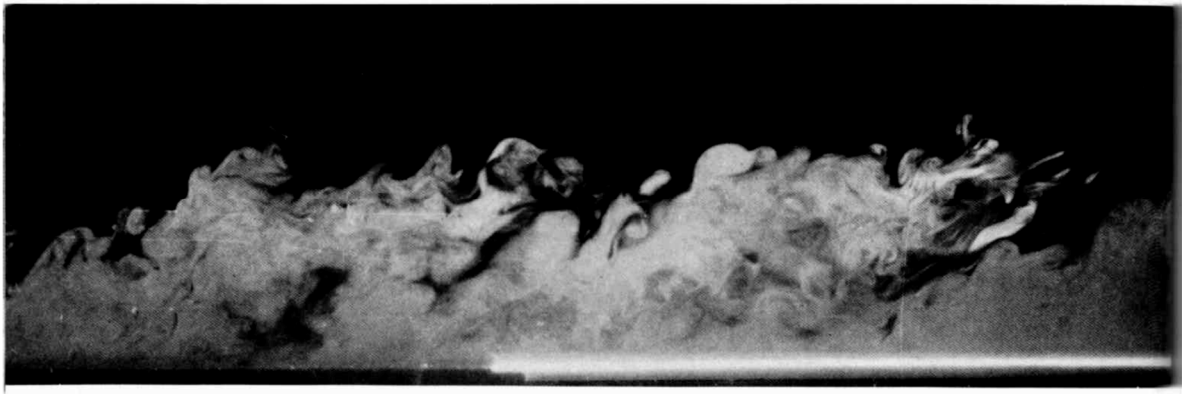


Figure 4.5 - (a) A streak in a turbulent boundary layer showing the ejection of low-speed near-wall fluid. (b) The $u - v$ sample plane showing the four quadrants and the quadrants corresponding to ejections and sweeps (Pope [6]).

In the outer part of the boundary layer there is a thin turbulence front, called *viscous superlayer*, separating the turbulent fluid of the boundary layer from the free-stream fluid. There, one can see the *large-scale motions* (LSM) or *turbulent bulges* having length of order δ to 3δ . These large-scale eddies or bulges are inclined at a characteristic angle of $20-25^\circ$ and they are separated by *valleys* of non-turbulent fluid which penetrate the boundary layer. In Figure 4.6, a typical structure of large-scale motions is depicted remarking the characteristic features.



(a)

Figure 4.6(a) - For caption see next page

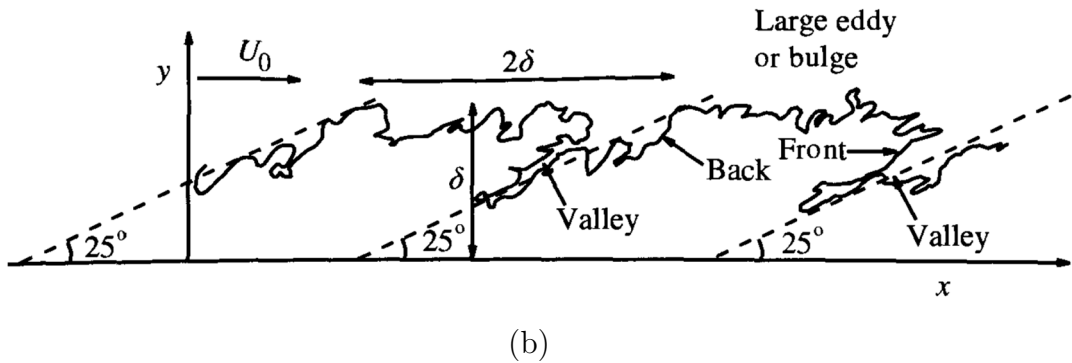


Figure 4.6 - (a) Fog of tiny oil droplets introduced in a turbulent boundary layer with Reynolds number based on momentum thickness is about $Re_\theta = 4000$ (Van Dyke [2]). (b) Large-scale features of turbulent boundary layer at $Re_\theta = 4000$ (Pope [6]). Both images are retrieved from the experiment of Falco in 1977.

The large eddies and the superlayer also contain finer-scale structures that Falco called *typical eddies* (see Figure 4.7) which later were identified to be *hairpin* or *horseshoe vortices* inclined at 45° .



Figure 4.7 - Oil fog illuminated by a sheet of laser light shows a portion of a turbulent boundary layer. The vortex-ring indicated with an arrow is an example of what Falco called “typical eddy”.

The hairpin vortices spanwise dimensions scale with viscous length l_τ while in the streamwise direction they can be considerably elongated with an overall length of order δ . Indeed, the part of filament moving away from the wall (known as *head* of the hairpin vortex) experiences higher mean flow velocity and therefore will be advected downstream faster than the lower part. Thus, the “legs” of the hairpin vortex will be stretched and, consequently, intensified. A sketch of a conceptual hairpin vortex is shown in Figure 4.8a. Moreover, many studies have reported that hairpin or horseshoe vortices occur in streamwise sequence with increasing size

downstream and that they often occur in *packets* as sketched in Figure 4.8b. Larger structures may be composed by packets of hairpin vortices.

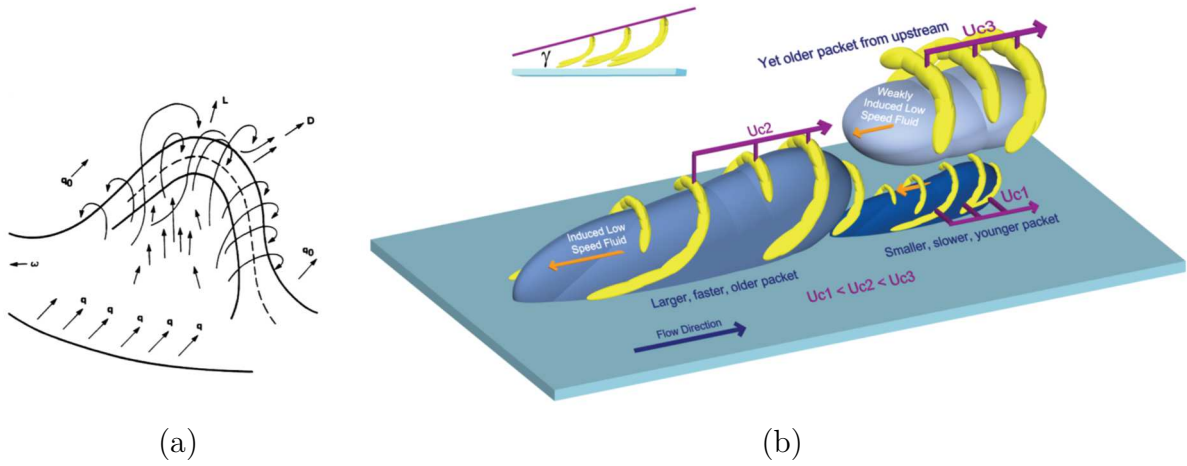


Figure 4.8 - (a) Theodorsen's depiction of a horseshoe vortex and (b) Conceptual scenario of growing hairpin packets (Ref. [9]).

4.3 Drag Reduction technologies

Since the beginning of the technological development, humans have been inspired by nature and animals in the attempt to transfer what the nature has refined during millions of years of evolution into his own technological application. These biologically inspired designs are called *biomimetics* which means mimicking biology or nature.

Observation of sharks and, specifically, their ability to move so fast took someone to wonder which could be their secret. They can reach up to $15 - 20 \text{ m/s}$, so why they can swim so fast? Scientists focused their attention onto the particular morphology of shark skin. They found that the shark skin is a non-smooth surface. On their skin surface, there are many micro-scales called dermal denticles which form a kind of riblet surface (see Figure 4.9). This riblet surface is able to reduce the shear stress which leads to a faster motion of the water over shark skin. Skin friction accounts for a great portion of the total drag. Friction, or viscous friction, is caused by the interaction between two layers of the same fluid flowing at different speed generating the shear layer, or between the fluid flowing over a surface and the surface itself. Indeed, the viscous drag is a measure the momentum transfer between the body moving within a flow field and the fluid.

Riblets is one of many drag reduction technologies which is studied and adopted for industrial purposes or marine navigation and so more.

Figure 4.10 shows different types of marine drag reduction techniques some of which can be implemented for non-marine purpose too. Three main types of drag reduction techniques exist: *active*, *passive* and *composite drag reduction* [10] which are rapidly presented below.

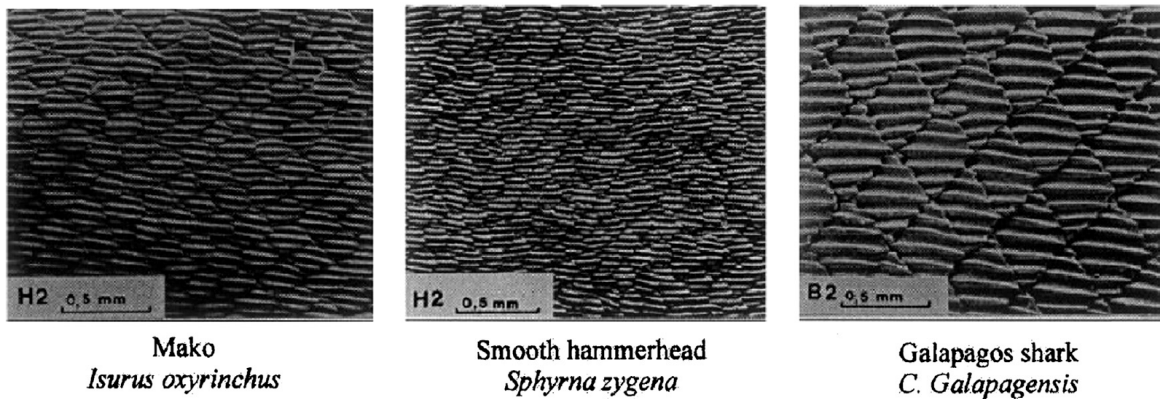


Figure 4.9 - Detail of fast sharks' skin (Ref. [10]).

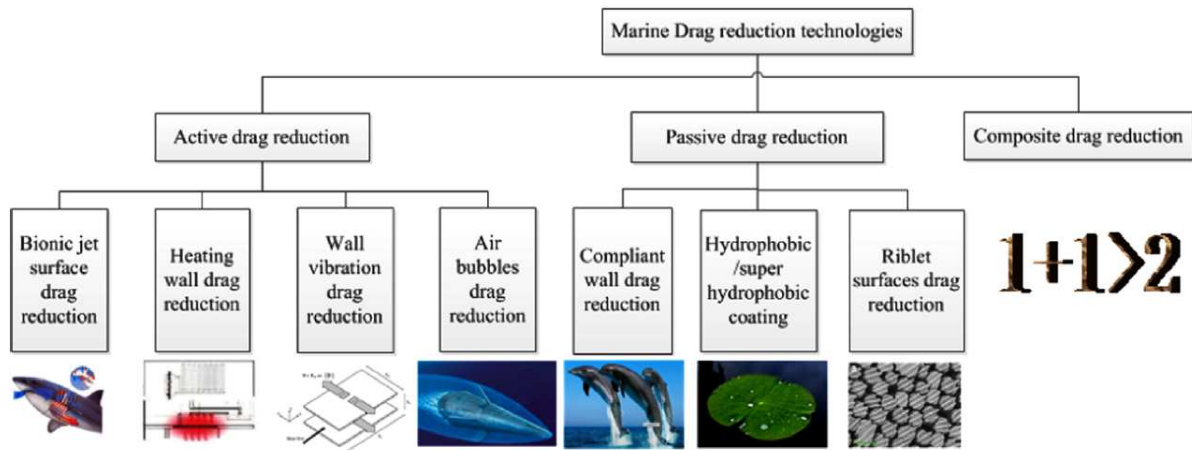


Figure 4.10 - Different drag reduction technologies (Ref. [10])

Bionic jet surface drag reduction

When sharks swim, they inhale water through their half-opened mouth, and it is successively discharged flowing through the gills for gas exchange. The water jet discharged by gills helps to increase the viscous sublayer thickness resulting in a decreased skin friction.

Heating wall drag reduction

In heated wall flows, the turbulent kinetic energy decreases in the buffer layer, resulting in a decreased Reynolds shear stresses and, hence, in a less turbulent production. Moreover, the lower fluid viscosity near the wall contributes to skin friction decrease. The overall contribution of Reynolds shear stress and skin friction decrease results in drag reduction.

Wall vibration drag reduction

The reduction of turbulence intensity caused by disruption of the interaction between the quasi-streamwise vortices and the low velocity streaks results in drag reduction and can be achieved through wall vibrations.

Air bubble drag reduction

More viscous fluids have higher drag than less viscous fluid. Thus, in water flows drag reduction can be achieved injecting a thin layer of air between the water and the body surface. This thin layer can be composed by small air bubbles or air film. A video documentation of swimming penguins shows that penguins exhale air before emerging at high speed from the sea and that exhaled air sometimes agglomerates

in rings surrounding the body of the penguins and remain there for several seconds [11].

Air bubble or film drag reduction technique was adopted in underwater missiles and torpedo.

Compliant wall drag reduction

The first experimental studies were carried by Kramer, which argued the possibility that compliant wall, such as dolphins' skin, can delay transition from laminar to turbulent regime stabilizing the boundary layer. Coupling between the flow dynamics and wall dynamics have an effect on drag reduction. However, when the compliant surface hardens, it will lose its drag reduction performance.

Hydrophobic coating

One of the most studied hydrophobic surfaces is the lotus leaf which presents a super-hydrophobic behaviour. Hydrophobic and super-hydrophobic surfaces lead to a slip condition in the near wall area, instead of the typical no-slip condition. This results on a reduced drag. Moreover, this characteristic contributes to keep the surface clean and free from any kind of dirt particles.

Composite drag reduction

This kind of drag reduction technique employs two different passive or active techniques simultaneously. It's been observed that the results of combined methods, such as polymer additives and riblets, work better than the algebraic sum of both effects [11].

4.4 Drag reduction by riblet surfaces

Turbulent flows over a smooth surface, like a flat plate, exhibit strong velocity deviation from the mean velocity direction. The strong exchange of momentum in a turbulent boundary layer is due to characteristic motions carrying high-speed fluid from higher layer to the near-wall zone (*sweeps*) and low-speed fluid away from the surface (*ejection*) into high speed regions of the flow. These two types of local events require fluid motion in the spanwise direction. Thus, hampering this spanwise motion the momentum exchange will be reduced, hence, the wall shear stress decreases. Riblets aligned with flow streamwise direction acts as barriers for z-direction velocity w .

Riblets with height of about $y^+ \simeq 3.5$ are included in the viscous sublayer, so the flow around the riblets can be analysed with the viscous theory, since fluid within this layer act as a viscous fluid. Under viscous condition, it results that the ribbed surface appears as a smooth surface located at a virtual origin (see Figure 4.11). However, the virtual origin depends on the flow direction. Indeed, for a fluid flowing streamwise, so parallel to riblets and grooves the virtual origin h_L turns out to be lower than the virtual origin h_C for a crossflow motion. This difference in height for virtual origins $\Delta h = h_L - h_C$ plays an important role, because an increased Δh turns out in higher resistance if the flow placed at a fixed y^+ moves laterally than if it moves in the longitudinal direction. Thus, the crossflow is hampered by the riblets and momentum transfer and shear stress decrease.

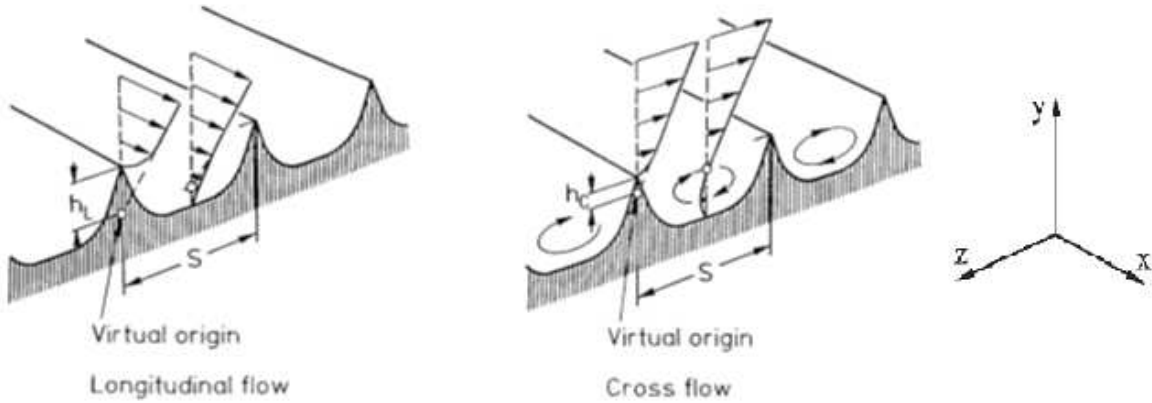


Figure 4.11 - Longitudinal and crossflow on riblets surface with different virtual origin height (Ref. [11]).

Another effect which contributes to drag reduction is due to the reduced area exposed to high velocity vortices. By keeping the vortices above the riblet tips the crossflow velocity fluctuation interact only with a reduced part of the entire surface [12], as showed in Figure 4.12, for two value of s , where s is defined to be the distance between two successive tips. The numerical results obtained by Choi *et al.* [12] are reported in Figure 4.13 which shows how the higher value of wall shear stress are obtained mainly over the riblet tips while the grooves exhibit relatively lower values.

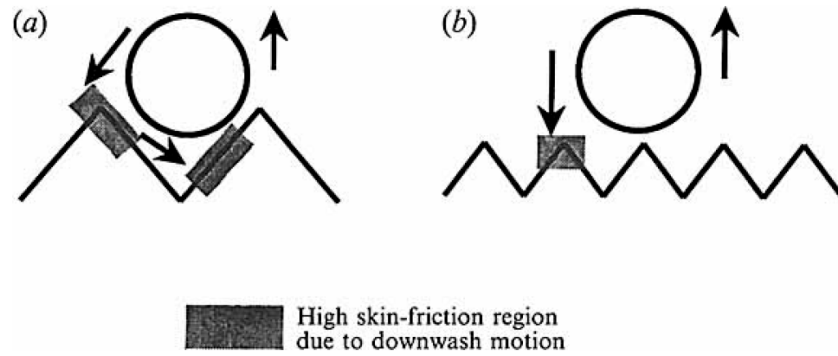


Figure 4.12 - Schematic sketch of drag increase and reduction by riblets due to exposed area. (a) $s^+ \simeq 40$ shows an increase of drag due to extensive area exposed to downwash motion; (b) $s^+ \simeq 20$ shows a drag reduction due to limited area affected by downwash motion (Ref. [12]).

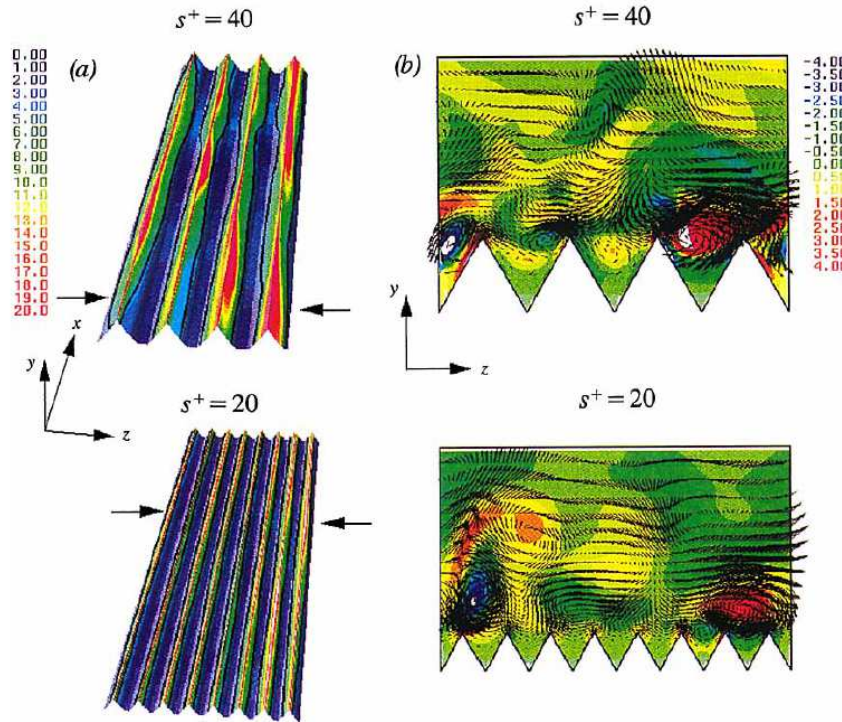


Figure 4.13 - Instantaneous flows over the riblets with $\alpha = 60^\circ$; (a) contours of the wall shear stress rate on the riblet surfaces; (b) crossflow velocity vectors v and w and contours of the streamwise vorticity (Ref. [12]).

In order to evaluate drag reduction performances of different shapes of riblets with different spacing value, all length dimensions are scaled by the *viscous length* $l_\tau = \nu/u_\tau$ where ν is the kinematic viscosity and u_τ is the *friction velocity*. The resulting quantities have the structure of a Reynolds number as can be seen from equation (4.12).

$$s^+ = \frac{su_\tau}{\nu} \qquad h^+ = \frac{hu_\tau}{\nu} \qquad (4.12)$$

For an optimization of shear stress reduction, more than one geometry of riblets was tested. To quantify the real performance of riblets, a comparison with a smooth reference surface is made. Thus, $\Delta\tau$ is the difference between shear stress τ on the ribbed surface and τ_0 on the smooth reference surface ($\Delta\tau = \tau - \tau_0$). So, negative values of $\Delta\tau/\tau_0$ turns out into drag reduction while positive values refer to an increase of drag. Some results obtained by Bechert *et al* [11] are reported in Figure 4.14.

The optimum value of drag reduction is obtained for the very thin blade-like ribs, which presents the maximum height difference Δh , as suggested by theory. The achieved shear stress reduction is around 9.9%. Bechert, through this oil channel's experiment, has showed that the optimum height of thin blade riblets was around $h = 0.5s$. Of course, it results difficult to manufacture this type of riblets and, moreover, in technical applications, like aircraft, these ribs are too weak to face dirt and particles impacts.

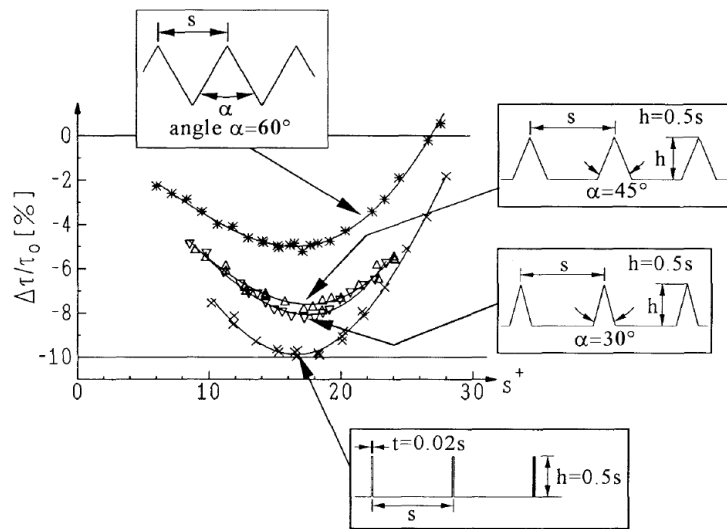


Figure 4.14 - Drag reduction performance of various riblet geometries (Ref. [11]).

Other riblet configurations were examined by Bechert *et al.* [11] like “brother and sister riblets”, where between two ribs one small rib is inserted (see Figure 4.15). This geometry came out by the observation of two ribs being way too far from each other, i.e. s is too high, the drag reduction performances drastically fall down, probably because of increased sloshing of the fluid in the grooves which, in this way, enhances momentum transfer and, as a consequence, increased wall shear stress occurs. Thus, they thought to place another small rib in the grooves. This riblet configuration took drag reduction performance results comparable with blade ribs.

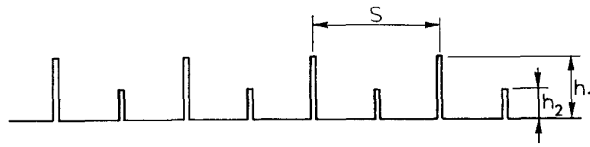


Figure 4.15 - “Brother and sister riblets” configuration (Ref. [11]).

Observation of shark skin and ideas similar to the “brother and sister riblets” led Bechert *et al* to investigate two more configurations: the 3D riblets and the shark skin riblets replica.

The former consisted in blade riblets of finite length as displayed in Figure 4.16. The various experiments performed with different riblet heights showed a wall shear stress reduction of about 7.3%, slightly below the 9.9% of the continuous blade riblets.

The shark skin replica was tested to discover if other mechanism plays a role in the drag reduction process. They reproduced the single skin element of sharks, which was placed on top of a spring to simulate the non-rigid body of the shark (see Figure 4.17). The wall shear stress reduction was found to be around 3% when scales are aligned each other. Of course, there can be many unknown factors which can help shear stress reduction for sharks, and moreover, usually the water flow can be not perfect aligned with the shark skin scales.

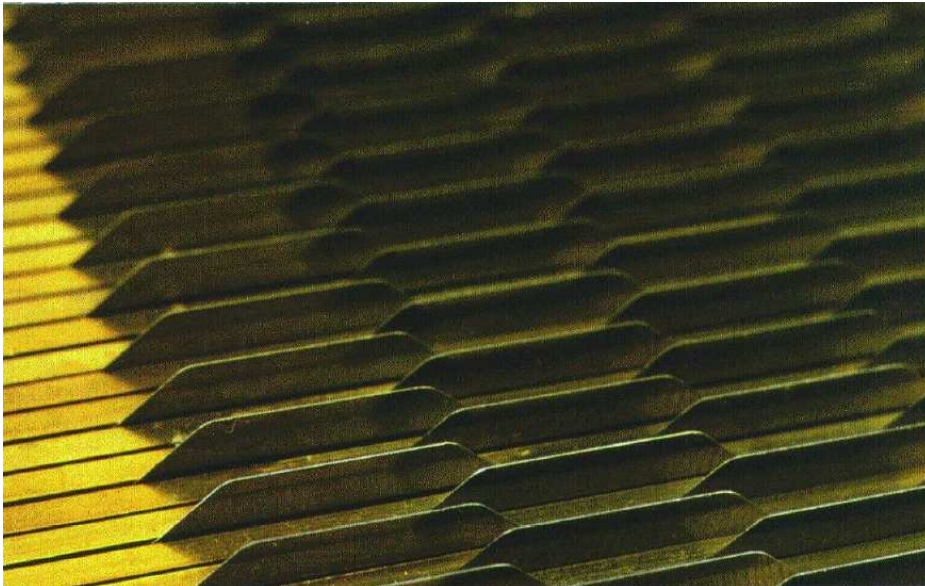


Figure 4.16 - Test surface with three-dimensional riblets (Ref. [11]).

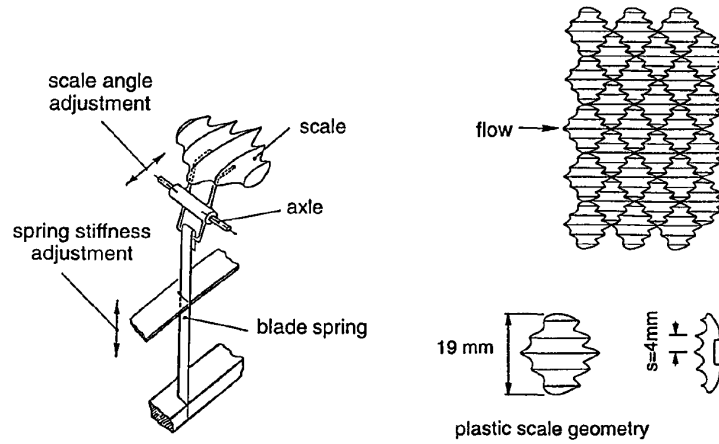


Figure 4.17 - Schematic of the artificial shark scale replica with the suspension mechanism (Ref. [11]).

Since the dependence of drag reduction performances, besides the spacing s , by the geometry of riblets, Mayoral and Jimenez [13] suggested a new geometric parameter which could capture at the same time the influence of both the spacing and shape of ribs on drag reduction performances. The better results were obtained considering the cross section of the groove A_g defining the parameter

$$l_g^+ = \sqrt{A_g^+} \quad (4.13)$$

As Figure 4.18 shows, the optimum values of s^+ and h^+ have variations of the order of 40%, while the optimum l_g^+ varies by approximately 10%. Moreover, it can be seen a better collapse of the data over a limited area for l_g^+ with respect to the data for s^+ where drag reduction is defined $DR = -\Delta\tau/\tau_0$.

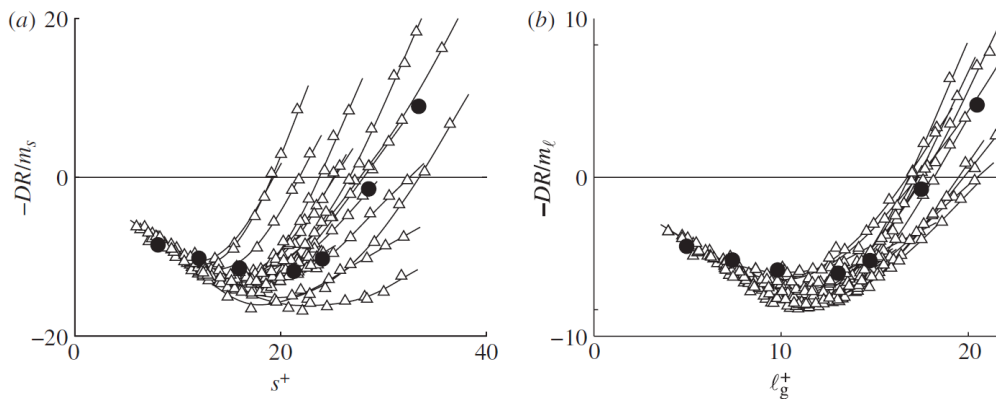


Figure 4.18 - Drag reduction curves of diverse riblets, reduced to a common viscous slope m . Drag Reduction DR (a) as function of s^+ and (b) as function of l_g^+ (Ref. [13]).

The drag reduction plots appear to be all similar, so a typical curve of drag reduction as function of s^+ is depicted in Figure 4.19, in which different drag

regimes are discernible according to the s^+ values. The first regime is known as *viscous regime* which extends from $s^+ = 0$ to approximately $s^+ \simeq 10$, and within it, the contributions of non-linear terms to the flow in the near-wall zone inside the riblet's grooves are negligible and drag reduction DR is proportional to s^+ . The slope can be quantified as:

$$m_s = - \left. \frac{\partial(\Delta\tau/\tau_0)}{\partial s^+} \right|_{s^+=0} \quad (4.14)$$

Then, once the optimum value s_{opt}^+ is reached, the viscous regime *breakdown* occurs, and the reduction become a drag increase instead.

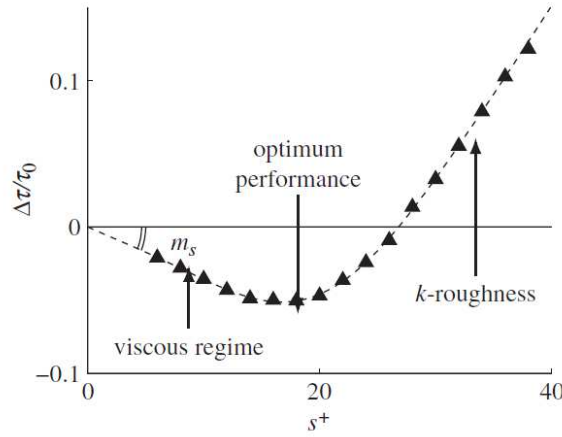


Figure 4.19 - Drag reduction regimes observed over triangular riblets with 60° tip angle, as a function of s^+ (Ref. [13]).

The analytic estimation of the drag reduction by riblet surfaces can be made looking at many studies which pointed out that when drag reduction occurs the mean velocity profile rises with respect to mean velocity profile of boundary layer over a smooth surface due to an increased thickness of the viscous sublayer which leads to an upward displacement of the logarithmic region, as suggested by Choi [14] (see Figure 4.20).

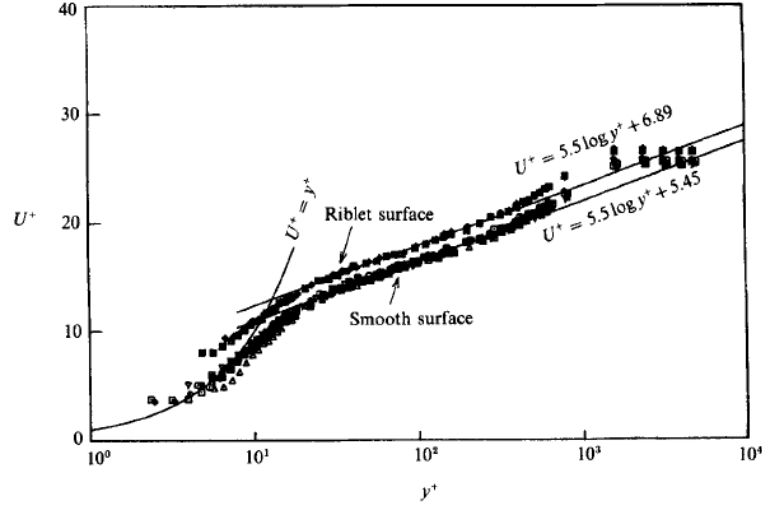


Figure 4.20 - Semi-logarithmic plot of mean velocity profiles over smooth and riblet surfaces (Ref. [14]).

The *log law* at the top of the turbulent boundary layer can be expressed as:

$$U_{\delta}^{+} = \frac{1}{k} \ln \delta^{+} + B \quad (4.15)$$

where U_{δ}^{+} can be written as

$$U_{\delta}^{+} = \frac{U_{\delta}}{u_{\tau}} = \left(\frac{2}{c_f} \right)^{1/2} \quad (4.16)$$

with c_f being the friction coefficient, U_{δ} the velocity at the edge of boundary layer, k the von Kármán constant and B a constant. The effect of a given riblet surface would be to change the B value which can be estimated through the relation

$$\Delta B = \mu_0 \Delta h^{+} \quad (4.17)$$

because of the linearity of the viscous regime, so considering ΔB proportional to the protrusion height Δh^{+} with a universal coefficient μ_0 . So, the drag reduction estimation can be obtained by the equation

$$\frac{\Delta c_f}{c_{f0}} = \frac{\Delta \tau}{\tau_0} = \frac{\Delta B}{(2c_{f0})^{-1/2} + (2k)^{-1}} \quad (4.18)$$

To conclude the overview, sinusoidal riblets are rapidly presented. We previously mentioned the enhanced effect of composite drag reduction technique. So, the combination of longitudinal riblets and wall-oscillation technique can have great results in terms of drag reduction performances, but it could struggle to find a practical application due to technological complication. Therefore, the oscillation of the flow

can be forced by sinusoids of riblets which mimic the oscillation behaviour with a specific path given by

$$z = a \sin\left(\frac{2\pi}{\lambda} x\right) \quad (4.19)$$

where time t has been replaced by the streamwise coordinate x , a represent the amplitude, λ the wavelength and z the spanwise coordinate [15].

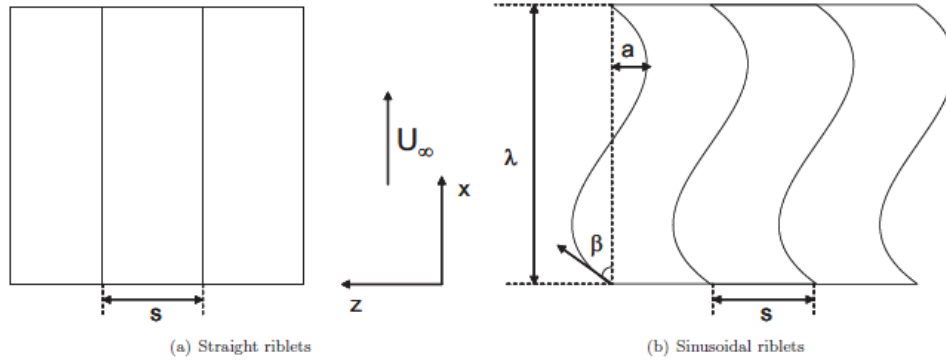


Figure 4.21 - Comparison between straight and sinusoidal riblets from a top view (from Ref. [16]).

4.5 Technological applications of riblets

In previous years, both Airbus and Boeing had carried out riblet film tests on full-size aircraft. Airbus started with an A320 aircraft covered with riblet film and obtained the expected results. Later, a long range A340-300 partly covered with 3M-type (see Figure 4.22) riblets was flown for several years in commercial service by Cathay Pacific Airways. Nowadays, riblets are not implemented in long range aircraft for few reasons concerning maintenance operations and riblets degradation. Bechert and Hage [17] considered a hypothetical application of riblet film on a long range A340-300. Considering that the contribution of skin friction to the total drag of this aircraft is about 50%, the implementation of riblets with trapezoidal grooves, taking into account possible imperfections, leads to a skin friction reduction of about 6%. Clearly, the entire surface of the aircraft cannot be covered by riblets, for example windows and leading edges of wing where riblets can interfere with de-icing system. So, only 70% of the surface of the aircraft can be coated with riblet film. The resulting reduction of aircraft total drag can probably achieve 2% which turn out in a 2% reduction of fuel consumption with a related 1.6 tons additional payload which substitute the saved fuel. Clearly, this leads to a profit increase for airline companies.

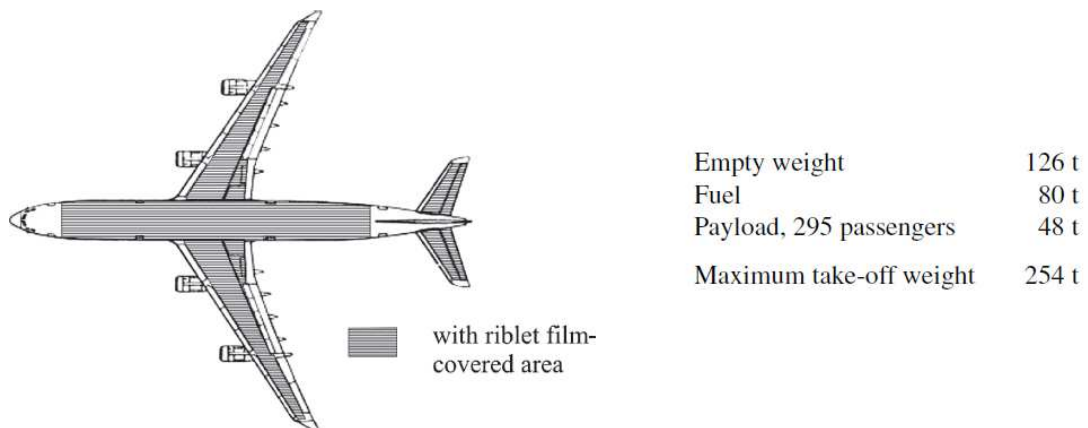


Figure 4.22 - Long range commercial aircraft A340-300 (Cathay Pacific Airways) partly covered with riblet film. The film was not applied under the wing and on the lower half of the fuselage (Ref. [17]).

Another interesting application of riblets is within gas pipelines. The pressure loss in pipelines is caused by wall friction alone. However, it would be difficult to apply plastic riblet film inside the pipe. Thus, Marvin Weiss had the idea that longitudinal scratching inside on the inside part of the pipeline tube can in some way like non-efficient riblets. These scratches are produced by means steel wire brushes which are moved along the pipeline which simultaneously perform cleaning of the surface from various roughness caused by corrosion and welding connections. This combined effect was tested on a ten miles piece of operating gas pipeline confirming a 10% of pressure loss reduction [11].

Other applications of riblets are found in sports. The most famous application of riblet surface in sport is sharkskin swimming suit. The sharkskin suit became popular in Olympics Games and swimming competition, when in 2010 they were banned from competitions as significantly improving performance.

5 Wavelet analysis of turbulent boundary layer

5.1 Experimental set-up and PIV measurements

The experimental activity was carried out within the laboratory of aerodynamics of Politecnico di Torino by means an open circuit wind tunnel depicted in Figure 5.2. The test section has a longitudinal length of 4 m and a cross section of 0.7x0.5 m. At the test section's centre there is a square opening where the 25x25x1 cm examined plates were placed. In order to force the transition of the flow from laminar to turbulent and enhance the boundary layer thickness some strips were added upstream the plate.

Above the test section the laser is placed (see Figure 5.3) which through a system of lenses generates a thin laser sheet in the streamwise and wall-normal plane, i.e. the $x - y$ plane. The laser has a wavelength of $\lambda = 532 \text{ nm}$ and it flashes at 15 Hz with a maximum energy of 200 mJ. Due to the low flashing frequency this Low Speed Laser is not suitable for time history acquisition.

The measurements of turbulent boundary layer were carried out for a smooth plate and for three types of riblet surfaces. The geometry scheme of the three riblets types are sketched Figure 5.1 and the related geometry data are reported within Table 5.1. Data concerning PIV images are reported within Table 5.2, Table 5.3 and Table 5.4 for each Reynolds number examined.

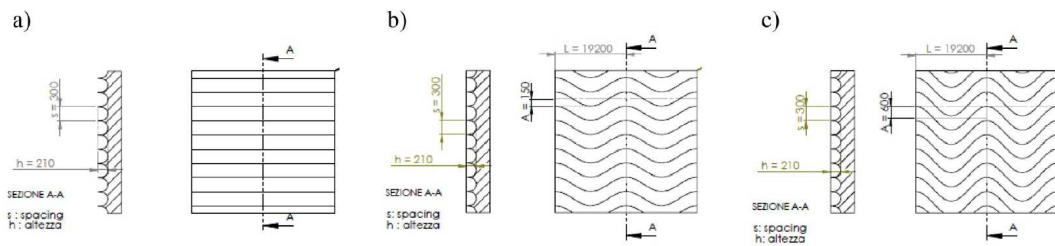


Figure 5.1 - Schematic of riblets' geometry; (a) Longitudinal riblets (R_Long); (b) Sinusoidal 1 (R_S1); (c) Sinusoidal 2 (R_S2).

	s (μm)	h (μm)	Amplitude (mm)	Wavelength (mm)
R_Long	300	210	-	-
R_S1	300	210	0.15	19.2
R_S2	300	210	0.6	19.2

Table 5.1 - Geometry data of riblet surfaces.

5 Wavelet analysis of turbulent boundary layer

$Re_\theta = 2790$	Pixel/mm	N° of samples per image	Field size	$\Delta x \Delta y$ (mm)
Smooth	80	833x893	$4 \leq x^+ \leq 820$ $4 \leq y^+ \leq 765$	0.025
R Long	80	828x893	$4 \leq x^+ \leq 820$ $4 \leq y^+ \leq 760$	0.025
RS1	92.4	468x632	$4 \leq x^+ \leq 1000$ $7 \leq y^+ \leq 750$	0.0433
RS2	80	805x893	$4 \leq x^+ \leq 820$ $4 \leq y^+ \leq 740$	0.025

Table 5.2 - PIV images data for smooth plate and riblets at $Re_\theta = 2790$. All wall variables indicated with \cdot^+ are scaled by viscous length $l_\tau = 27.3\mu m$ related to the smooth plate.

$Re_\theta = 3900$	Pixel/mm	N° of samples per image	Field size	$\Delta x \Delta y$ (mm)
Smooth	80	830x893	$4 \leq x^+ \leq 1040$ $4 \leq y^+ \leq 970$	0.025
R Long	80	820x893	$4 \leq x^+ \leq 1040$ $4 \leq y^+ \leq 960$	0.025
RS1	92.4	468x632	$4 \leq x^+ \leq 1270$ $8 \leq y^+ \leq 950$	0.0433
RS2	80	815x893	$4 \leq x^+ \leq 1040$ $4 \leq y^+ \leq 950$	0.025

Table 5.3 - PIV images data for smooth plate and riblets at $Re_\theta = 3900$. All wall variables indicated with \cdot^+ are scaled by viscous length $l_\tau = 21.5\mu m$ related to the smooth plate.

$Re_\theta = 4895$	Pixel/mm	N° of samples per image	Field size	$\Delta x \Delta y$ (mm)
Smooth	80	831x893	$6 \leq x^+ \leq 1300$ $6 \leq y^+ \leq 1200$	0.025
R Long	80	823x893	$6 \leq x^+ \leq 1300$ $6 \leq y^+ \leq 1200$	0.025
RS1	92.4	466x632	$6 \leq x^+ \leq 1600$ $10 \leq y^+ \leq 1170$	0.0433
RS2	77	803x893	$6 \leq x^+ \leq 1350$ $6 \leq y^+ \leq 1210$	0.026

Table 5.4 - - PIV images data for smooth plate and riblets at $Re_\theta = 4895$. All wall variables indicated with \cdot^+ are scaled by viscous length $l_\tau = 17.3\mu m$ related to the smooth plate.

The results presented in Section 5.2 and 5.3 for all four boundary layer measurements are related to the free-stream velocity $U_0 = 13.4 m/s$ leading to a Reynolds number $Re_\theta = 2790$ computed through the *momentum thickness* θ .

The viscous length l_τ is different for each plate, but to make possible comparison between them, the length quantities are all scaled by $l_\tau = 27.3\mu m$ corresponding to the viscous length of the smooth plate. The graphic $E(r)$ for the boundary layer is

not evaluated because the extremely chaotic motion makes not possible the identification of structures from it.

For the statistical analysis all three Reynolds numbers will be examined.

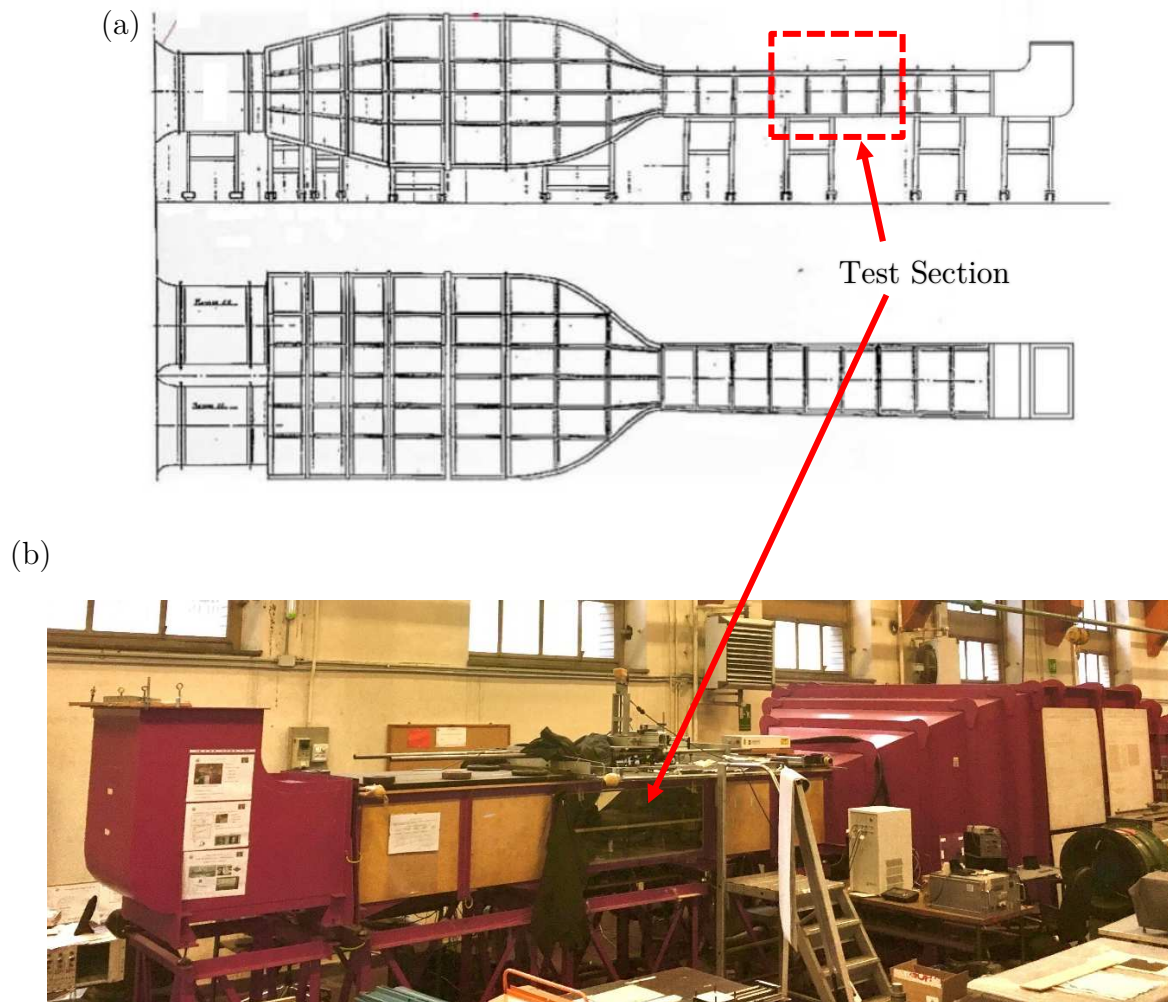


Figure 5.2 -(a) Schematic of the adopted wind tunnel; (up) lateral view and (down) top view; (b) photo of the wind tunnel.



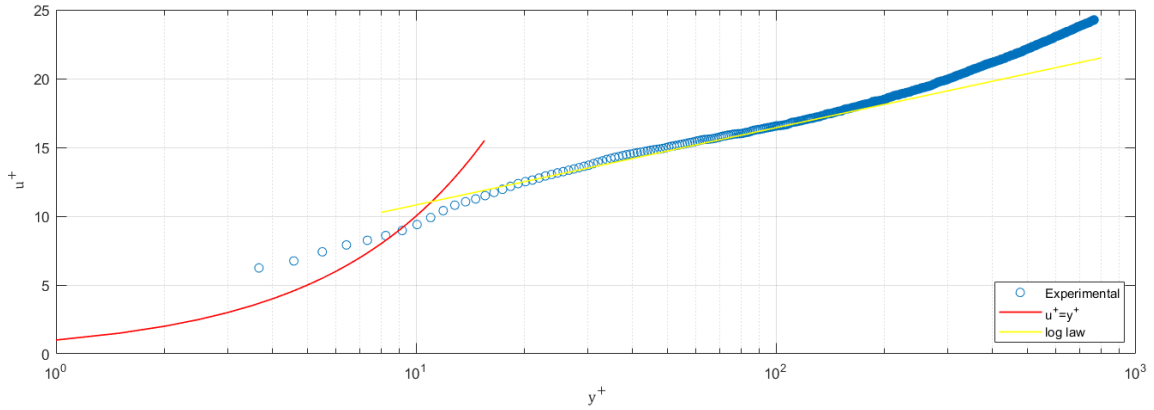
Figure 5.3 - Laser beam pattern entering into the test section (Ref. [18]).

5.2 Smooth plate

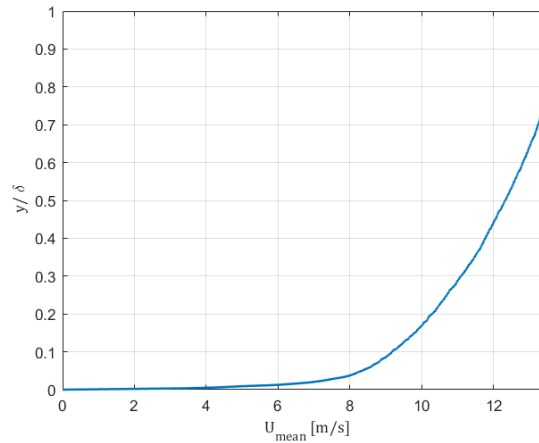
The turbulent boundary layer results to be very complex due to its remarked multiscale nature and the extremely chaotic motion.

By means the viscous length, the inner variable u^+ , y^+ and x^+ can be defined as previously described in Section 4.1.

The mean velocity profile for $x^+ \simeq 360$ with viscous and outer variables is depicted in Figure 5.4. The experimental data lie over the linear law curve ($u^+ = y^+$) with the first point located at about $y^+ = 3.5$, so within the viscous sublayer and then proceed through the buffer layer and the log law region with good approximation. The sampling domain stay within the boundary layer without going in the free-stream.



(a)



(b)

Figure 5.4 - Mean velocity profile of boundary layer at $x^+ \simeq 360$ expressed by means (a) inner variables and (b) outer variables where $\delta(x)$ represents the boundary layer thickness for a fixed x .

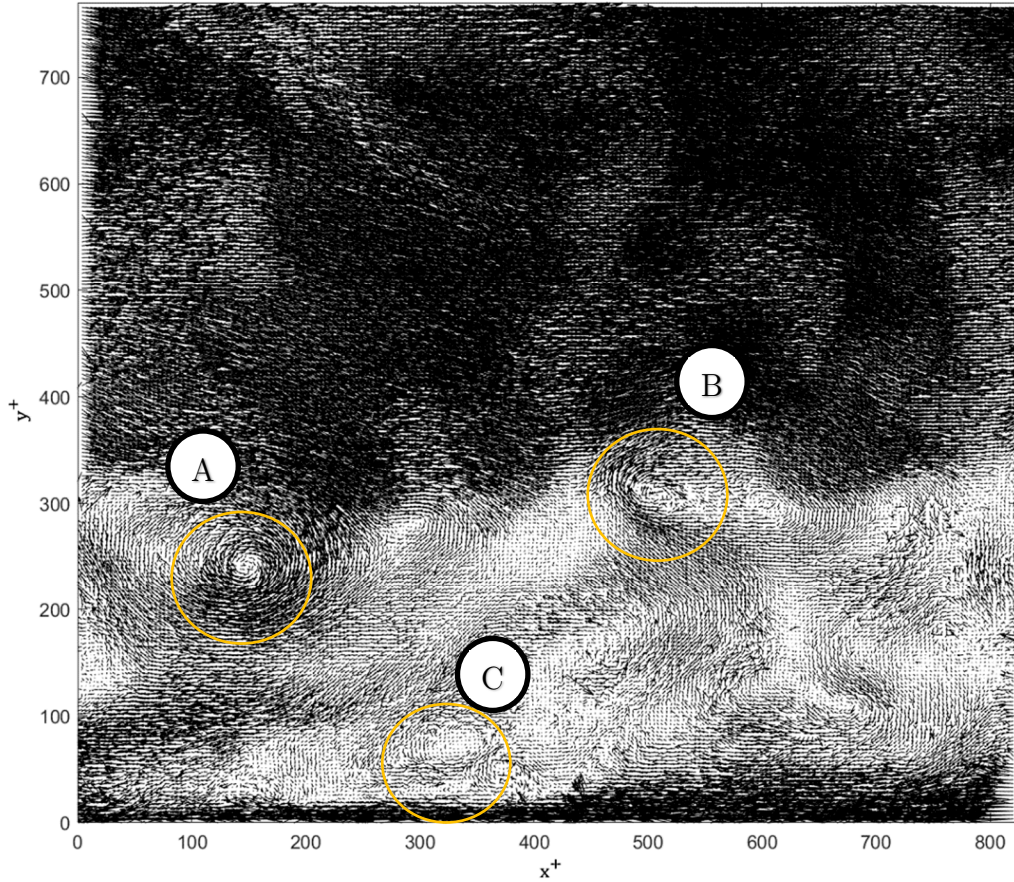


Figure 5.5 - Galilean flow field of turbulent boundary layer over a flat plate at null angle of attack with convective velocity $U_a = 0.7U_0$. Three structures labelled as A, B and C are visible.

The Galilean vector field of the first snapshot examined is reported in Figure 5.5, where the advective velocity U_a is equal to 70% of the free-stream velocity U_0 . Inside the chaotic tangle of the turbulent motion two vortices, indicated as A and B, are well visible.

We performed the wavelet analysis for the entire flow field and the wavelet maps at scales which reveal the presence of a coherent structure are reported in Figure 5.6. We can spot the two structures A and B, but C is not visible at this scale neither at lower scale due to its position $y^+ < 100$ where the boundary layer is extremely chaotic and it is merged with some other “structures”. We, also, notice, just above the vortex B, a small area of energy. Indeed, if we change the convective velocity U_a from 70% to 95% of the free-stream velocity, the structure D appears in the Galilean vector field as showed by Figure 5.7. Indeed, if one takes into account more than one value of the convective velocity ranging, for example, from 60% to 100% of the free-stream velocity U_0 , for each value of U_a different vortices can show up just because they move within the flow field with velocity U_a .

5 Wavelet analysis of turbulent boundary layer

These vortices seem to be what Adrian [9] and others have described as *hairpin vortices*, and specifically, what we see corresponds to the heads of hairpins.

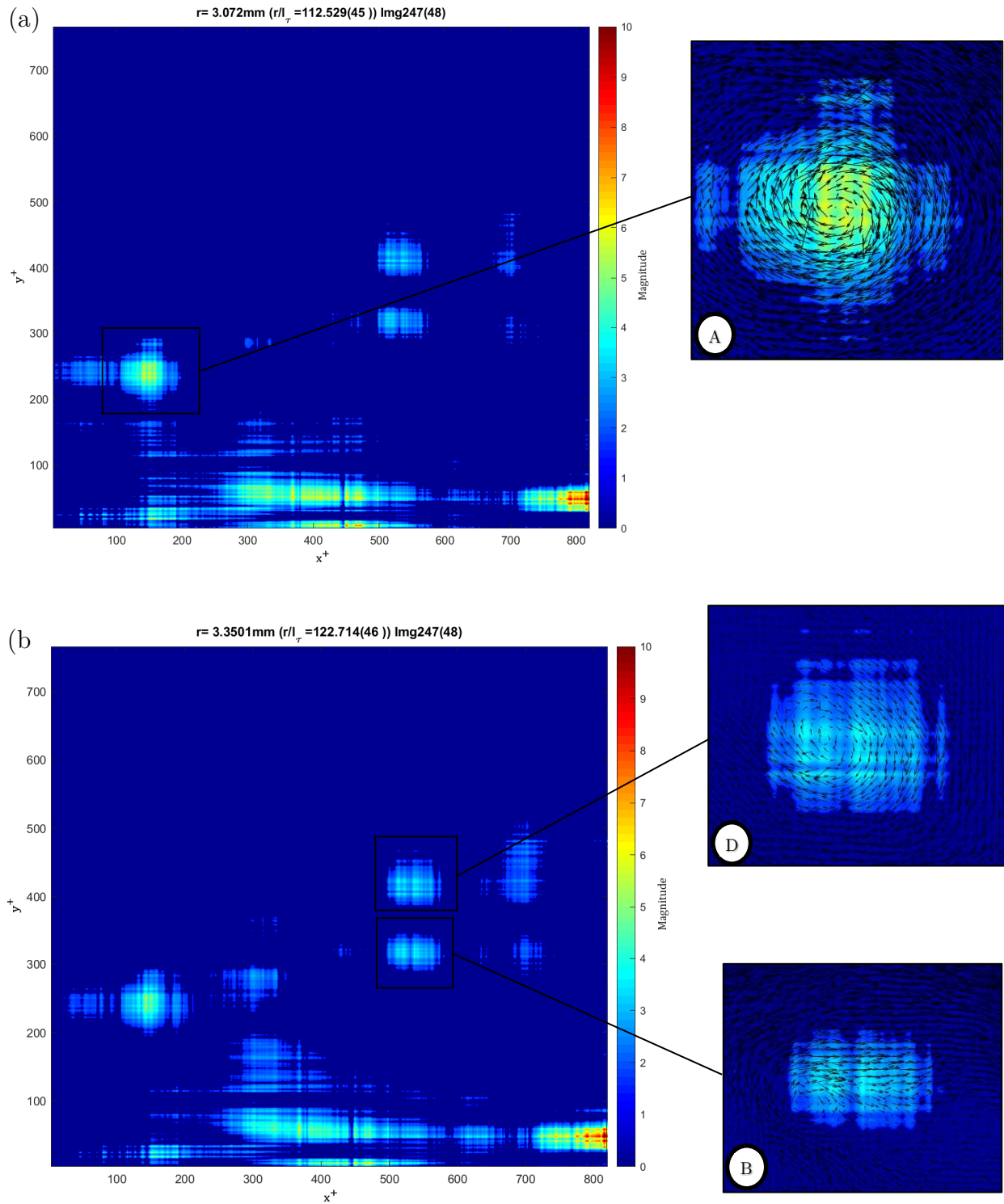


Figure 5.6 - Wavelet maps for (a) $r^+ = 112$ and (b) $r^+ = 122$ show three different vortices while in the lower part of the images there are some energy strips.

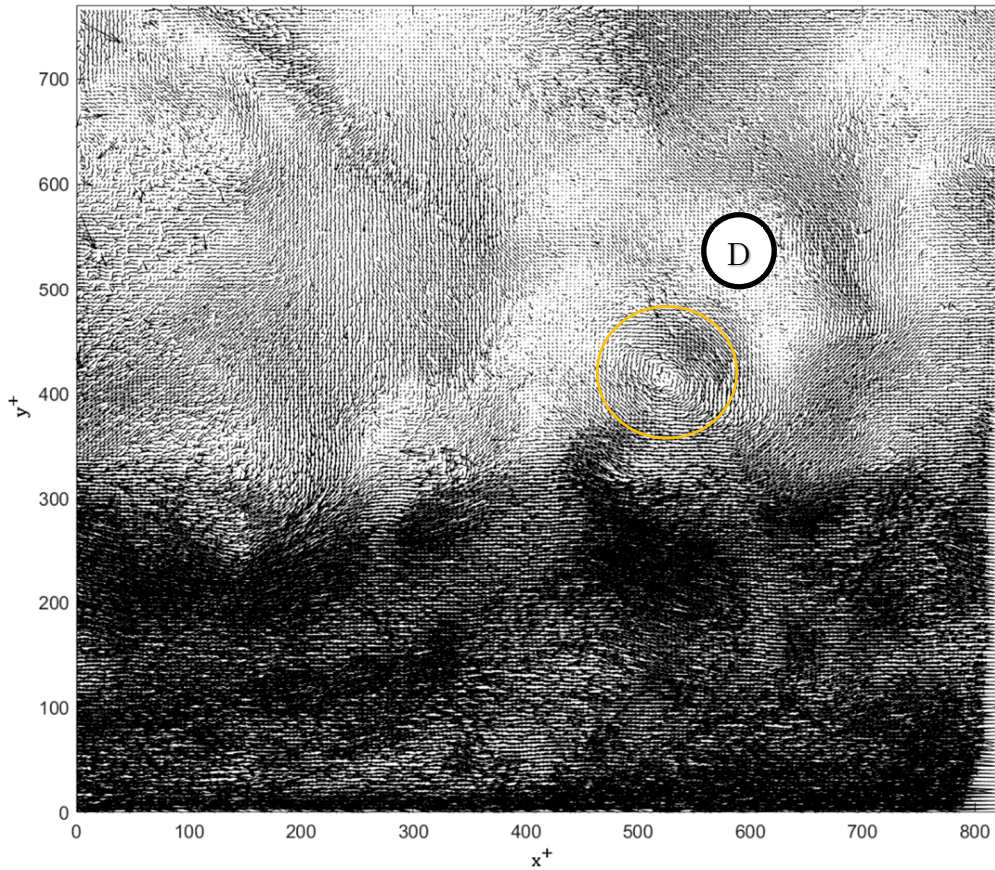


Figure 5.7 - Galilean vector field with an increased convective velocity to $U_a = 0.95U_0$ shows one more coherent structure.

As previously mentioned, in the bottom of the wavelet maps some energy strip are visible and decreasing the resolution, we obtain the map reported in Figure 5.8.

It is too difficult to say what type of structure they are. Perhaps, they can be *streaks* or also the legs of hairpin vortices.

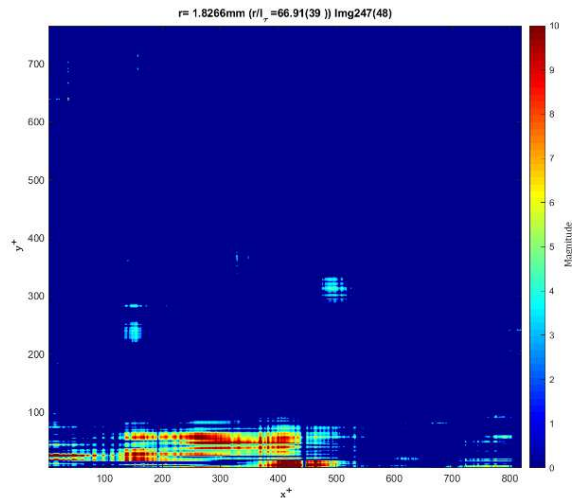


Figure 5.8 - Wavelet map at low scales which shows the presence of energy concentration in the lower side of the map.

5.3 Riblet surfaces

We present here some wavelet maps for the three types of riblets. These results are, obviously, very similar to smooth plate results. Distinction between boundary layers can be highlighted through a statistical analysis of data in the attempt to catch a different behaviour of smooth and riblet surfaces. Many studies have been made analysing the turbulent statistics of the velocity field. In Section 5.4 we try to evaluate statistics of the wavelet-transformed flow field.

Longitudinal riblets

Many snapshots were evaluated, and some significative results are provided. The flow field displayed by the Galilean transform reported in Figure 5.9 shows a clear vortex circled and labelled as A considering an advection velocity U_a equal to 70% of the free-stream U_0 . This vortex is correctly identified by the wavelet analysis. Indeed, for a resolution of $r^+ \simeq 145$ the energy concentration corresponds exactly with the coherent structure of the A zone (see Figure 5.10). We notice another energy concentration just beneath the clear vortex. Figure 5.9 doesn't provide a clear view of what is there, but perhaps, another structure is present. The superimposed velocity vector field over the wavelet map shows the almost perfect matching and the correct detection of the coherent structure which probably corresponds to a hairpin vortex's head, while the area below it is not identified.

5 Wavelet analysis of turbulent boundary layer

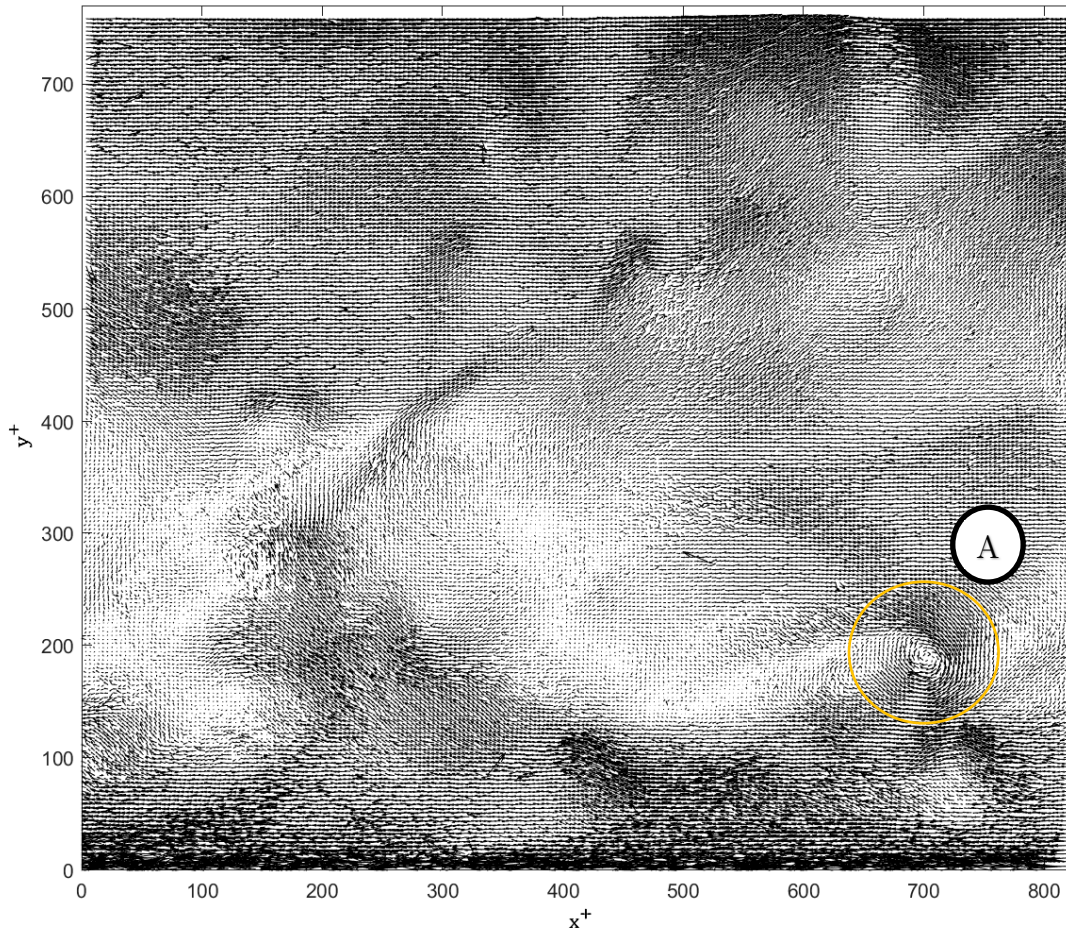


Figure 5.9 - Galilean transform of boundary layer velocity field over longitudinal riblet surface with convective velocity $U_a = 0.7U_0$.

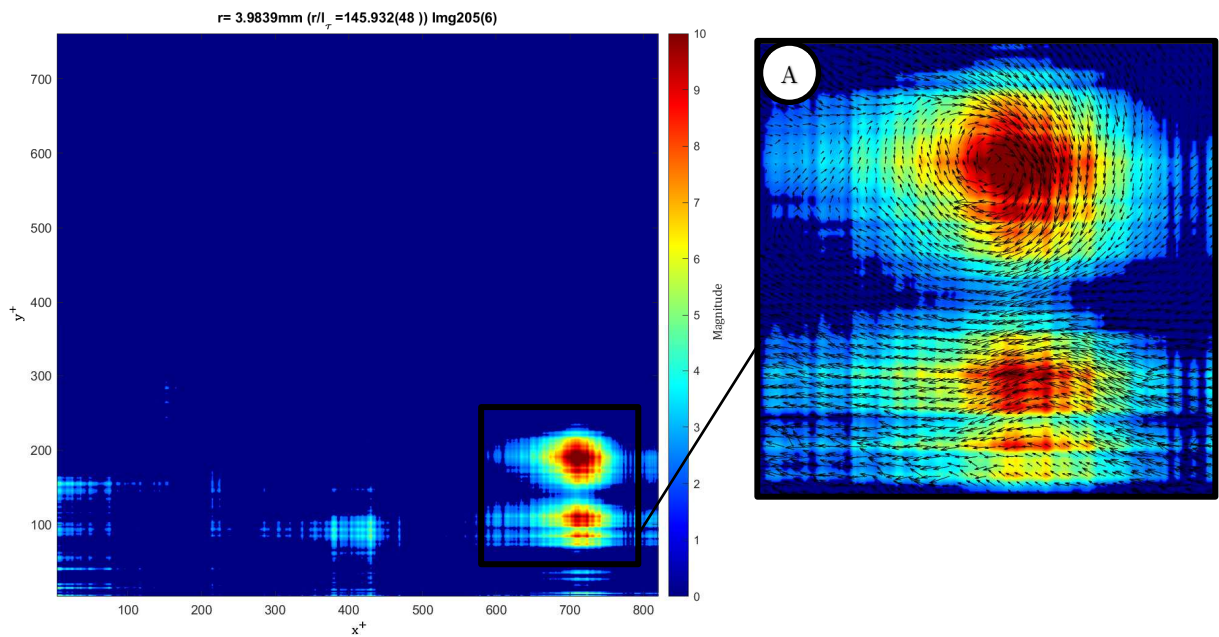


Figure 5.10 - Wavelet map and vortex visualization.

Sinusoidal Riblets 1

The flow field over the first type of sinusoidal riblet surface is reported in Figure 5.11. Two vortices labelled as A and B are clearly visible, while a third vortex is barely visible in the zone C. The wavelet map reported in Figure 5.12 enlightens all three coherent structures for slightly different scales. These, as said before, are probably hairpin vortex's heads, but it depends on where exactly the x-y laser plane has cut the horseshoe. Indeed, the C structure is not well defined, maybe because it can be part of the hairpin but not exactly the head. The sequence of A, B and C structures lead to think to a *packet* of hairpins.

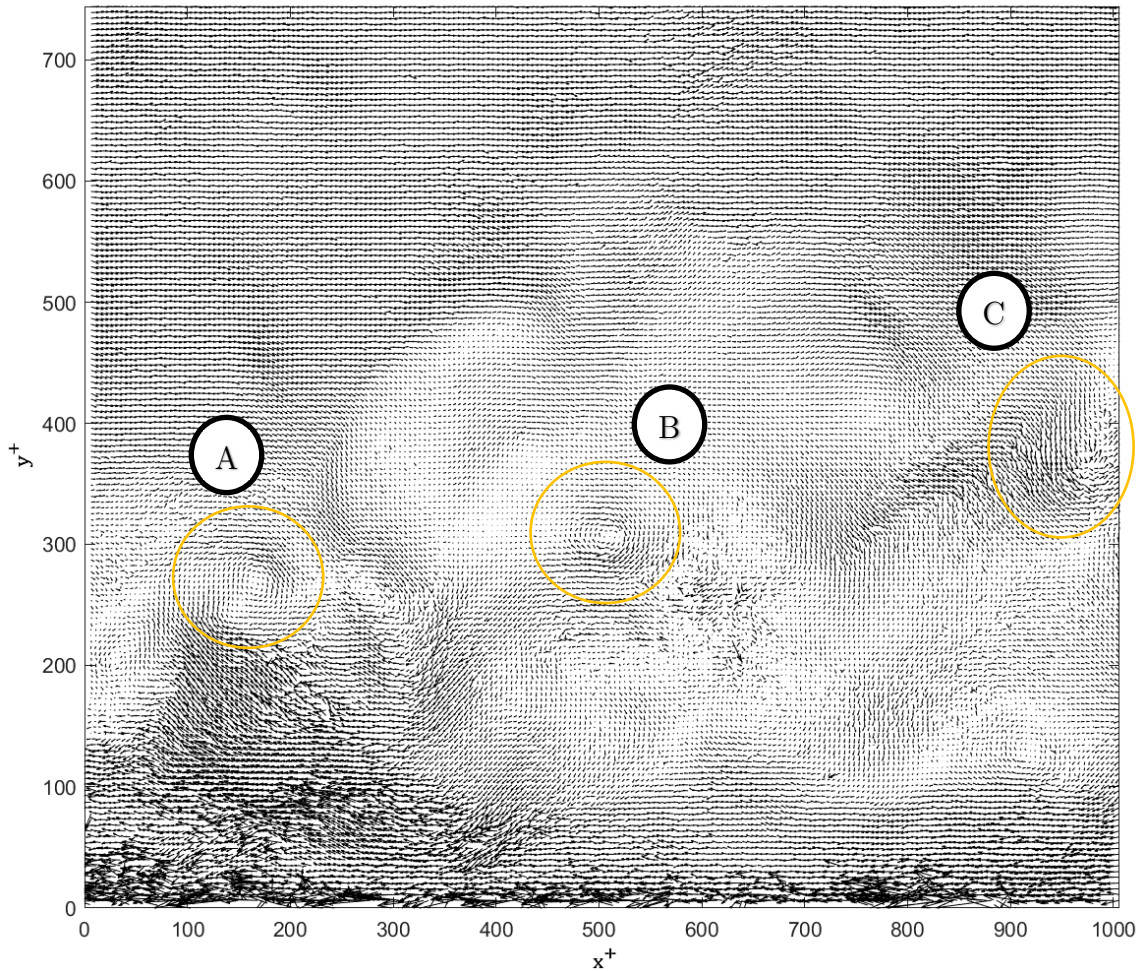


Figure 5.11 - Galilean transform of boundary layer velocity field over sinusoidal type 1 riblet surface with convective velocity $U_a = 0.85U_0$.

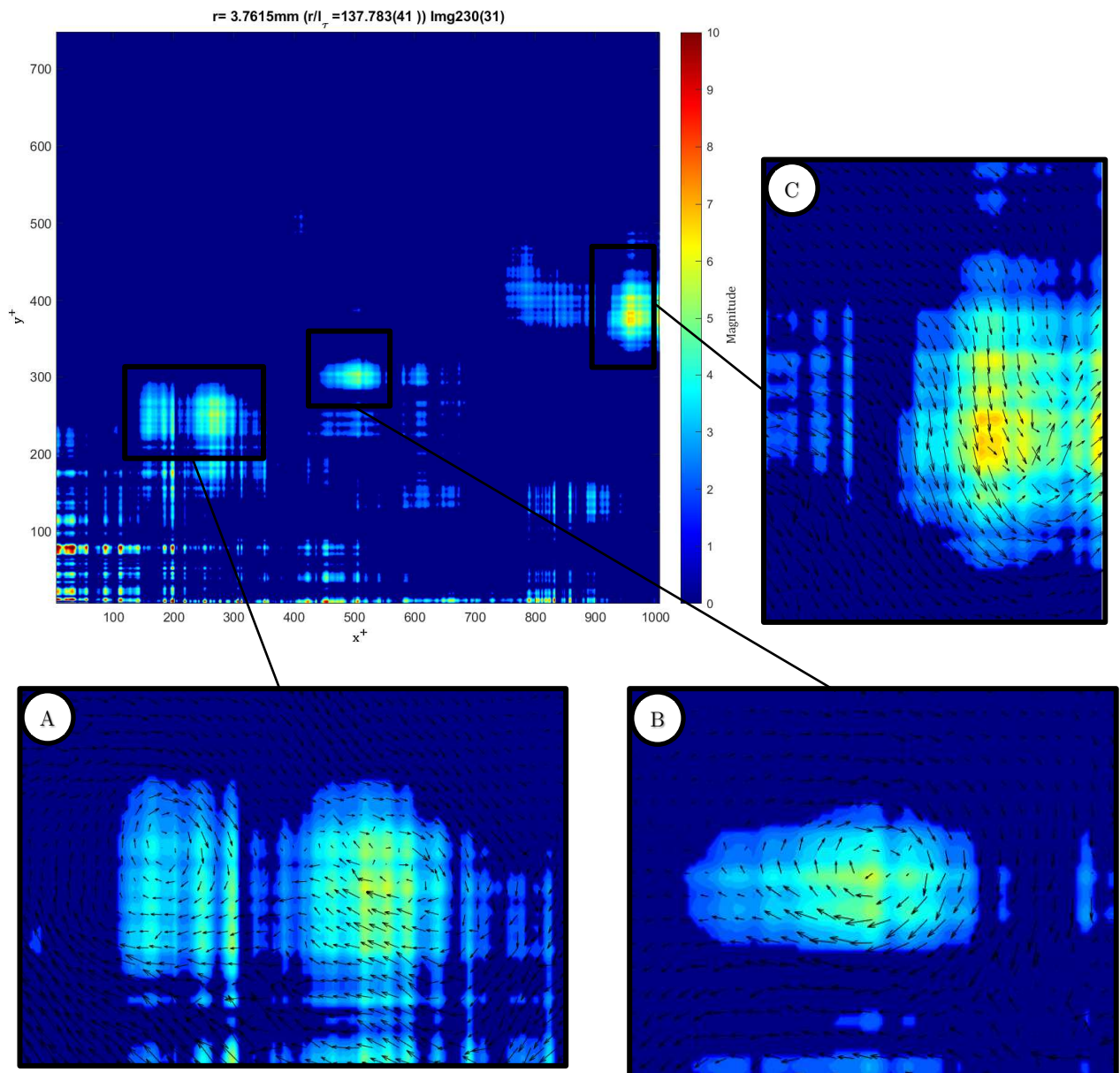


Figure 5.12 - Wavelet map and vortex visualization.

Sinusoidal Riblets 2

Figure 5.13 and Figure 5.14 show the boundary layer over the second type of sinusoidal riblets which have same wavelength, but a greater amplitude of the sinusoid than R S1 (see Table 5.1). As previously observed many structures appear. There are many energy contributions which are not well linked with observable vortices, and probably, they are related to areas which present anyway a space-correlation for the cross-energy density, so for the vorticity intensity of coherent structures.

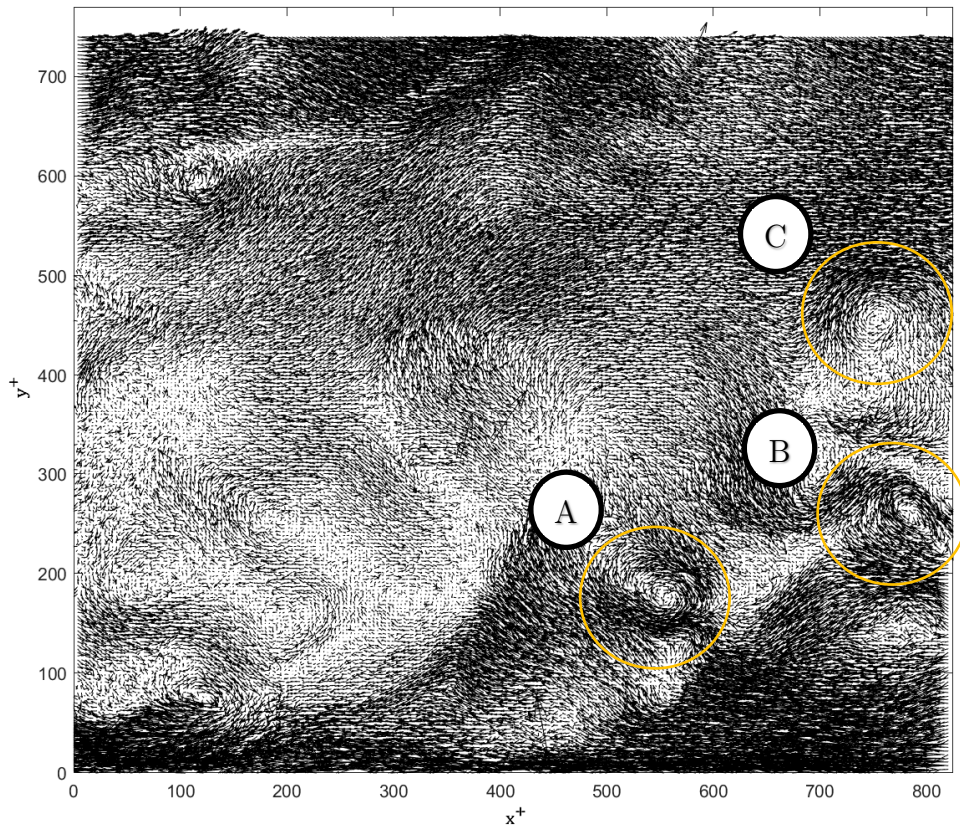


Figure 5.13 - Galilean transform of boundary layer velocity field over sinusoidal type 2 riblet surface with convective velocity $U_a = 0.8 U_0$.

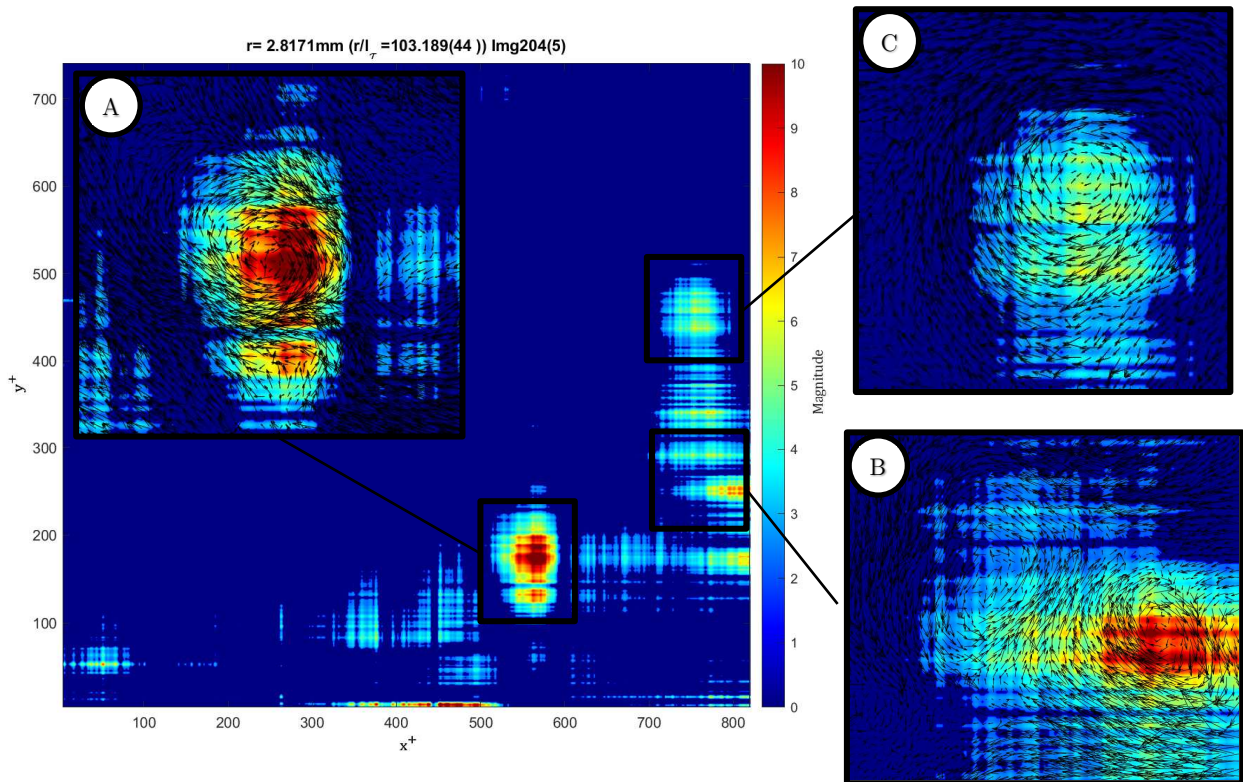


Figure 5.14 - Wavelet map and vortex visualization.

5.4 Statistical analysis

The performed statistical analysis is based on the evaluation of the mean energy at each y^+ and at each scale or resolution value. In order to allow a comparison between the four different boundary layer flow fields the quantity $E(x_1, x_2)^r$ which is defined in eq. (2.9), need to be reshaped. The introduced quantity is called as $E_{w,t}(x_1, x_2)^r$ and represents the numerator of the eq. (2.9) where t is the instantaneous PIV snapshot and r the scale

$$E_{w,t}(x_1, x_2)^r = [(w_{1,2}^r w_{1,2}^{r*})(w_{2,1}^r w_{2,1}^{r*})]^{1/2} \quad (5.1)$$

The difference between the two quantities lies in the normalization of $E(x_1, x_2)^r$ which, as previously mentioned, becomes the 2D counterpart of LIM.

With eq. (5.1), comparison between different fields is possible, since we excluded the denominator of eq. (2.9) which is different for each wavelet map at each scale.

The following operation is performed for each y^+ , r and t values:

$$E_{w,t}(y)^r = \frac{1}{L} \int_0^L E_{w,t}(x, y)^r dx \quad (5.2)$$

where L is the total streamwise distance. The eq. (5.2) represents the mean value of the cross-energy density at each y^+ at the scale r and snapshot t . The value of t represents a temporal instant, but due to a lack of time-correlation between two successive snapshots, t accounts for the snapshots' number which run from 1 to 2000. So, since we have discrete data the eq. (5.2) is expressed for a discrete domain as:

$$E_{w,t}(y)^r = \frac{1}{N_x} \sum_{i=1}^{N_x} E_{w,t}(i, y)^r \quad (5.3)$$

where N_x is the total number of spatial samples along the streamwise direction x . At this point, we performed the time-average of eq. (5.3)

$$E_w(y)^r = \frac{1}{T} \int_0^T E_{w,t}(y)^r dt = \text{discrete} = \frac{1}{N_t} \sum_{j=1}^{N_t} E_{w,j}(y)^r \quad (5.4)$$

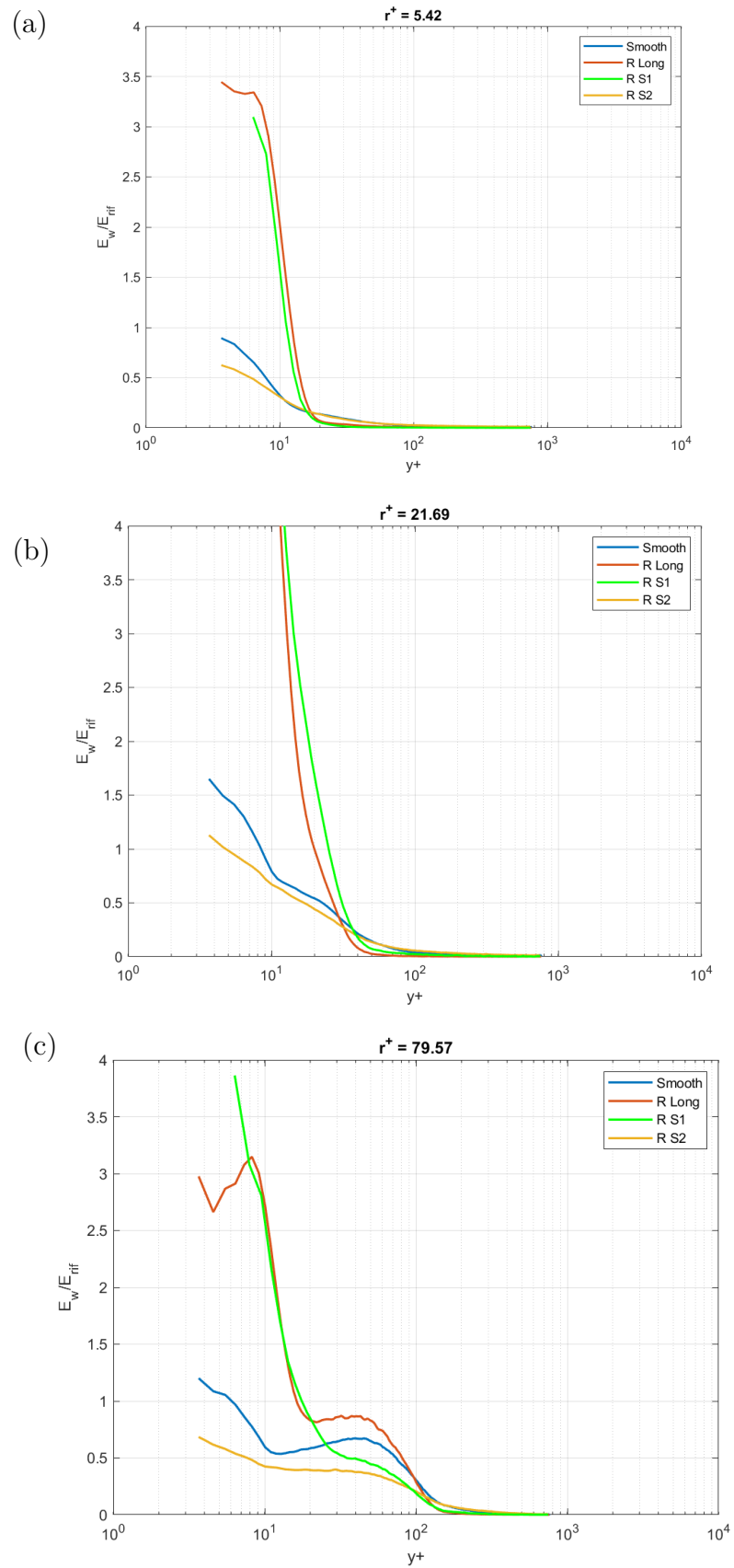
with N_t the total number of PIV snapshots ($N_t = 2000$).

The eq. (5.3) and (5.4) are applied to wavelet maps of smooth and riblet plates. Results for some scales r^+ are showed in Figure 5.15, Figure 5.16 and Figure 5.17 for the three Reynolds number $Re_\theta = 2790$, $Re_\theta = 3900$ and $Re_\theta = 4895$ corresponding to $U_0 = 13.4m/s$, $U_0 = 18.2m/s$ and $U_0 = 22.7m/s$, respectively.

The quantity E_{rif} is defined as follow with notation $\langle \cdot \rangle$ representing the spatial average over the whole map for the larger scale and it refers to the smooth plate.

$$E_{rif} = \frac{1}{N_t} \sum_{j=1}^{N_t} [\langle w_{1,2}^r w_{1,2}^{r*} \rangle \langle w_{2,1}^r w_{2,1}^{r*} \rangle]_j^{1/2} \quad (5.5)$$

5 Wavelet analysis of turbulent boundary layer



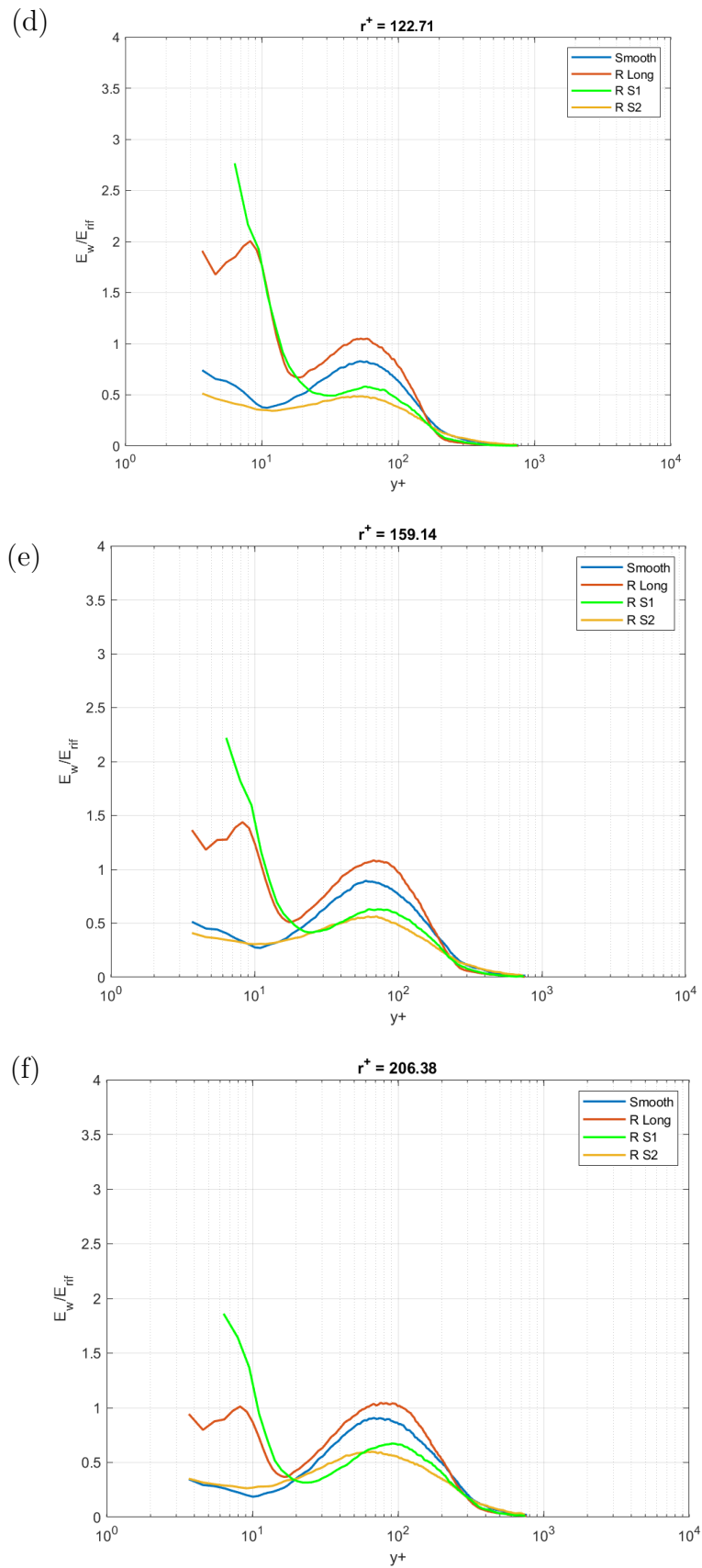
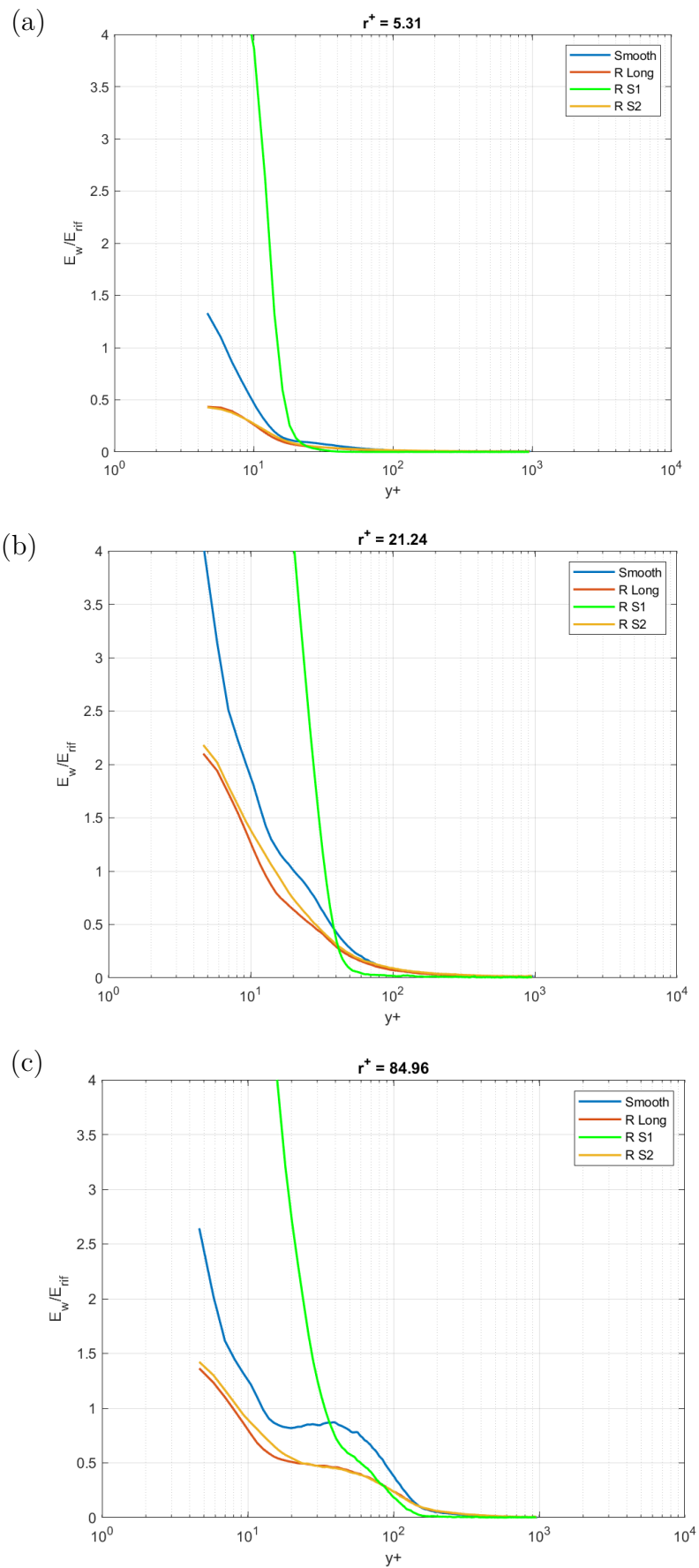


Figure 5.15 - Statistics of energy distribution for smooth and riblet surfaces at $Re_\theta = 2790$; r^+ is obtained through $l_\tau = 27.3\mu m$.

5 Wavelet analysis of turbulent boundary layer



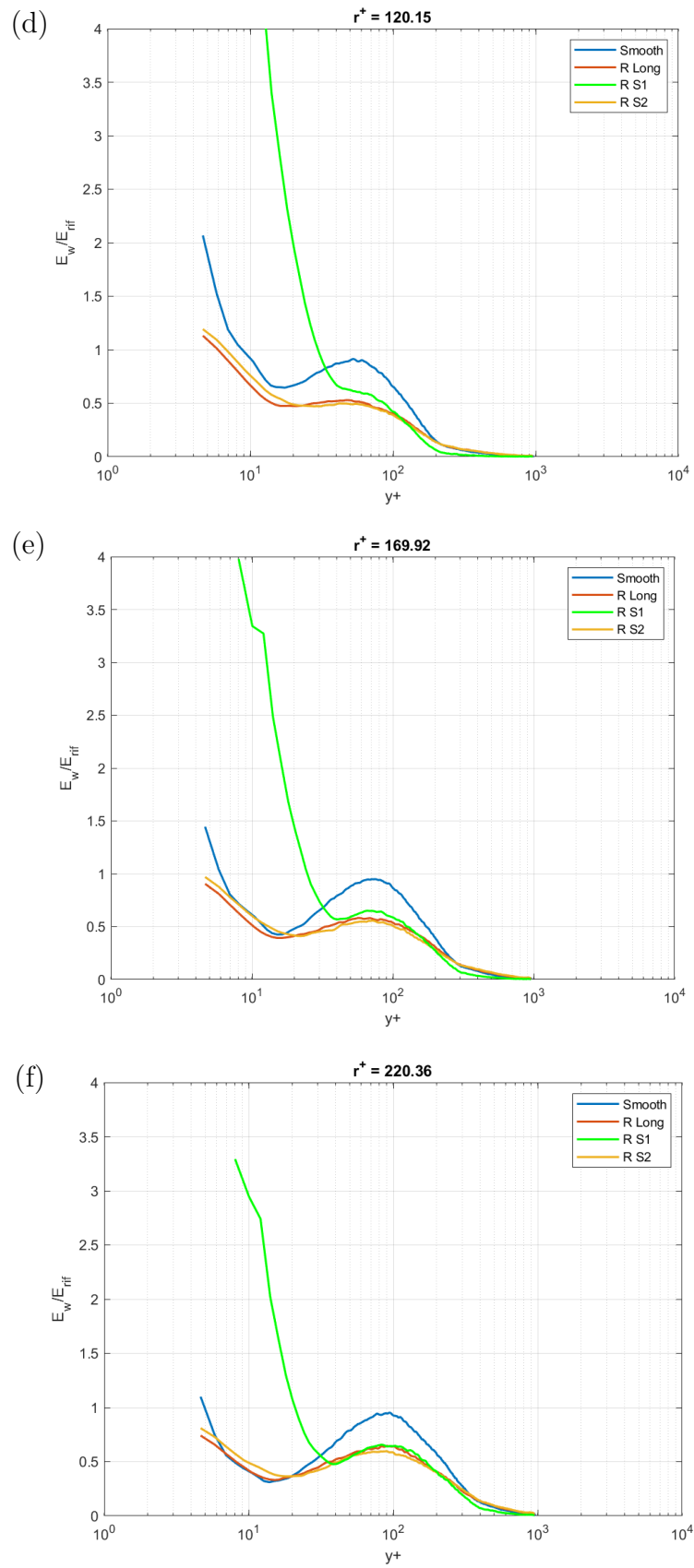
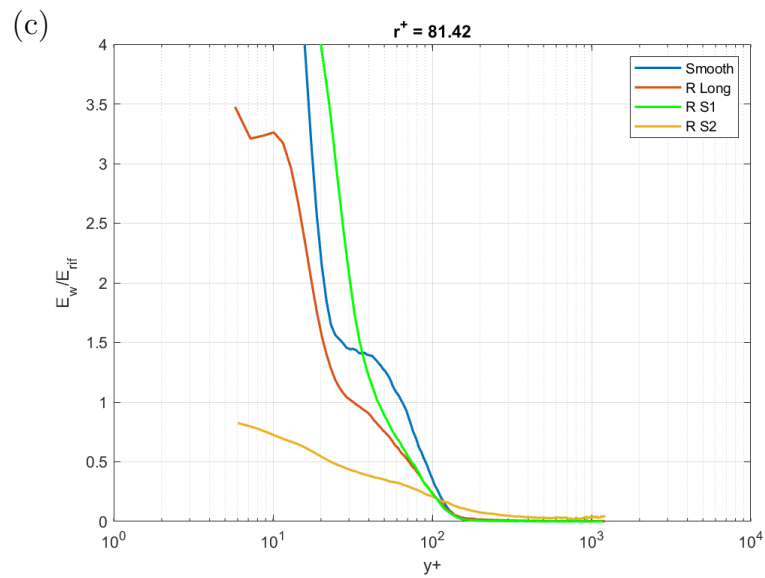
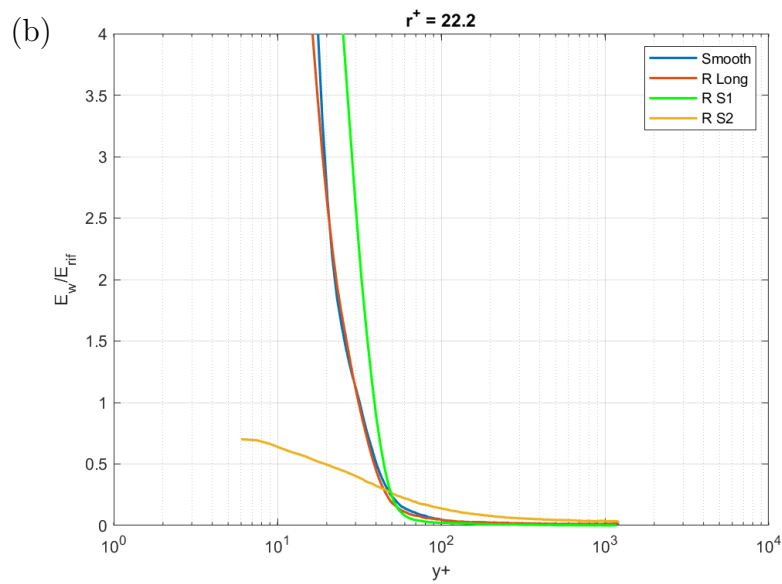
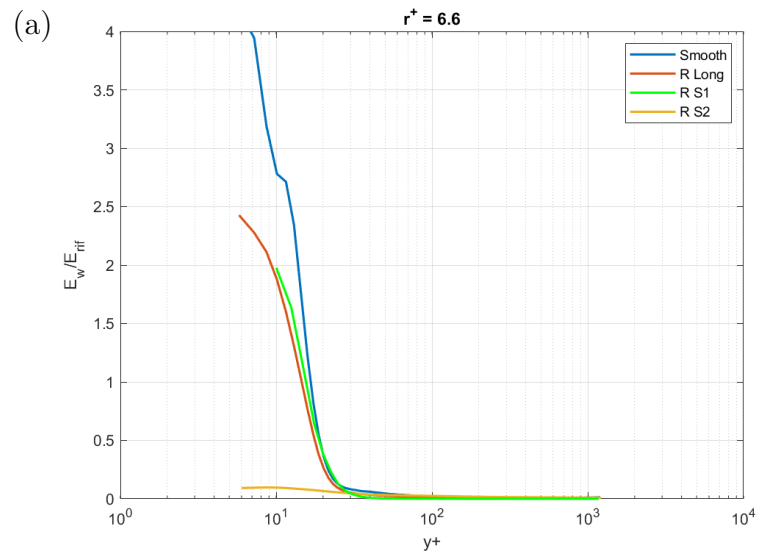


Figure 5.16 - Statistics of energy distribution for smooth and riblet surfaces at $Re_\theta = 3900$; r^+ is obtained through $l_\tau = 21.5 \mu m$.

5 Wavelet analysis of turbulent boundary layer



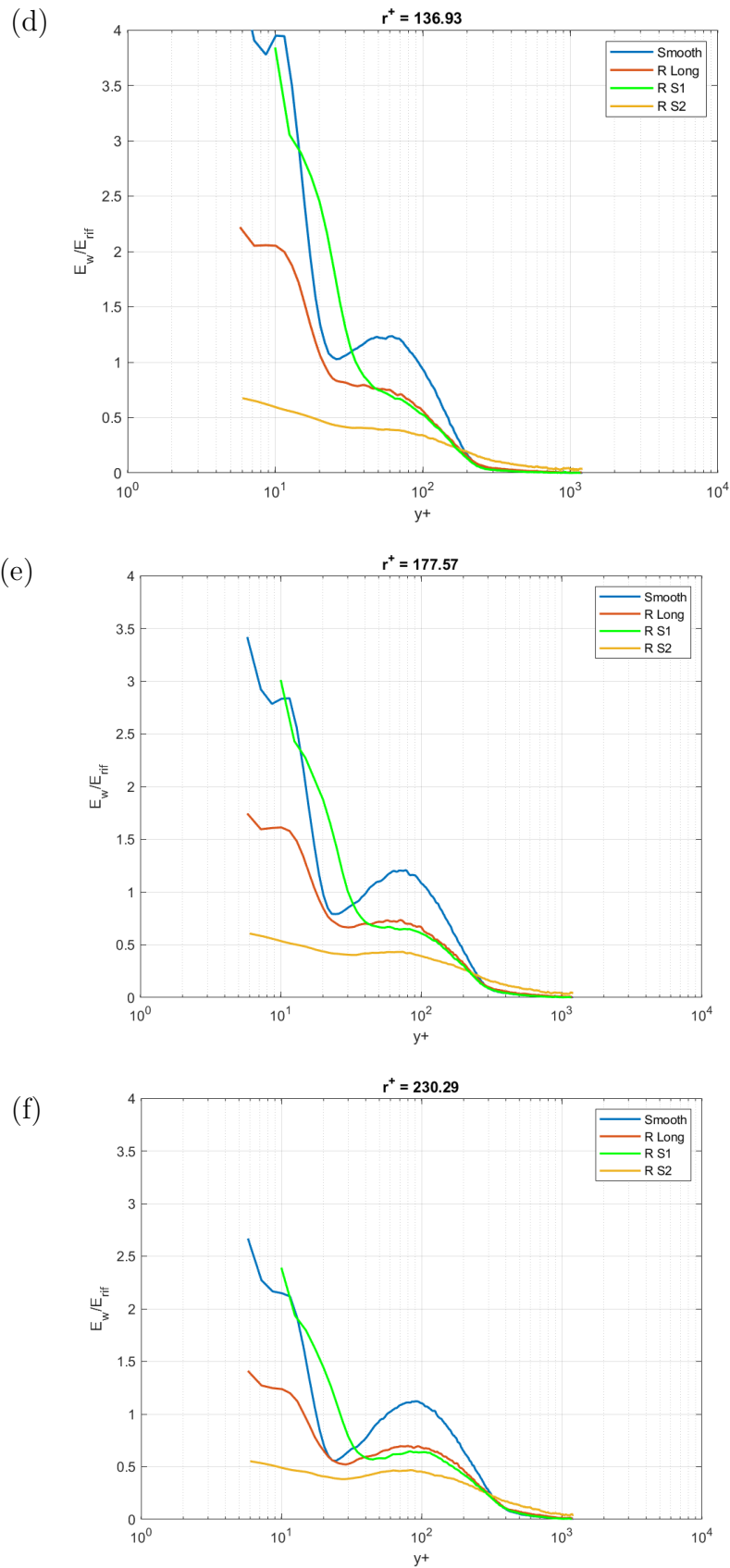


Figure 5.17 - Statistics of energy distribution for smooth and riblet surfaces at $Re_\theta = 4895$; r^+ is obtained through $l_\tau = 17.3\mu m$.

For all Reynolds numbers, the larger scales show a peak value for $50 < y^+ < 100$ approximately, which slowly moves toward lower y^+ as the scale r^+ decreases.

As said before, the $E_w(y^+)^r$ is the mean value of the cross-energy density and it is somehow linked to the spanwise vorticity as well as $E(x_1, x_2)^r$ which enlighten the high vorticity areas at different scales related to coherent structures. Therefore, the curves should indicate the cross-energy density level of “coherent structures” which also incorporate sweeps, ejections or hairpin legs which probably cause the distribution of energy visible for about $y^+ < 150$, despite we have not a reliable confirmation.

The lowest Reynolds number $Re_\theta = 2790$ (see Figure 5.15) shows how the curves related to the sinusoidal type 1 and 2 riblets (R S1 and R S2, respectively) have a lower peak than the smooth plate for larger scales while the longitudinal riblets (R Long) shows the same shape but higher values within the logarithmic region. In the near-wall region both R Long and R S1 riblets show a greater amount of energy than the smooth plate.

This seems like the longitudinal riblets for larger scales within the logarithmic region presents a greater value of turbulent activity with respect to the smooth plate, while both sinusoidal riblets shows a lower activity. This, probably, turns in good drag reduction performances for R S1 and R S2, while for R Long a drag increase is obtained with respect to the smooth plate performances at this Reynolds number.

At Reynolds number $Re_\theta = 3900$ (see Figure 5.16), the energy content of longitudinal and sinusoidal type 2 riblets is nearly always lower than the smooth plate values, while sinusoidal type 1 riblets shows values greater than the smooth plate curves only for $y^+ < 25$.

Lastly, at $Re_\theta = 4895$ (see Figure 5.17), approximately, the same behaviour for all the surfaces is observed with respect to $Re_\theta = 3900$.

The proposed results need a more accurate investigation to better understand the behaviour of coherent structures within the boundary layer. With present data a deeper investigation is almost not feasible.

However, according to present outcomes, we can hypothesize that all riblets have good drag reduction performances almost for all three Reynolds numbers examined, except an increased activity observed for R Long at $Re_\theta = 2790$, but the sinusoidal riblets type 2 seems to play a better role in drag reduction performances with respect to the other two riblet surfaces. The different sinusoid amplitude, specifically greater than the amplitude of R S1, can be the key for the marked difference in

behaviour. Probably, the enhanced amplitude acts like an oscillating plate with an increased oscillating amplitude. The R S2 plate can break the vortical structures better than others do. Thus, the turbulent activity is decreased.

Results at larger scales need a critical evaluation. Indeed, the amount of energy represented is due to the whole area interested by coherent structures, which in the wavelet map would not appear as single structures at larger scales. In fact, the energy of single structures can be distributed between them, covering the entire area interested by coherent structures without distinction between them, because of the stretching of the wavelet reaches values which englobe contribution of all structures. So, the peak visible at larger scales for $y^+ \simeq 100$ indicates where most of the structures are placed and the turbulent activity intensity.

The great out of scale peak which characterizes the R Long and R S1 for small scales well visible for $Re_\theta = 2790$ can find an explanation in the following reason.

At very small scales, the procedure of wavelet analysis enlightens the very tiny high-vorticity areas which in the near-wall region are hugely enhanced for both plates, while for smooth and RS2 plate this behaviour is not encountered. We show in Figure 5.19 the wavelet maps of one snapshot for each surface, and it is clear the presence of high-energy areas along the near-wall region for R Long and R S1, while for smooth and R S2 plates the energy content is lower and not only concentrated near the wall. Thus, R Long and R S1 enhance the spanwise vorticity as confirmed by the Figure 5.18, where the root mean square value of spanwise vorticity is reported, showing a significative peak for R Long and R S1.

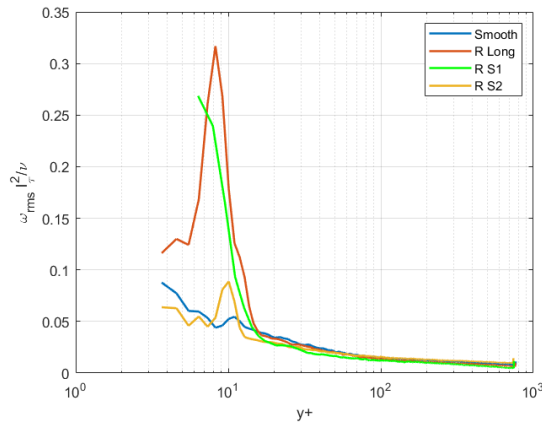


Figure 5.18 - Root mean square of spanwise vorticity at $Re_\theta = 2790$.

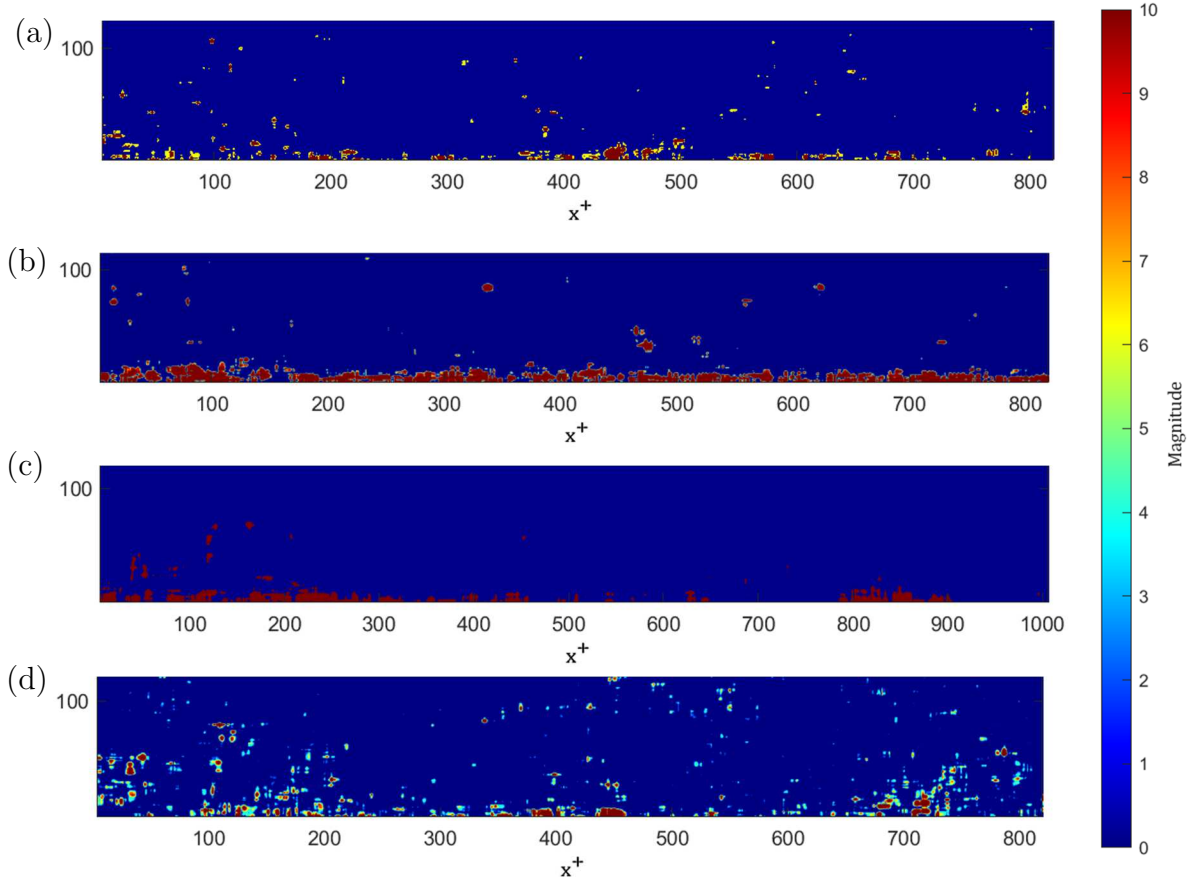


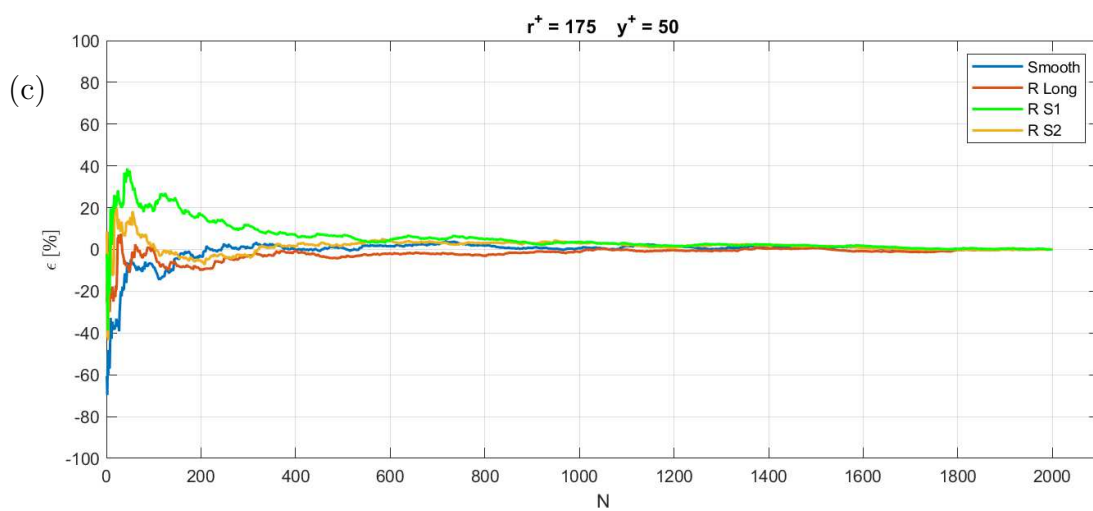
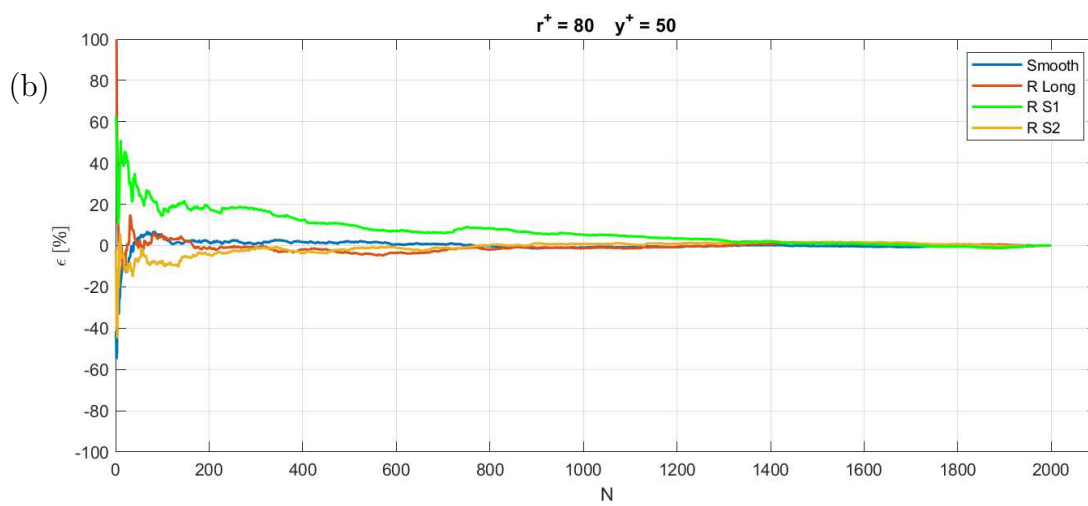
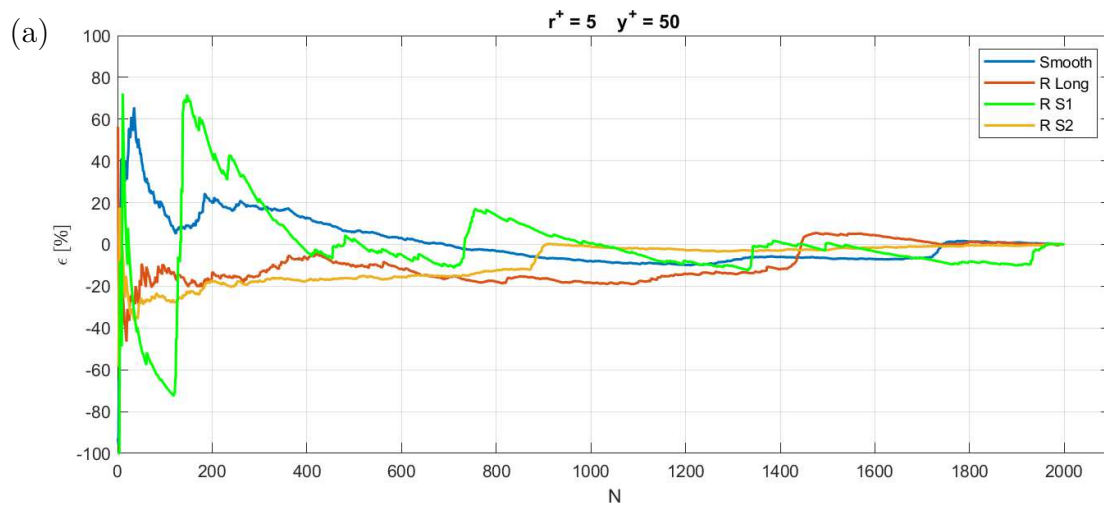
Figure 5.19 - Wall region focus of wavelet maps at low scales of (a) smooth plate and (b) longitudinal, (c) sinusoidal 1 and (d) sinusoidal 2 riblets at $Re_\theta = 2790$.

Lastly, the convergence analysis of statistics is performed. In order to evaluate convergence characteristics for different values of r^+ and y^+ the following quantity is defined:

$$\epsilon = \frac{E_n - E_N}{E_N} * 100$$

where E_N is the mean value over the whole set of samples and E_n is the mean value at the n th iteration over the n samples both concerning quantity $E_w(y^+)^r$ for a set of $N = 2000$ images for each plate. Results are reported in Figure 5.20, Figure 5.21 and Figure 5.22. For low-scales and high y^+ values we notice a not very good convergence behaviour, while for higher r^+ and lower y^+ the value of ϵ is within 2%.

5 Wavelet analysis of turbulent boundary layer



5 Wavelet analysis of turbulent boundary layer

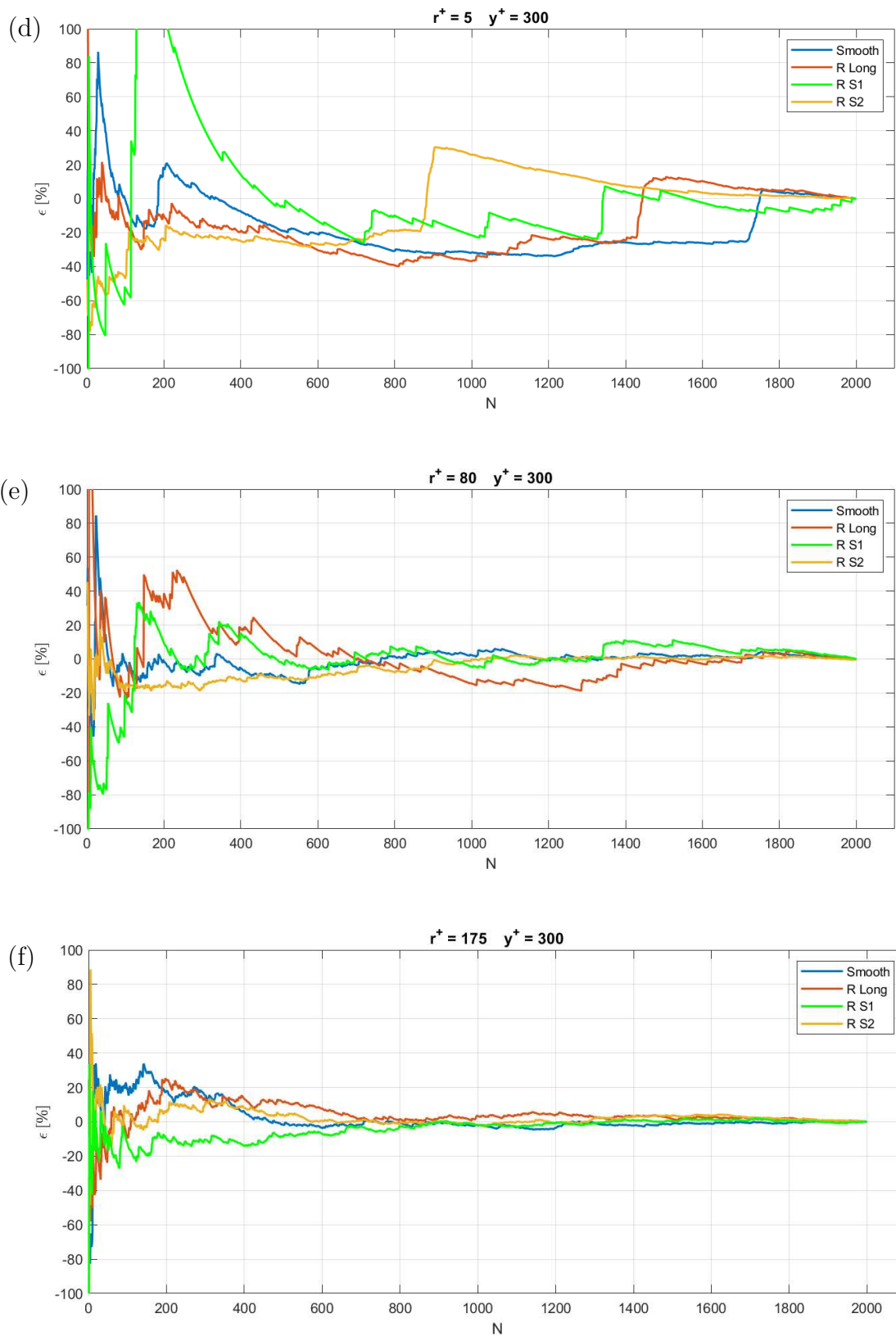
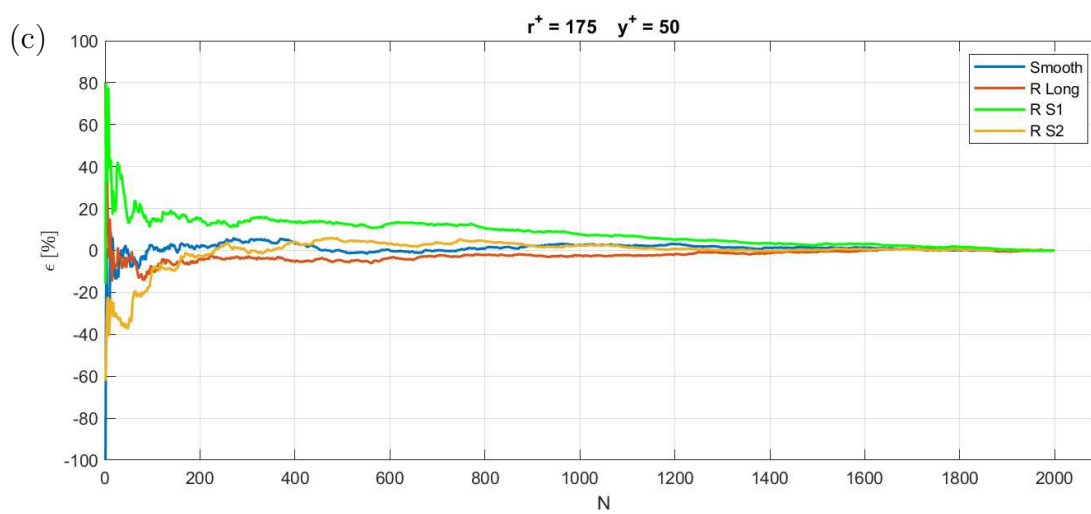
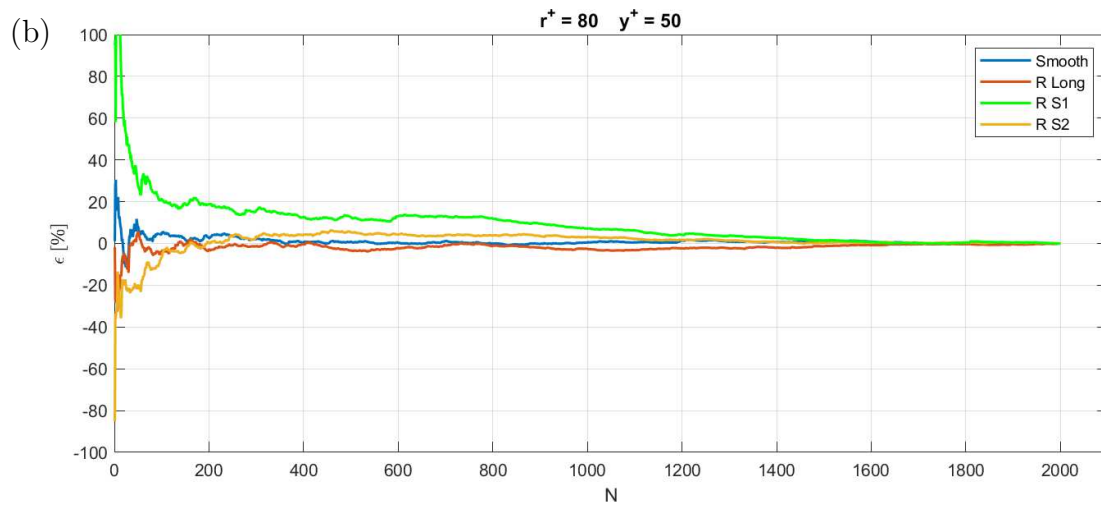
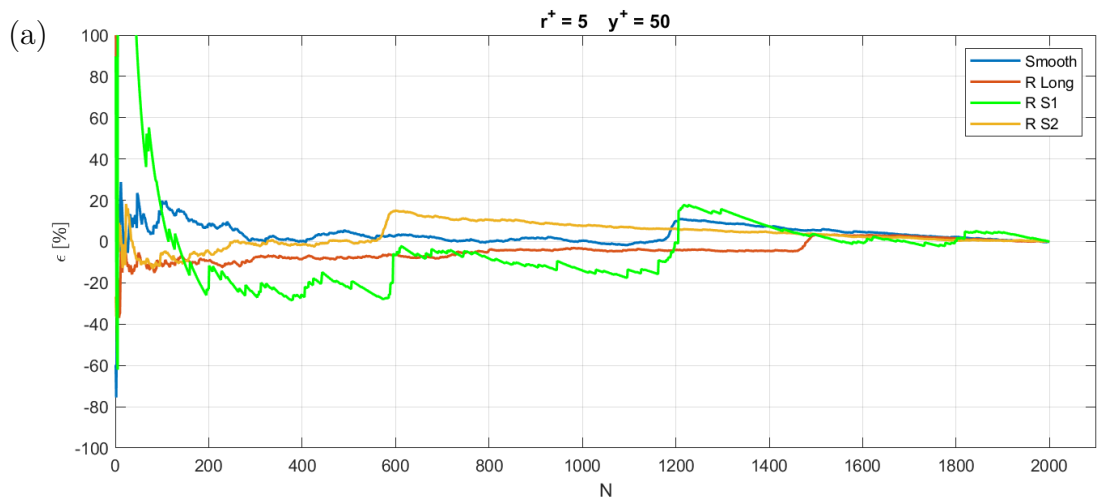


Figure 5.20 - Convergence curves for different scales r^+ and wall-normal coordinate y^+ at $Re_\theta = 2790$.

5 Wavelet analysis of turbulent boundary layer



5 Wavelet analysis of turbulent boundary layer

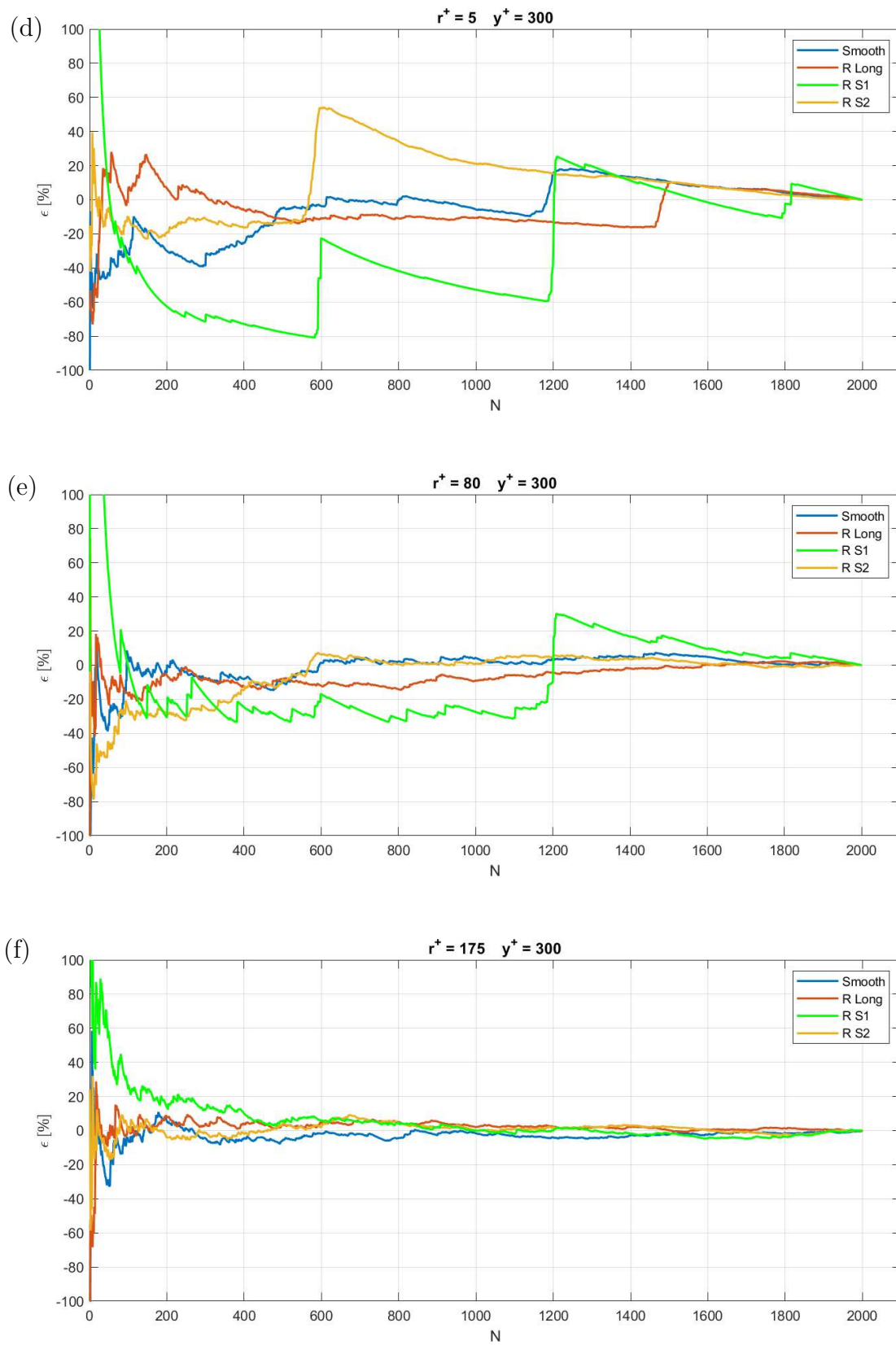
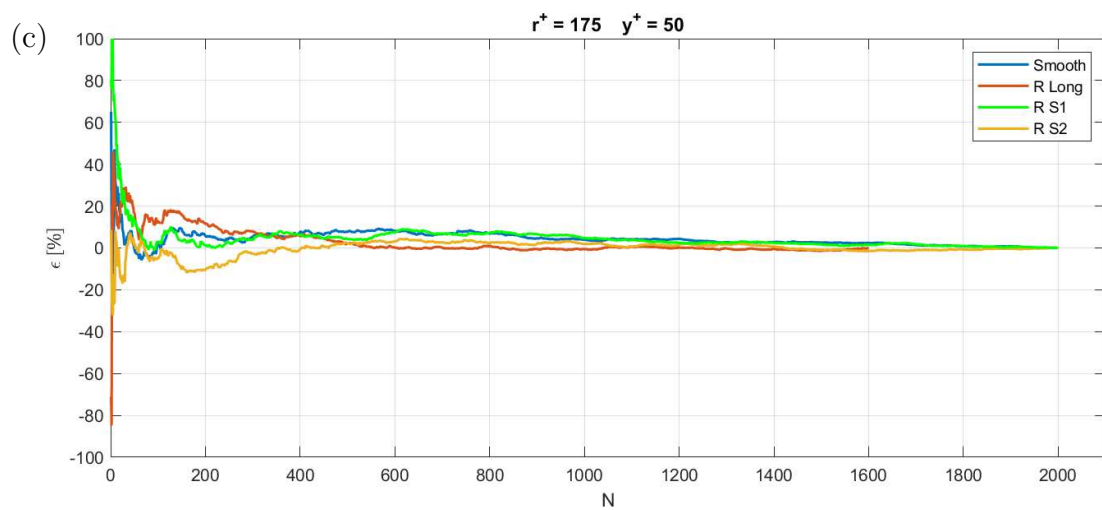
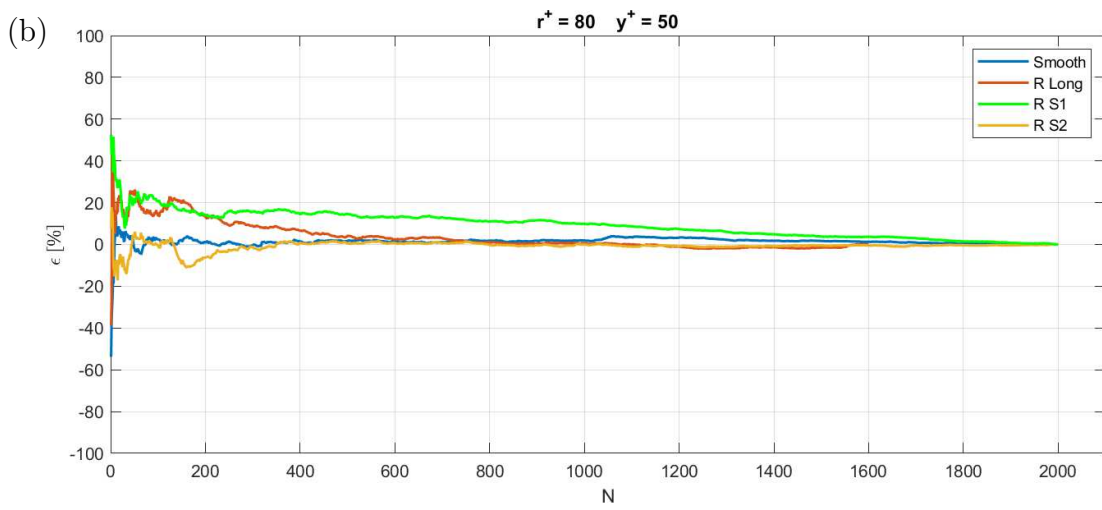
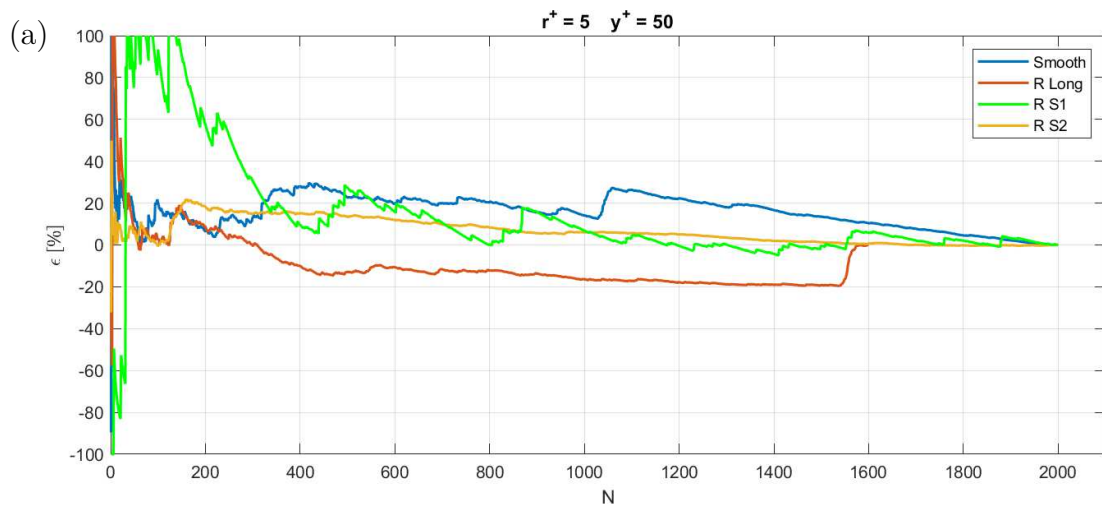


Figure 5.21 - Convergence curves for different scales r^+ and wall-normal coordinate y^+ at $Re_\theta = 3900$.

5 Wavelet analysis of turbulent boundary layer



5 Wavelet analysis of turbulent boundary layer

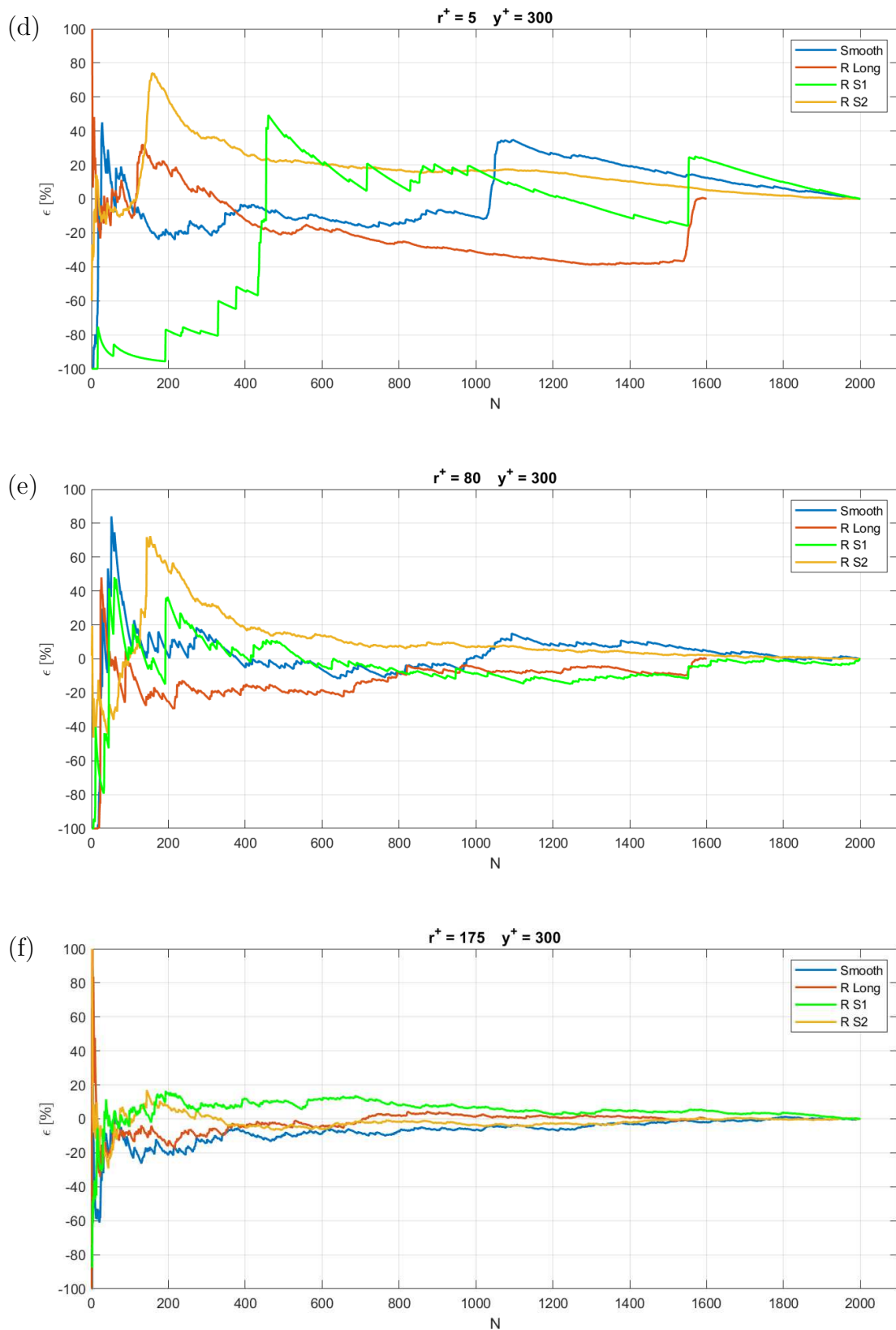


Figure 5.22 - Convergence curves for different scales r^+ and wall-normal coordinate y^+ at $Re_\theta = 4895$.

6 Conclusion

The analysis process adopted during the development of the present study appear to work properly and give a good description of the flow field examined for the coherent structure identification. The coherent structures result, generally, correctly educed and associated to the corresponding length-scale. There are also some inaccuracies concerning highlighted areas which do not shows the presence of vortices, despite they have a cross-energy correlation.

Within the round jet flow field, the method correctly identities coherent structures relative to the planar section of azimuthal structures, i.e. vortex-rings, while going downstream through the transition region things become more complicated due to the enhanced chaotic motion of the flow and some vortices are identified, anyway. The identified structures show values of length-scale coherent with those found in literature. Furthermore, the wavelet maps had been compared with the λ_2 -Criterion, showing a good matching between the two methods.

In fully turbulent flow field, like turbulent boundary layer, the method is well stressed, although it shows good results too. The educed coherent structures consist, in all likelihood, to section of hairpin vortices' heads as showed through the Galilean transform of the velocity field which clearly reveals the vortices, while we have no confirmation about sweeps, ejections, and widely, streamwise structures which seems to be effectively retrieved, but there isn't the absolute confidence due to the impossibility to perform a comparison.

Lastly, a statistical analysis of wavelet maps for the boundary layer of smooth and riblet surfaces was conducted on the attempt to evaluate possible differences between them. These results need to be treated carefully due to the convergence performances, although they seem to confirm riblets performances. The sinusoidal riblets appear to have an increased drag reduction performance than straight riblets. Indeed, the "vortical" activity appear to be reduced with respect to smooth and longitudinal riblet surfaces. The sinusoid probably modifies the properties of coherent structures within the boundary layer mixing the drag reduction effects of riblets with those related to oscillating plates. Moreover, the sinusoidal riblets with the higher amplitude value appear to work better than others, while sinusoidal riblets with lower amplitude show a behaviour, in the near-wall area, in contrast with other riblets. Therefore, a more accurate evaluation of these statistics data is needed.

6.1 Future works

The wavelet analysis of particle image velocimetry can be adopted for future deepest analysis to evaluate the characteristics of riblets boundary layer's flow fields by means other PIV data sampled within different planes, like the horizontal plane (x-z plane), or more likely, the transversal plane (y-z plane) in order to obtain values of the spanwise component of velocity, which, as literature states, is the responsible for the drag reduction performances. Moreover, the correct eduction of streamwise structures which is only hypothesized in the present work can be confirmed or denied and can give a significative contribution to a better understanding of drag reduction mechanism and properties modification of coherent structures adopting riblet surfaces.

Bibliography

- [1] M. Farge, "Wavelet transforms and their applications to turbulence," *Annu. Rev. Fluid Mech.*, 1992.
- [2] M. V. Dyke, "An Album of Fluid Motion," 1982.
- [3] H. E. Fiedler, "Coherent structures in turbulent flows," 1987.
- [4] A. K. M. F. Hussain, "Coherent structures and turbulence," 1983.
- [5] J. Jeong and F. Hussain, "On the identification of a vortex," *J. Fluid Mech.*, 1995.
- [6] S. B. Pope, "Turbulent Flows," 2000.
- [7] R. Camussi, "Coherent structure identification from wavelet analysis of particle image velocimetry data," *Experiments in Fluids - Springer*, 2002.
- [8] C. Ball, H. Fellouah and A. Pollard, "The flow field in turbulent round free jets," *Elsevier ScienceDirect*, 2012.
- [9] R. J. Adrian, "Hairpin vortex organization in wall turbulence," *Phys. Fluid*, 2007.
- [10] Y. Fu, C. Yuan and X. Bai, "Marine drag reduction of shark skin inspired riblet surfaces," *Elsevier - ScienceDirect*, 2017.
- [11] D. Bechert, M. Bruse, W. Hase and R. Meyer, "Biological surfaces and their technological application - Laboratory and flight experiments on drag reduction and separation control," *AIAA*, 1997.
- [12] H. Choi, P. Moin and J. Kim, "Direct numerical simulation of turbulent flow over riblets," *J. Fluid Mech.*, 1993.
- [13] R. Mayoral and J. Jiménez, "Drag reduction by riblets," *Phil. Trans. R. Soc. A*, 2011.

- [14] K.-S. Choi, “Near-wall structure of a turbulent boundary layer with riblets,” *J. Fluid Mech.*, 1989.
- [15] M. Sasamori, O. Iihama, H. Mamori, K. Iwamoto and A. Murata, “Parametric study on a sinusoidal riblet for drag reduction by direct numerical simulation,” *Flow Turbulence Combust*, 2017.
- [16] Y. Peet and P. Sagaut, “Turbulent drag reduction using sinusoidal riblets with triangular cross-section,” *AIAA*, 2008.
- [17] D. Bechert and W. Hage, “Drag reduction with riblets in nature and engineering,” *WIT Press*, 2006.
- [18] G. Ciullo, “Caratterizzazione di superfici con riblet sinusoidali mediante tecnica PIV,” 2020.

Ringraziamenti

Sono giunto alla conclusione di questo percorso. Ovviamente, non avrei potuto farcela senza il sostegno e, in alcuni casi, la guida di coloro che mi sono stati “accanto”.

Inizio con il ringraziare il professor Cafiero e il professor Iuso per avermi guidato nel lavoro di tesi e sono loro grato per le conoscenze che sono riusciti a trasferirmi.

Durante questi anni ho potuto contare sul supporto dei miei amici-colleghi Max, Dario, Laura, Federica e Francesco con i quali, per buona parte del percorso, ho condiviso gli studi e che continuano a far sentire la loro presenza nella mia vita nonostante la distanza che ci separa. In particolare, voglio ringraziare Francesco che non ha mai mancato di portare il buon umore in qualsiasi momento.

Gli anni trascorsi in collegio mi hanno arricchito e divertito e vorrei ringraziare il mio V Piano della Sezione Crocetta dove ho trascorso tutti questi anni e, in particolare, vorrei ringraziare quello scapestrato di Enrico, detto “Messner il rosso”, che di tanto in tanto mi ha condotto su per i monti.

Altro elemento portante dell’esperienza torinese è Ignazio con cui da sempre condivido una profonda amicizia e che in tutti questi anni è stato sempre compagno di risata assicurata.

Poi, c’è Alessio, fedele rivale ragusano che mi ha sostenuto e consigliato con la sua alquanto discutibile saggezza nei momenti di difficoltà e che sempre ha una buona parola per me.

Grazie agli amici compatrioti modicani tra cui Carmelo, Lucia, Peppe, Maria, Alberto, Jessika, Giorgio, Luciano per i momenti trascorsi insieme durante la mia permanenza in terra sicula.

Grazie al Csf14 per i meravigliosi momenti\allenamenti trascorsi insieme; nonostante ci siamo incontrati da così poco tempo Ciccio Pt ha già preso posto nel mio cuore.

Nulla di tutto questo sarebbe stato possibile senza il sostegno e il supporto della mia famiglia che nonostante la distanza è sempre stata al mio fianco e che mai ha mancato di farmi sentire il suo affetto, sostenendomi anche nei momenti più complicati che ho affrontato.

E, infine, grazie ad Alessia che tanto ha sopportato e supportato i pochi anni che ancora abbiamo trascorso insieme. Come al solito, una buona parte del merito per il raggiungimento di questo traguardo toccherebbe a lei per tutte le lamentele e le ansie che ha condiviso e dovuto sopportare. Nonostante i lunghi mesi e la distanza che ci separava, sei sempre riuscita a farmi sentire il tuo amore. Grazie per le avventure in cui sei riuscita a trascinarci e che insieme abbiamo vissuto e affrontato segnando soltanto l’inizio di questa vita insieme.

